

University of Louisville

ThinkIR: The University of Louisville's Institutional Repository

Electronic Theses and Dissertations

6-2013

Dielectrophoretic precipitation of airborne particles.

Joseph D. Duff
University of Louisville

Follow this and additional works at: <https://ir.library.louisville.edu/etd>

Recommended Citation

Duff, Joseph D., "Dielectrophoretic precipitation of airborne particles." (2013). *Electronic Theses and Dissertations*. Paper 376.
<https://doi.org/10.18297/etd/376>

This Master's Thesis is brought to you for free and open access by ThinkIR: The University of Louisville's Institutional Repository. It has been accepted for inclusion in Electronic Theses and Dissertations by an authorized administrator of ThinkIR: The University of Louisville's Institutional Repository. This title appears here courtesy of the author, who has retained all other copyrights. For more information, please contact thinkir@louisville.edu.

DIELECTROPHORETIC PRECIPITATION OF AIRBORNE PARTICLES

By

Joseph D. Duff

B.S. UNIVERSITY OF LOUISVILLE, 2010

A Thesis

Submitted to the Faculty of the

University of Louisville

J.B. Speed School of Engineering

as Partial Fulfillment of the Requirements

for the Professional Degree

MASTER OF ENGINEERING

DEPARTMENT OF MECHANICAL ENGINEERING

JUNE 19, 2013

APPROVAL PAGE

DIELECTROPHORETIC PRECIPITATION OF AIRBORNE PARTICLES

Submitted by: _____
Joseph D. Duff

A Thesis Approved on

_____ June 19, 2013 _____
(Date)

By the Following Reading and Examination Committee:

Stuart J. Williams, Thesis Director

XXXXXXX

XXXXXXXX

XXXXXXXXXX

XXXXXXXX

ACKNOWLEDGEMENTS

I would like to thank Dr. Stuart J. Williams for his patience, guidance, and tutelage throughout my educational career. Without Dr. Williams I would not have attempted to perform a Thesis or any research beyond the structured research requirement. Furthermore, I couldn't have created the devices without Vanessa Velasco's cleanroom instruction and training. Vanessa has gone out of her way to help and provide hands on instruction that prepared me to accomplish this research. Last, but not least, my parents, Joe and Brenda Duff; I couldn't have reached this level of educational success without their support and encouragement.

ABSTRACT

Experimental and numerical modeling studies of particle separation from a gas stream using a dielectric force have shown that dielectrophoresis is an appropriate mechanism for the filtration of a particulate matter from a particle laden gas stream. Dielectrophoresis technology has the ability to produce high filtration efficiency with highly restive particles. This is the first known work producing a device that demonstrates that dielectrophoresis will separate particles from this type of fluidic system.

The testing was conducted using frequencies on the order of 60 Hz, 15 kHz, and DC. The voltage ranged from 100V to 300V and the fluid velocity was varied from 1.5 m/s to 3 m/s. The dielectrophoretic separation device was designed to use interdigitated electrodes. Interdigitated electrodes are a well know device that produces dielectrophoresis in other applications[1]. The interdigitated electrodes were designed to be 20 μ m wide and spaced 20 μ m apart. The device collected particles under all frequencies, voltages, and fluid velocities; the testing shows that there is an inverse relationship between the fluid velocity and applied voltage, the lower the fluid velocity the higher the voltage; the greater the collection of particles.

TABLE OF CONTENTS

I. INTRODUCTION	5
A. PARTICULATE MATTER.....	5
B. EFFECTS OF PARTICULATE MATTER POLLUTION	5
C. MOTIVATION	6
LITERATURE REVIEW	7
A. AIR POLLUTION CONTROL AND EPA REQUIREMENT	7
B. PARTICLE CONTROL BY CYCLONIC SEPARATION.....	8
C. PARTICLE CONTROL BY FABRIC FILTER.....	9
D. PARTICLE CONTROL BY ELECTROSTATIC PRECIPITATOR.....	10
E. DIELECTROPHORETIC FILTRATION EXPERIMENTS	12
II. THEORETICAL BACKGROUND OF DIELECTROPHORESIS	14
A. DIELECTROPHORETIC FORCE ON A PARTICLE	15
B. COMPLEX PERMITTIVITY	18
C. INDUCED EFFECTIVE DIPOLE MOMENT OF PARTICLES	19
D. ELECTROPHORESIS IN AC FIELDS	22
E. DIELECTROPHORESIS IN DC FIELDS	24
III. PARTICULATE MATTER DYNAMICS.....	24
A. PARTICLE SIZE DISTRIBUTION	24
B. PARTICLE BEHAVIOR	25
C. STOKES LAW	28
IV. DIELECTROPHORETIC PRECIPITATOR AND FILTER	29
V. THE IDEAL FILTER	30
VI. STATEMENT OF WORK.....	30
VII. EXPERIMENT	31

A.	DEVICE DESIGN	31
B.	DEVICE FABRICATION	34
C.	TEST APPARATUS AND EQUIPMENT	36
D.	ISO 12103-1 TEST DUST PARTICLE SIZE DISTRIBUTION	39
E.	EXPERIMENTAL PROCEDURE AND METHODS	40
VIII.	RESULTS	42
A.	COMPUTER SIMULATION (2D)	42
1.	<i>Clausius-Mossotti Factor</i>	42
2.	<i>Computational fluid dynamics Simulation (2D)</i>	47
3.	<i>Dielectrophoresis Simulation</i>	52
4.	<i>Combination Dielectrophoresis Velocity And Fluid Velocity Simulation</i>	59
5.	<i>Particle tracing Simulation</i>	61
C.	EXPERIMENTAL	67
1.	<i>Experimental Results</i>	67
2.	<i>Image results</i>	77
3.	<i>Power Measurements</i>	78
IX.	DISCUSSION	79
X.	CONCLUSIONS	83
XI.	RECOMMENDATIONS	84

LIST OF TABLES

TABLE I CYCLONE COLLECTOR ADVANTAGES AND DISADVANTAGES	8
TABLE II FABRIC FILTER ADVANTAGES AND DISADVANTAGES	9
TABLE III ELECTROSTATIC PRECIPITATOR ADVANTAGES AND DISADVANTAGES	12
TABLE IV CUNNINGHAM CORRECTION FACTOR AT 1 ATM AND 25 °C[4].....	28
TABLE V DIELECTROPHORETIC PRECIPITATOR ADVANTAGES AND DISADVANTAGES.....	29
TABLE VI DIELECTROPHORETIC FILTER ADVANTAGES AND DISADVANTAGES	29
TABLE VII THE IDEAL FILTER	30
TABLE VIII MEASURED FLUID VELOCITY	36
TABLE IX TEST DUST STATISTICAL DATA	39
TABLE X LIST OF TESTS PERFORMED	40
TABLE XI ELECTRICAL PROPERTIES OF ISO TEST DUST.....	42
TABLE XII SUMMARY OF CLAUSIUS MOSSOTTI FACTORS.....	46
TABLE XIII POWER MEASUREMENTS.....	78

LIST OF FIGURES

FIGURE 1 CYCLONE COLLECTOR DIAGRAM	8
FIGURE 2 PRINCIPLE OF MECHANICAL SEPARATION OF DIRT PARTICLES WITH FIBER FILTERS [22]	9
FIGURE 3 ELECTROSTATIC PRECIPITATOR DIAGRAM	10
FIGURE 4 FILTER EFFICIENCY OBTAINED FROM TESTING AT LAWRENCE LIVERMORE[8]	13
FIGURE 5 DIELECTROPHORETIC EFFECT	14
FIGURE 6 THREE PHASE ELECTRIC CURTAIN	15
FIGURE 7 REPRESENTATION OF THE FORCE AND TORQUE EXERTED UPON A SMALL DIPOLE BY AN ELECTRIC FIELD OF FORCE.	16
FIGURE 8 PLOT OF VARIATION OF THE REAL (SOLID LINE) AND IMAGINARY (DOTTED LINE) PARTS OF THE CLAUSIUS- MOSSOTTI FACTOR WITH FREQUENCY. THE HIGH AND LOW FREQUENCY LIMITING VALUES OF THE REAL PART ARE SHOW, AS WELL AS THE VALUE OF THE IMAGINARY PART AT THE	22
FIGURE 9 DEVICE DESIGN	33
FIGURE 10 PHOTO MASK DESIGN	35
FIGURE 11 FABRICATED DEVICE	35
FIGURE 12 DESIGN OF TEST APPARATUS	37
FIGURE 13 TEST EQUIPMENT SETUP	38
FIGURE 14 FREQUENCY OF OCCURRENCE	39
FIGURE 15 CLAUSIUS-MOSSOTTI FACTOR OF EACH PARTICLE VS. FREQUENCY	43
FIGURE 16 CLAUSIUS-MOSSOTTI FACTOR OF SiO ₂ PARTICLE VS. FREQUENCY	44

FIGURE 17 CLAUSIUS-MOSSOTTI FACTOR OF Al_2O_3 PARTICLE VS. FREQUENCY.....	44
FIGURE 18 CLAUSIUS-MOSSOTTI FACTOR OF CaO PARTICLE VS. FREQUENCY.....	45
FIGURE 19 CLAUSIUS-MOSSOTTI FACTOR OF MgO PARTICLE VS. FREQUENCY.....	45
FIGURE 20 CLAUSIUS-MOSSOTTI FACTOR OF TiO_2 PARTICLE VS. FREQUENCY.....	46
FIGURE 21: CFD BOUNDARY AND GEOMETRY PLOT.....	47
FIGURE 22: CFD SURFACE PLOT; VELOCITY = 0.1 M/S.....	48
FIGURE 23 CFD SURFACE PLOT; VELOCITY = 1.5 M/S.....	49
FIGURE 24 CFD SURFACE PLOT; VELOCITY = 2.3 M/S.....	50
FIGURE 25 CFD SURFACE PLOT; VELOCITY = 3.0 M/S.....	51
FIGURE 26: DEP ELECTRODE ARRAY DESIGN AND BOUNDARY CONDITIONS.....	53
FIGURE 27: DEP SURFACE PLOT OF $\log_{10}F_{dep}$: 100V.....	54
FIGURE 28 DEP SURFACE PLOT OF $\log_{10}F_{dep}$: 150V.....	55
FIGURE 29 DEP SURFACE PLOT OF $\log_{10}F_{dep}$: 200V.....	56
FIGURE 30 DEP SURFACE PLOT OF $\log_{10}F_{dep}$: 250V.....	57
FIGURE 31 DEP SURFACE PLOT OF $\log_{10}F_{dep}$: 300 V.....	58
FIGURE 32: COMBINATION OF DIELECTROPHORESIS VELOCITY AND FLUID VELOCITY.....	60
FIGURE 33 PARTICLE TRACING PLOT: AIR VELOCITY IS 1.5 M/S AND APPLIED VOLTAGE VALUE OF 100 V.....	61
FIGURE 34 PARTICLE TRACING PLOT: AIR VELOCITY IS 1.5 M/S AND APPLIED VOLTAGE VALUE OF 200 V.....	62
FIGURE 35 PARTICLE TRACING PLOT: AIR VELOCITY IS 0.01 M/S AND APPLIED VOLTAGE VALUE OF 250 V.....	63

FIGURE 36 PARTICLE TRACING PLOT: AIR VELOCITY IS 1.5 M/S AND APPLIED VOLTAGE VALUE OF 300 V	64
FIGURE 37 PARTICLE TRACING PLOT: AIR VELOCITY IS 2.3M/S AND APPLIED VOLTAGE VALUE OF 300V	65
FIGURE 38 PARTICLE TRACING PLOT: AIR VELOCITY IS 3.0M/S AND APPLIED VOLTAGE VALUE OF 300V	66
FIGURE 39: CLEAN DEVICE BEFORE TESTING; TAKEN UNDER 10X MAGNIFICATION.....	67
FIGURE 40 EXPERIMENT #1: UNDER 5X MAGNIFICATION AND 1.5 M/S AIR VELOCITY	68
FIGURE 41: EXPERIMENT #2: UNDER 5X MAGNIFICATION AND 1.5 M/S AIR VELOCITY	69
FIGURE 42:EXPERIMENT #3: UNDER 5X MAGNIFICATION AND 1.5 M/S AIR VELOCITY.....	70
FIGURE 43:EXPERIMENT #4: UNDER 5X MAGNIFICATION AND 1.5 M/S AIR VELOCITY.....	71
FIGURE 44:EXPERIMENT #5: UNDER 5X MAGNIFICATION AND 2.3 M/S AIR VELOCITY.....	72
FIGURE 45:EXPERIMENT #6: UNDER 5X MAGNIFICATION AND 3.0 M/S AIR VELOCITY.....	73
FIGURE 46:EXPERIMENT #7: UNDER 5X MAGNIFICATION AND ≈ 0 M/S AIR VELOCITY	74
FIGURE 47:EXPERIMENT #8: UNDER 5X MAGNIFICATION AND 2.3M/S AIR VELOCITY	75
FIGURE 48:EXPERIMENT #9: UNDER 5X MAGNIFICATION AND 3.0M/S AIR VELOCITY	76
FIGURE 49:EXPERIMENT #10: UNDER 5X MAGNIFICATION AND 1.5 M/S AIR VELOCITY.....	77
FIGURE 50 IMAGE RESULTS	78

I. INTRODUCTION

A. Particulate Matter

Particulate matter (PM) is typically defined as a microscopic discrete mass of a solid or liquid that remains individually dispersed in gas or liquid emissions and is considered to be an atmospheric pollutant[2]. There are three main sources of PM. The first is materials-handling processes, for example, ball mills and rock crushing[3]. The second is gas conversion reaction in the atmosphere[3]. The third, and most common source, is the incomplete combustion of fossil fuels[3]. However, there are natural sources of PM including forest fires, tornados, sand storms, ocean spray, and pollen[4].

B. Effects of Particulate Matter Pollution

There are a number of different harmful effects caused by particulate matter beyond environmental and human health hazards. One such effect is the corrosion of metals[2]. Particulate matter is commonly comprised of oxides, whose enhanced hardness caused abrasive wear on protective surfaces; providing a path for moisture to attack vulnerable layers. Such path leads to surface corrosion and the potential loss of material integrity.

Particulate matter also impacts human health. The adverse health effects of particulate matter include the exacerbation of asthma, increases in the occurrence of lung cancer, decreases of the overall standard of living[5]. Airborne particles contribute to the poor quality of indoor and outdoor air. To reduce the health impact of airborne particles, the Environmental Protection Agency (EPA) has established the national ambient air quality standards (NAAQS).

The national ambient air quality standard is designed to improve the quality of and reduce the toxicity of the air. However, there are challenges in reducing the health impact of airborne particles. There is a relationship between the health impact of PM and the sizes of the particles that make up aggregate of the PM. Smaller particles have the greatest effects on health. This occurs as the diameter of the particle decreases; the surface area of the particle increases relative to its mass. This increased surface area-to-mass relationship allows the particle to adhere to the lining of the lungs[5]. When this occurs the particles in the lungs cause inflammation due to a complex set of molecular and cellular responses resulting from exposure pathogens and/or noxious substances that are included in particles[5].

C. MOTIVATION

A more effective method for particulate matter removal is necessary to protect the environment and human health. Currently there are only a few commonly used methods for the collection and removal of airborne particles. One such device is the electrostatic precipitator (ESP). ESPs remove PM from the air through electrostatic force. However, the efficiency of ESP's are limited by the ESP's ability to charge the particle[3]. For those particles with high resistivity, traditional ESP's are not an effective means of PM removal[2].

There has been extensive emphasis placed on effective precipitation of ESP's with optimum amounts of electrical input during the corona process of collection. While the power input is limited by structural and/or individual component defects, most power limitations occur under conditions of excessive electrical resistivity of the collected material[3]. In the design of electrostatic precipitators, the electrical resistivity of the airborne particles is one of several

important factors to be considered, since resistivity inversely influences the allowable electrical operating parameters.

Particle resistivity can alter the actual collection efficiency and has the greatest impact on the design of ESPs[2]. The most economical design and operation of ESPs are obtained when the electrical resistivity of the particulate is low and within ideal limits[4]. However, this characteristic of the particle permits some particles, like ash, to penetrate and escape the ESPs[4]. This is a quandary in the design and application of ESPs.

To remove highly resistive or electrically neutral particles from a gas stream a different type of filtering technology is needed. A device using dielectrophoresis (DEP) technology has been shown in this work to remove neutral particles from a gas stream. DEP technology does not depend on the particle's resistivity solely. DEP is a function of the conductivity and the permittivity of the particle and the medium[6]. Furthermore, the electric voltage needed to operate a DEP systems are significant lower, resulting in decreased operating cost.

LITERATURE REVIEW

A. AIR POLLUTION CONTROL AND EPA REQUIREMENT

The Environmental Protection Agency (EPA) is the federal agency that was created by National Environmental Policy Act of 1970[4]. This act was designed to provide policing and enforcement of the laws and governance of the Clean Air Act Amendments (CAAA) of 1970. The CAAA required the EPA to establish the National Ambient Air Quality Standards (NAAQS). The NAAQS has established standards to protect public health. The standards are intended to provide protection to public well-being, health, aesthetics, or economic damage[4].

The EPA has determined that PM is a criteria air pollutant and has established regulations for PM less than 10 μm (PM-10) in diameter and less than 2.5 μm (PM-2.5) in diameter. The PM-10 standard is set at a rate of $150\mu\text{g}/\text{m}^3$ in a 24 hour period. The PM-2.5 is set at a rate of $15\mu\text{g}/\text{m}^3$ on an annual mean[4].

B. PARTICLE CONTROL BY CYCLONIC SEPARATION

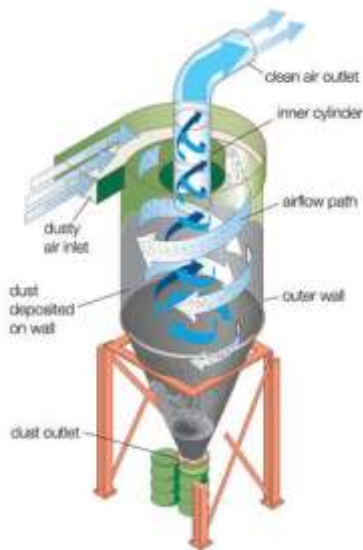


Figure 1 Cyclone Collector Diagram[21]

A cyclone collector uses centrifugal force to separate particles from the gas stream. This is performed by taking the particle laden gas and forcing it in a smaller and smaller circular path[4]. This circular path provides the mean to separate the particles through centrifugal force contacting the separator wall and exiting out the bottom of the separator[4]. The clean gas then exists through the top of the separator. There are a several advantages and disadvantages of cyclone collector listed in Table

I[3].

TABLE I CYCLONE COLLECTOR ADVANTAGES AND DISADVANTAGES

Advantages	Disadvantages
Low Cost	Large Pressure Loss
No Moving Parts; Leading To Few Maintenance Problems.	Low Collection Efficiencies (Diameters above 10μ)
Dry Collection And Disposal	Inability To Handle Wet Or Sticky Material

This type of separator is ideal as a pre-cleaner for higher efficient equipment like bag-houses and ESPs[4]. Applications for cyclone collectors are extensive; for example, they are used for recovering and recycling catalysts in petroleum refineries and for recovering freeze-dried coffee in food-processing plants[2].

C. PARTICLE CONTROL BY FABRIC FILTER

Fabric filters or impingement filters refer to a group of filtering technology that has been around over one hundred years[7]. Fabric filters are typically used as a porous support medium.

This medium performs filtration on the entire fluidic system resulting in larger pressure losses across the filter[3]. The fabric filter was designed from a point of view that the filter will collect particle matter and a cake will form that will cover the fabric filter and remove the PM from the gas stream[4]. The

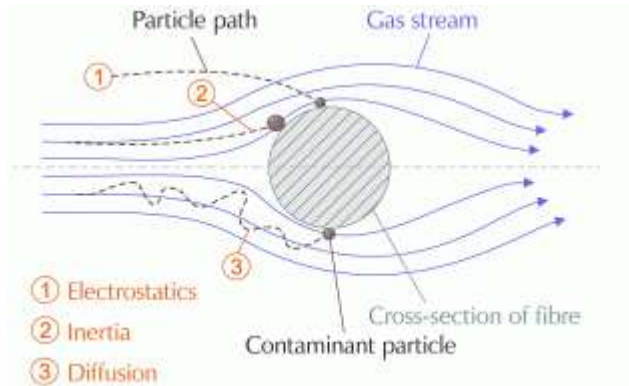


Figure 2 Principle of mechanical separation of dirt particles with fiber filters [22]

advantages and disadvantages of filtration methods are listed in Table II[3].

TABLE II FABRIC FILTER ADVANTAGES AND DISADVANTAGES

Advantages	Disadvantages
High Collection Efficiencies	High Maintenance Requirement
Dry Collection And Disposal	Dust Dependent Fire Or Exposition Risk
No High Voltage Hazard	Short Fabric Life
Insensitive To Gas Stream Fluctuation	Medium Pressure Drop
Can Handle Wet Or Sticky Material	Low Temperature Requirement

The most common type of industrial fabric filter is the bag-house. The bag-house is typically used where higher collection efficiencies are needed[2]. There are a few economic and technical issues with this type of system. The first is that a bag-house does not reach the high collection efficiencies needed until the bags develop a cake, potentially leading to compliance issues[3]. The last issue is the high maintenance requirement that is needed for the bags[3]. The bag will need to be replaced on a given time intervals, which requires shutting down the system for filter replacement.

D. PARTICLE CONTROL BY ELECTROSTATIC PRECIPITATOR

Electrostatic precipitators filter the air in a way that is different than the previously discussed mechanical filters. An “electrostatic” phenomenon is recognized by the presence of electrical charge, either stationary or moving, and the interaction of these charges[2]. Charge interaction results in particle collection and not by reason of their motion. For an Electrostatic precipitators the electrostatic force is applied directly to the particle in the gas stream and not indirectly[3]. This allows for higher ESP gas flows and collection efficiencies with moderate power consumption.

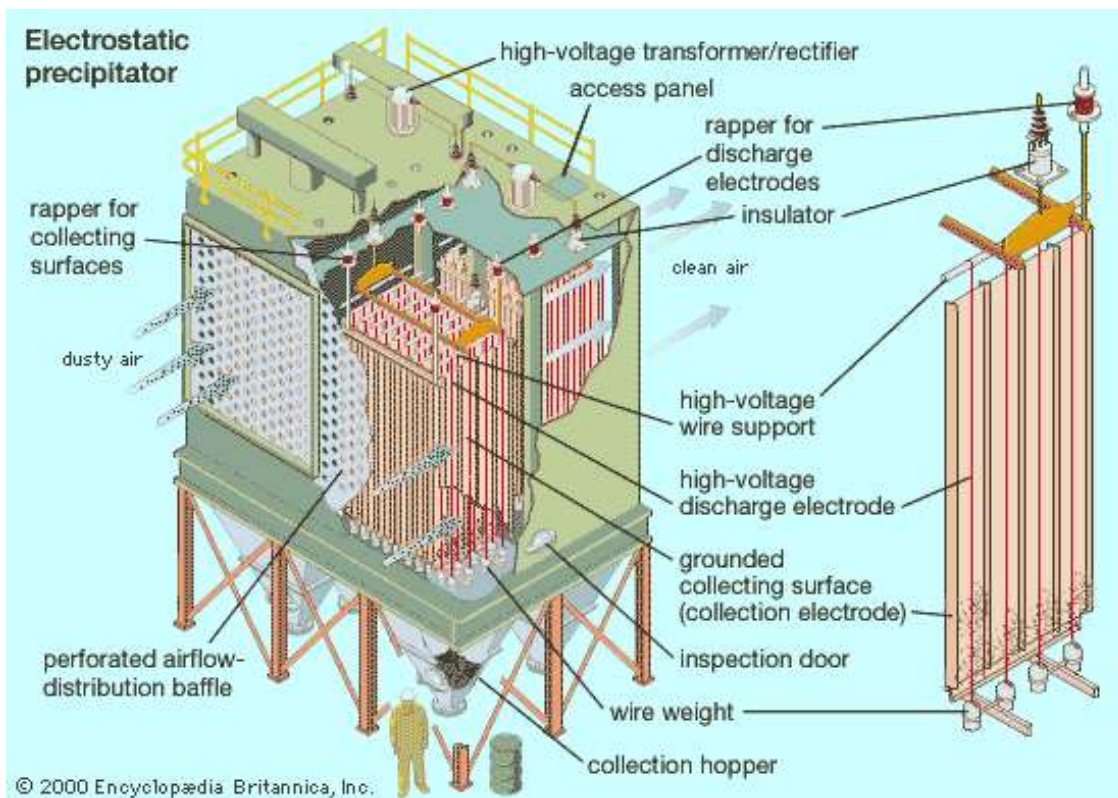


Figure 3 Electrostatic Precipitator Diagram[20]

There are three fundamental steps in Electrostatic precipitator operation. First the particle must be charged[2]. This occurs when the particle-laden gas stream passes through a high

voltage positive DC corona[2]. Within the corona there are two separate charging mechanisms that occur. The first charging mechanism is the charging of ions that is produced by the force of the applied electric field. This charging can be written as follows[2]:

$$q = 12\pi\epsilon_0 E r_p^2 \left(\frac{\epsilon_p}{\epsilon_p + 2} \right) \left[\frac{t}{t + \left(\frac{4\epsilon_0}{N_0 e K} \right)} \right] \quad (1)$$

where E is the electric field strength, r_p is the particle radius, ϵ_0 is the permittivity of free space, ϵ_p is the relative dielectric constant of the particle, K is the mobility of the gas ions, e is the electronic charge, N_0 is the ion density, and t is the time. The charge decreases with particle radius. The second charging mechanism is due to ion diffusion, which depends on the thermal energy of the ions, not on the electric field[2]. For ESPs, electric field charging is the dominant charging mechanism[2].

The second fundamental step in the electrostatic precipitator process is the collection of particles. Electrostatic precipitators collect particulate matter using Coulomb's law of electric forces acting on the particle where[2]:

$$F_e = qE \quad (2)$$

where q is the particle charge, and F_e is the electrostatic force.

The third and final step in the electrostatic precipitator process is the removal of the collected particles into an external holding area[3]. This is often treated as a needless detail and over-looked, but is just-as important as the first two steps. Proper and timely removal of collected particles can prevent particle loss by re-entrainment. Re-entrainment can occur from many sources. However, thorough and careful design will mitigate this from happening.

Modern electrostatic precipitators have collection efficiencies greater than 99.9%. However, this is somewhat misleading; the efficiency is calculated using the mass of the particle and not the particle quantity. Therefore, collection efficiencies have to increase further to collect the nanometer-sized particles. For this to occur, higher voltages, slower fluid velocities, and a greater collection area is necessary. Increased efficiencies come at added expense. The additional advantages and disadvantages of ESPs are listed in Table III[3].

TABLE III ELECTROSTATIC PRECIPITATOR ADVANTAGES AND DISADVANTAGES

Advantages	Disadvantages
High Collection Efficiencies	High Capital Cost
Dry Collection And Disposal	Sensitive To Gas Stream Fluctuation
Low Pressure Drop	Sensitive To Particle Resistivity
Continuous Operation With Low Maintenance Requirement	High Voltage Hazard
Large Gas Flow Rates	Produces Ozone “A Criteria Air Pollutant”
High Temperature And Pressure Operation	Explosion Hazard With Combustible Gas

Even with an abundant number of disadvantages ESPs are still the most cost effective and sustainable way to remove PM on the market[3].

E. DIELECTROPHORETIC FILTRATION EXPERIMENTS

In 1976 the Lawrence Livermore Laboratory conducted a series of experiments with electric field across a filter medium[8]. They designed an apparatus that held a media type filter between two 0.5-mm-thick perforated stainless steel plates (29% open) spaced 13 mm apart by two polyethylene spacers[8]. A negative high DC voltage lead was connected to the front screen and the rear screen was grounded. A polydispersed sodium chloride particle with a mean diameter of 0.95 μ m was used as a test aerosol[8]. The experiments used a number of different face velocities ranging from 16.3 cm/s to 65 cm/s[8]. The efficiency of the filters where

measured at voltages ranging from 0-15 kV, and the pressure differential was monitored throughout the testing. The test included 25 different types of filter medium ranging from fiber glass to polyester fabric. The experiment concludes that all materials exhibited significant increases in efficiency with increasing field strengths. Efficiencies of >99% could be obtained from glass fiber mats using a 13 kV/cm electric field at 16.3 cm/s face velocity. Figure 4 is a plot of the filter efficiency obtained from testing[8].

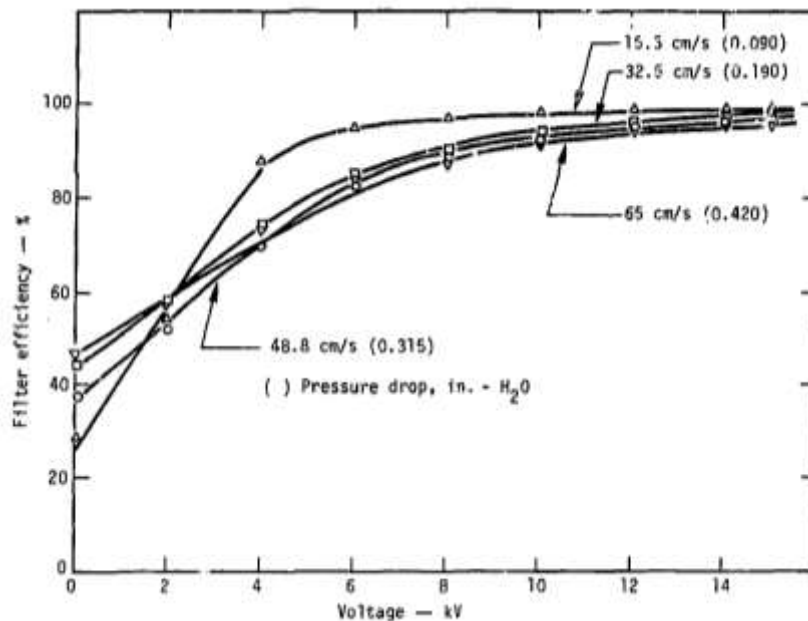


Figure 4 filter efficiency obtained from testing at Lawrence Livermore[8]

However, in 1978 the Lawrence Livermore team concluded that the dielectrophoresis effect is minor and these conclusions were based on observations and a developed Coulombic static force model[9]. The Lawrence Livermore team stated that there were two factors responsible for dielectrophoresis negligible contribution to the increase in filter efficiency with an applied electric field:

1. Nearly all aerosols were charged ionic particles[9]
2. Dielectrophoresis is only important for large particles[9]

The Lawrence Livermore team's conclusions are only partially correct. A dielectrophoretic force will not affect a charged ionic particle. However, dielectrophoresis is not limited to only large particles. Dielectrophoresis has been used to remove DNA from cell. DNA molecules have a consistent width of 2.5 nanometers; which is smaller than the mean diameter of the aerosol used for testing at Lawrence Livermore.

II. THEORETICAL BACKGROUND OF DIELECTROPHORESIS

Dielectrophoresis was first described by Herbert Pohl in 1951[10]. Pohl defined dielectrophoresis as the translational motion of neutral matter caused by polarization effects in a nonuniform electric field[10]. This effect should never be confused with electrophoresis. Electrophoresis is the motion produced by a charged particle in a uniform electric field. The foundations for dielectrophoresis are stated below:

- The dielectrophoretic force is only present when particles are in a nonuniform electric field[11].
- The dielectrophoretic force is not governed by the polarity of the electric field and can be observed either with AC or DC excitation[11].
- Particles are attracted to regions of greater nonuniform electric field when they are more polarizable than that of the suspension medium[11]. (a.k.a. positive dielectrophoresis)
- When the medium is more polarizable than that of the particles, particles are repelled from the nonuniform field regions[11]. (a.k.a. negative dielectrophoresis)

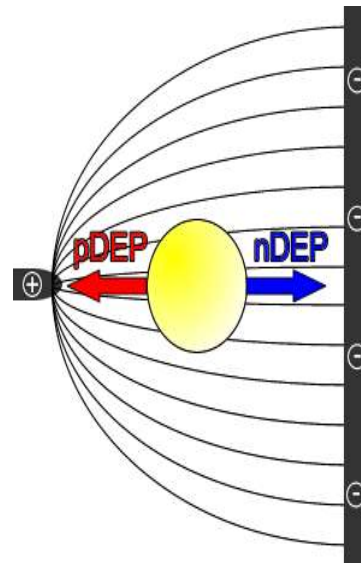


Figure 5 Dielectrophoretic Effect [11]

One of the greatest strengths of dielectrophoresis is that the direction of the applied force is frequency and material property dependent. Therefore, two dissimilar particles can experience different magnitudes and different direction of the DEP force. For example H. Li and R. Bashir separated live listeria cell using DEP[12].

Dielectrophoresis can also be used in conjunction with out-of-phase AC current[13]. This out-of-phase AC current produces an effect of a traveling wave. The traveling wave dielectrophoretic phenomena have been used to design and build self-cleaning transparent dust shields for protecting solar panels[13]. The dust shield consists of a series of parallel electrodes that generate a traveling wave acting as a contactless conveyor as shown in Figure 6[13]. Particles are repelled and pushed by dielectrophoresis to translate the particle along or against the direction of the wave, depending on their polarization.

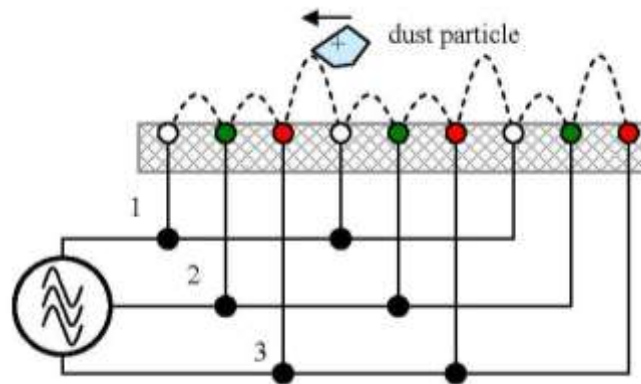


Figure 6 Three phase electric curtain[11]

A. DIELECTROPHORETIC FORCE ON A PARTICLE

If a charged particle is placed inside a nonuniform electric field, it experiences a force imbalance that will direct it to move towards the electrode with the opposite charge[11]. Conversely, neutral particle experience an effect that is profoundly different. Under the influence of the non-uniform electric field, the neutral particle becomes polarized[6]. It acquires a negative

charge on the side of the positive electrode and conversely, a positive charge on the side of the negative electrode. However, the particle is overall neutral in total charge. Nevertheless, the field is non-uniform and it diverges across the particle causing a force imbalance[6]. The forces on these two charged poles are unequal resulting in a force imbalance that causes the particle to move[10].

The direction in which the particle will move does not depend on the direction of the electric field[6]. Therefore, the dielectrophoretic effect can be observed in either DC or AC electric fields. However, AC fields are chosen for the reason that the frequency of the field can be selected to sort particle and characterize their polarization. This fact is due to the simultaneous application of positive DEP and negative DEP on two different particles[6].

As shown in Figure 7, the polarized particle can be treated as a dipole, with equal and opposite charges $+q$ and $-q$ located at vector \vec{d} apart. The dipole is located in a non-uniform electric field described with the vector \vec{E} [11].

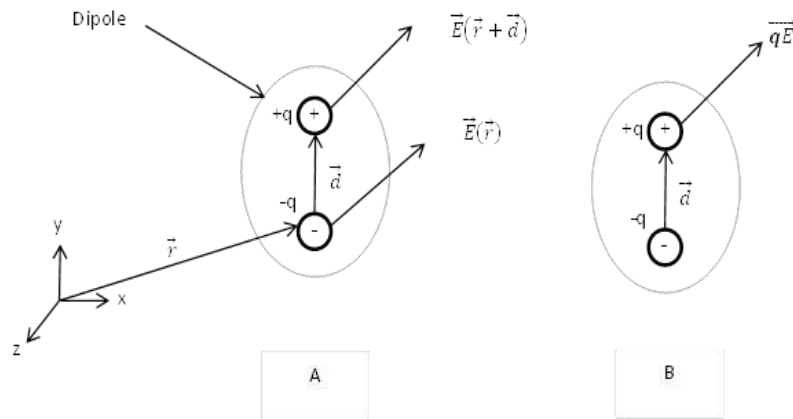


Figure 7 Representation of the force and torque exerted upon a small dipole by an electric field of force[6].
A. Net force on a small dipole of strength $p = qd$ in a nonuniform electric field.[6] **B. Coulombic force components creating net torque on a small dipole of strength $p = qd$ in a uniform electric field[6]**

Let's assume that the dipole does not influence the magnitude of the electrical field strength; the force on the dipole will be equal to the sum of the two forces acting on the dipole. Performing a sum of the forces on the particle, we have[6]

$$\vec{F} = q\vec{E}(\vec{r} + \vec{d}) - q\vec{E}(\vec{r}) \quad (3)$$

where \vec{r} is the position vector of the negative charge $-q$. If $|\vec{d}|$ is small compared to the characteristic dimension of the electric field non-uniformity, equation (3) can be simplified. The electric field vector can be expanded about position \vec{r} using the vector Taylor series expansion; that is[6]

$$\vec{E}(\vec{r} + \vec{d}) = \vec{E}(\vec{r}) + \vec{d}\nabla\vec{E}(\vec{r}) + \dots \quad (4)$$

In the previous equation, the additional higher order terms, of order d^2 , d^3 , and so forth, have been neglected, since d is considered to be very small. Equation (4) can be re-written as[6]

$$\vec{F} = q\vec{d}\nabla\vec{E}(\vec{r}) \quad (5)$$

The dipole moment of a polarized particle is given as[6]

$$\vec{p} = q\vec{d} \quad (6)$$

By combining equations (5) and (6), the dielectrophoretic force on a particle with a dipole moment \vec{p} , which is placed in a non-uniform electric field \vec{E} at the position given by a vector \vec{r} , equals[6]

$$\vec{F} = q\nabla\vec{E}(\vec{r}) \quad (7)$$

From equation (7), the dielectrophoretic force on a polarized particle is equal to zero if the electric field is uniform. This equation is an approximation of the DEP force on a particle, because we have neglected the size of the particle when compared to the characteristic dimension of the electric field non-uniformity. However, for circumstances where there is a collection of particles that can interact, these equations have potential for significant errors due to the non-uniformities of the electric field induced by the particles themselves[6]. In this case the higher order effects must be taken into account.

B. COMPLEX PERMITTIVITY

Complex permittivity describes the frequency-dependent response of the dielectric particle to the electric field. An ideal dielectric media is loss-free and has constant permittivity; however, this is not true for most media. The non-ideal dielectric media depends on their frequency-dependent polarization within the applied electric field. For a parallel-plate capacitor with an ideal dielectric between its plates, the impedance is given by the following equation[6]

$$Z = \frac{1}{i\omega F} \quad (8)$$

where, ω is equal to $2\pi f$, where f is the frequency of the electric field, $i^2 = -1$, and F is the capacitance of the dielectric. If it is a non-ideal dielectric the total impedance is given by[6]

$$Z = \frac{1}{\frac{1}{R}i\omega F} = \frac{R}{1 + i\omega RF} \quad (9)$$

where, R is the resistance of the non-ideal dielectric. Substituting for R and F we can rewrite equation (9) in the form of a parallel plate capacitor whose capacitance is given by the plate surface area and the distance between the plates, we get the following[6]

$$F = \tilde{\epsilon} \frac{A}{d} \quad (10)$$

where, A is the plate surface area, d is the distance between the plates, and $\tilde{\epsilon}$ is the complex permittivity given by[6]

$$\tilde{\epsilon} = \epsilon_0 \epsilon_r - i \frac{\sigma}{\omega} \quad (11)$$

where $\tilde{\epsilon}$ is the complex permittivity, ϵ_0 is the permittivity of free space, ϵ_r is the relative permittivity of the dielectric, and σ is the conductance of the dielectric.

C. INDUCED EFFECTIVE DIPOLE MOMENT OF PARTICLES

A particle-laden gas stream rarely consists of a homogenous particle size and composition. It is more likely that a number of particles with varying properties will exist. When the electric field is applied, surface charge accumulates at the interfaces between the particles and the media due to their different dielectric properties[6]. Both the polarizability of the dielectrics and the surface charge accumulation are frequency dependent. Therefore, the overall force on the particle's effective dipole moment must be analyzed using complex permittivity[6].

The simplest case is that of a single homogenous dielectric sphere suspended in a homogenous dielectric medium. The derivation of the equation for the effective dipole moment of the particle in this case is given in equation (3). The result is given by the following[6]:

$$\vec{p} = 4\pi\epsilon_m \left(\frac{\epsilon_p - \epsilon_m}{\epsilon_p + 2\epsilon_m} \right) r_p^3 \vec{E} \quad (12)$$

where, ε_m is the permittivity of medium, ε_p is the permittivity of the particle, r is the radius of the particle, and E is the electric field strength.

There are times when the equation for the effective dipole moment of a particle is simplified, for example, for a spherical particle, the equation is given as[6]:

$$\vec{p} = v\tilde{\alpha}\vec{E} \quad (13)$$

where, v is the volume of the particle, and $\tilde{\alpha}$ is the effective polarizability of a sphere given as[6]:

$$\tilde{\alpha} = 3\varepsilon_m \left(\frac{\tilde{\varepsilon}_p - \tilde{\varepsilon}_m}{\tilde{\varepsilon}_p + 2\tilde{\varepsilon}_m} \right) = 3\varepsilon_m \tilde{f}_{cm} \quad (14)$$

here, \tilde{f}_{cm} is the Clausius-Mossotti factor. This is a complex number that describes the effective permittivity or polarizability of particles, given by[6]:

$$\tilde{f}_{cm}(\varepsilon_p, \varepsilon_m) = \left(\frac{\tilde{\varepsilon}_p - \tilde{\varepsilon}_m}{\tilde{\varepsilon}_p + 2\tilde{\varepsilon}_m} \right) \quad (15)$$

Figure 8 shows the plot of the variation of the real and imaginary parts of the Clausius-Mossotti factor with the frequency of the applied field[11]. The real part depends solely on the conductivity of the medium at low frequencies. Conversely, the high frequency limiting value is $\frac{\varepsilon_p - \varepsilon_m}{\varepsilon_p + 2\varepsilon_m}$ and the polarization is dominated by the permittivity of the particle and suspending medium. The imaginary part is zero at low and high frequencies, then reaches a maximum at the relaxation frequency. The reciprocal value of this frequency, also called the Maxwell-Wagner relaxation frequency, represents the relaxation time of the particles polarizability and is given as[14]

$$\tau_{mw} = \frac{\varepsilon_p - 2\varepsilon_m}{\sigma_p + 2\sigma_m} \quad (16)$$

Consequently, the real part of the Clausius-Mossotti factor goes from a maximum value of 1 to the value of -1/2 at different frequencies depending on the medium and the particle dielectric properties. The imaginary part is equal to zero at high and low frequencies and has a theoretical range of -3/4 to +3/4.

Comparable to equation (14), this shows the effective polarizability of a sphere, the following shows the effective polarizability of a homogeneous dielectric ellipsoid with the half lengths of the major axes given as a_1 , a_2 , and a_3 [6]:

$$\tilde{\alpha}_n = 3\varepsilon_m \tilde{K}_n \quad (17)$$

where, $\tilde{\alpha}_n$ is the effective polarizability given for each of the major axes, and $n = 1, 2$, or 3 . K_n is a frequency dependent factor similar to Clausius-Mossotti factor, and is given by[6]:

$$\tilde{K}_n(\tilde{\varepsilon}_p, \tilde{\varepsilon}_m) = \frac{\tilde{\varepsilon}_p - \tilde{\varepsilon}_m}{3(A_n \tilde{\varepsilon}_p - \tilde{\varepsilon}_m) + 2\tilde{\varepsilon}_m} \quad (18)$$

where, A_n is the depolarizing factor for the axis n , and is given by[6]:

$$A_n = \frac{1}{2} a_1 a_2 a_3 \int_0^\infty \frac{ds}{(s + a_n^2)B} \quad (19)$$

where, s is the arbitrary distance for integration, and B is given as[6]:

$$B = \sqrt{(s + a_1^2)(s + a_2^2)(s + a_3^2)} \quad (20)$$

Given equation (13) for the effective dipole moment and equation (18), the following equation can be used to calculate the effective dipole moment of ellipsoids[6]:

$$\vec{p} = \frac{4\pi a_1 a_2 a_3}{3} \left(\frac{\tilde{\epsilon}_p - \tilde{\epsilon}_m}{\tilde{\epsilon}_p + A_n(\tilde{\epsilon}_p - \tilde{\epsilon}_m)} \right) \vec{E} \quad (21)$$

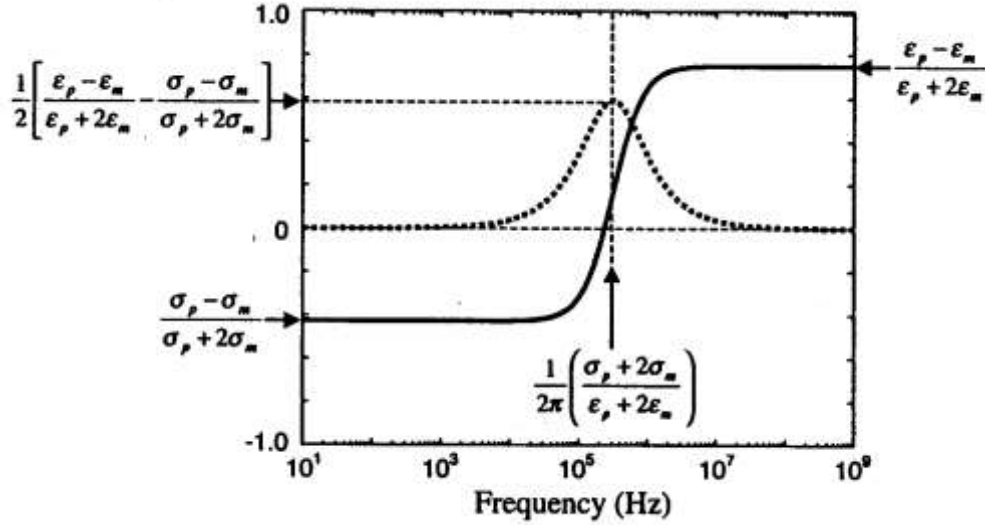


Figure 8 Plot of variation of the real (solid line) and imaginary (dotted line) parts of the Clausius-Mossotti factor with frequency. The high and low frequency limiting values of the real part are show, as well as the value of the imaginary part at the[6]

D. ELECTROPHORESIS IN AC FIELDS

Comparing AC and DC fields, dielectrophoresis in AC fields has a number of advantages. If the phase is constant across the system, the imaginary part can be neglected; by using the equations (5) and (13), the time-averaged DEP force becomes[6]:

$$\langle F_{DEP} \rangle = \frac{1}{2} v Re[\tilde{\alpha}] \nabla |\tilde{E}_{RMS}|^2 \quad (22)$$

where, E_{RMS} is the root mean square value of the electric field. Equation (22) shows that the DEP force is proportional to the volume of the particle and the gradient of the field magnitude squared.

The real part of the particle's effective polarizability determines the direction of the DEP force. It can be shown that if the polarizability of the particle is greater than the polarizability of the medium, the real part of the Clausius-Mossotti factor is positive and the particles therefore

move to the regions of high field strength. If the polarizability of the particle is less than the polarizability of the medium, the real part of the effective polarizability is negative, and therefore, the particles move towards the regions of the low field strength.

In the case where different field phases are applied, the DEP force expression becomes more complex, as the imaginary part of the electric field cannot be neglected. In that case, the equation for the DEP force calculation becomes[6]:

$$\langle F_{DEP} \rangle = \frac{1}{2} v Re[\tilde{\alpha}] \nabla |\tilde{E}_{RMS}|^2 - \frac{1}{2} v Im[\tilde{\alpha}] * \{ \nabla_x (Re[\tilde{E}] \times Im[\tilde{E}]) \} \quad (23)$$

Here I_m denotes the imaginary part of the complex value, in this case the effective polarizability. It is clear from equation (23) that if the imaginary part of the electric field phasor equals zero, the entire second term on the right hand side of the equation go to zero, and equation (23) is equal to the equation (22). It should be noted that the second term depends on the imaginary part of the Clausius-Mossotti factor, and therefore, its value equals zero at high and low frequencies, and reaches its maximum at the Maxwell-Wagner relaxation frequency[6].

If the electrodes are of a suitable layout, the second term on the right hand side of equation (23) can represent forces due to the travelling wave electric field[6]. This leads to the effect of the travelling wave dielectrophoresis twDEP, which can be used for particle transportation along the electrodes[13]. Normally, both of the electric field components need to exist for twDEP to be effective, as stated below:

- The particle is levitated above the electrodes to the regions of low field strength (i.e. the real part of the Clausius-Mossotti factor is negative)[6].
- The imaginary part of the Clausius-Mossotti factor is non-zero, and the particles experience the force of the travelling field wave[6].

E. DIELECTROPHORESIS IN DC FIELDS

For this work the Clausius-Mossotti (f_{CM}) factor is assumed not to vary under a DC and/or low-frequency AC fields. Therefore, the f_{CM} factor is determined solely by the electric conductivity difference between the particle and medium. It should be noted that if the particle is nonconductive and the medium is conductive, then the f_{CM} factor is negative resulting in negative DEP.

III. PARTICULATE MATTER DYNAMICS

A. PARTICLE SIZE DISTRIBUTION

The size distribution of a particle is the first and the most important characteristics in the selection of a particulate matter control device[3]. There are two ways to describe the particle distribution either by number count or by mass[4]. However, it is often more important to express particle size frequencies as percentages of the total number measurements. The distribution of particle sizes in a particle laden gas stream arises from a number of statistical reasons which make it unlikely that the distribution curve follows a normal curve. It's more likely that that the probability curves follows a logarithmic form. The Log probability distribution is expressed as[2]:

$$f(d_p)_n = \frac{\Sigma n}{\log \sigma_g \sqrt{2\pi}} \exp \left[\frac{-(\log d_p - \log d_g)^2}{2 \log^2 \sigma_g} \right] \quad (24)$$

here $f(d_p)_n$ frequency of occurrence of diameter d , n total number of particles, σ_g is the geometric standard deviation obtained from[2]:

$$\text{Log}\sigma_g = \sqrt{\frac{\Sigma [n(\text{log}d_p - \text{log}d_g)^2]}{n}} \quad (25)$$

where d_g is the geometric number mean diameter and is defined as[2]:

$$d_g = \sqrt[n]{d_1 d_2 d_3 \dots, d_n} \quad (26)$$

From the log-probability curve, the number medium diameter, which corresponds to the geometric mean d_g , can be derived. The standard deviation is calculated using[2]:

$$\sigma_g = \frac{84.13\% \text{ size}}{50\% \text{ size}} \quad (27)$$

The geometric mean diameter d_g , and the standard deviation σ_g are determined from the particle size distribution as measured with a particle sizing instrument like a cascade inspector.

B. PARTICLE BEHAVIOR

Let's examine particle motion relative to fluid and/or both relative to each other. The fluid exerts an opposing drag force on that particle relative to its velocity. This opposing drag force is given by[4]:

$$F_D = C_D A_p \rho_F \frac{v_r^2}{2} \quad (28)$$

where F_D is the drag force, C_D is the drag coefficient, A_p is the projected area of the particle, ρ_F is the density of the fluid, and v_r is the relative velocity of the particle. The disconcerting portion of equation (28) is the drag coefficient. Drag coefficients have to be determined experimentally and for that reason they are a shape-dependent parameter[4]. However, there is an empirical approach to determine the drag coefficient using[4]

$$C_D = \alpha Re^{-\beta} \quad (29)$$

where α and β are constants give in Table IV[4].

TABLE IV DRAG COEFFICIENT CONSTANTS

Reynolds Number	α	β
< 2.0	24.0	1.0
2 -500	18.5	0.6
500 – 200,000	0.44	0.0

Non-dimensional parameters are typically used to describe particle flow in a system. Reynolds number is one such parameter; that is the ratio of inertial to viscous forces of a fluid. The Reynolds number is used to determine if the fluid flow is laminar or turbulent flow. For internal flow, if the Reynolds number is less than 2400 the flow is laminar and if it's greater than 2400 it's turbulent[15]. For external flow, 10^5 is the transition number used to determine laminar flow verse turbulent flow[15]. The Reynolds number of the gas is calculated using[15]:

$$Re_g = \frac{D u_g \rho_g}{\mu_g} \quad (30)$$

where Re_g is the Reynolds number for the gas, D is the diameter or characteristic dimension of the gas containing device, u_g gas velocity, ρ_g gas density, μ_g absolute viscosity of the gas. The Reynolds number for the particle is calculated using[2]:

$$Re_p = \frac{d_p (u_p - u_g) \rho_g}{\mu_g} \quad (31)$$

where, d_p is the particle diameter, u_p is the particle velocity. The Reynolds number of the particle is dependent on the velocity of the particle relative the gas stream.

Another non-dimensional parameter is the Knudsen Number. The Knudsen Number is used to characterize particle motion and is defined as the ratio of the mean free path of the gas molecules to the particle diameter and is calculated using[4]:

$$Kn = \frac{2\lambda_g}{d_p} \quad (32)$$

where λ_g is the mean free path of the gas molecules. From the kinetic theory of gas and the mean free path is calculated using[2]:

$$\lambda_g = \frac{\mu}{0.499P \sqrt{\frac{8MW}{\pi RT}}} \quad (33)$$

where P is the absolute pressure, R is the universal gas constant, MW is the molecular weight of the particle, and T is the absolute temperature. When the Knudsen Number is greater than 0.1 particle will slip between gas molecules and the resistance of the air is thought of as discontinuous. This slippage reduces the effect of drag on the particle as predicted by Stokes. To correct for this, the Cunningham correction factor is used and is calculated using[4]:

$$C = 1 + \frac{2.0\lambda_g}{d_p} \left[1.257 + 0.40e^{\left(\frac{-0.55d_p}{\lambda_g}\right)} \right] \quad (34)$$

As shown in Table IV the Cunningham correction factor is significant for particles smaller than 1 micron. However, as the particles diameter increases the significance of the Cunningham correction factor begins to diminish.

TABLE IV CUNNINGHAM CORRECTION FACTOR AT 1 ATM AND 25 °C[4]

$d_p, \mu m$	C
0.01	22.5
0.05	5.02
0.10	2.89
0.50	1.334
1.0	1.166
2.0	1.083
5.0	1.033
10.0	1.017

As shown in Appendix D; we will not be testing particles less than 1 micron. That is to say that the Cunningham correction factor is not a significant factor at this time, but should not be neglected in futures studies with smaller particles.

C. STOKES LAW

When particles are significantly larger than that of the mean free path of the gas, the resistance of the gas to the motion of the particle is determined by the hydrodynamic forces acting on the particle. However, for rigid spherical particles where the medium is infinite in size, this resistance is expresses by Stokes Law. Stokes Law is used for rigid spheres and for Reynolds number less than 1 and it is calculated using[2]:

$$F = -3\pi\mu_g d_p u_r \quad (35)$$

where F is the fluid resistance force, μ_g is the absolute gas viscosity, d_p is the particle diameter, and u_r is the relative velocity between the particle and the gas. The terminal velocity of a spherical particle is calculated by taking in to account the gravitational and fluid resistance force using[2]:

$$u_t = \frac{(\rho_p - \rho_g)gd_p^2}{18\mu_g} \quad (36)$$

where ρ_p is the particle density, and ρ_g is the gas density.

IV. DIELECTROPHORETIC PRECIPITATOR AND FILTER

A dielectrophoretic precipitator would have many advantages and few disadvantages. The principal advantages of a dielectrophoretic precipitator would be the lack of particle penetration from high electrical resistance particles. Moreover, Table V provides a list of advantages and disadvantages for a DEP filter.

Table V Dielectrophoretic Precipitator Advantages and Disadvantages

Advantages	Disadvantages
High Collection Efficiencies	High Capital Cost
Low Pressure Loss	Sensitive To Gas Stream Fluctuation
Continuous Operation With Low Maintenance Requirement	Low Gas Stream Velocity
No High Voltage Hazard	

A dielectrophoretic filter would have different advantages and disadvantages than the precipitator. The principal difference between a dielectrophoretic precipitator and dielectrophoretic filter can be reduced to one main difference. A dielectrophoretic precipitator relies solely on the dielectrophoretic force to provide the method for collection. A dielectrophoretic filter is a hybrid filter, where the dielectrophoretic force is added to a common woven filter. The advantages of a dielectrophoretic filter are show in Table VI.

Table VI Dielectrophoretic Filter Advantages and Disadvantages

Advantages	Disadvantages
High Collection Efficiencies	High Maintenance Requirement
Dry Collection And Disposal	Dust Dependent Fire Or Exposition Risk
No High Voltage Hazard	Short Fabric Life
Insensitive To Gas Stream Fluctuation	
Can Handle Wet Or Sticky Material	Low Temperature Requirement
Low Pressures Loss	

V. THE IDEAL FILTER

The ideal filter would have a number of different qualities than what is currently available in the market today. Some of these qualities would be low to absent pressure loss, high collection efficiencies, and low maintenance requirements. A complete list of the requirement needed for the ideal filter in listed in Table VII

Table VII the Ideal Filter

Advantages
High Collection Efficiencies
Dry Collection And Disposal
No High Voltage Hazard
Insensitive To Gas Stream Fluctuation
Can Handle Wet Or Sticky Material
Continuous Operation With Low Maintenance Requirement
Large Gas Flow Rates
High Temperature And Pressure Operation
Low Cost

VI. STATEMENT OF WORK

The objective of this work is to determine the potential of applying dielectrophoresis to remove solid particles from a gas stream. The process to determine the effectiveness of dielectrophoresis is as follows:

- Design a proven device that applies dielectrophoretic force.
- Examine the effectiveness of varying the fluid velocity on the collection of particle through computer simulation.
- Examine the effectiveness of the varying voltages on of the collection of particle through computer simulation.

- Physically test the effectiveness of varying the voltages and fluid velocities on the collection of particles.
- Determine the power consumed to collect particles.

The outcome of these objectives will determine the potential of dielectrophoresis to remove particles from particle laden gas stream.

VII. EXPERIMENT

A. DEVICE DESIGN

To design a device that would solely test the dielectrophoretic force, we had to design a device that would generate a non-uniform electric field and provide minimal fluidic disturbance. Relying on current technology to provide a proven design, we decided to adopt interdigitated electrodes as the base design to generate the non-uniform electric field. Interdigitated electrodes have been used countless times in the past with great success in demonstrating the effectiveness of dielectrophoresis[12].

The design of the device has several different areas of interest. The first area is the top of the device. In Figure 9, the top of the device has 20 electrical connecting pads; these pads were designed to fit in to a Samtec Mini Card Guide Systems to provide the power needed. The pads were designed to have a width of $350\mu\text{m}$ and a length of $2540\mu\text{m}$ to insure a positive electrical connection.

The second area of interest is the interdigitated electrode testing sites. There are 10 testing sites that measure approximately $1/2\text{mm}$ in width and $1/2\text{mm}$ in length. These testing sites were designed solely for ease of fabrication.

The discontinuous testing sites allowed for one and/or many of the testing sites to malfunction and still have a functioning device. There is a secondary advantage to having ten distinct testing sites. This allowed for a testing group and a control group on one device. The inside width dimensions of the test rig was $\frac{3}{4}$ in and this allowed for a total of five testing sites along the length of the device that would fit inside the test rig for simultaneously testing of all test sites.

The electrodes where designed to provide the applied dielectrophoretic force. The size and pitch are of equal distance and provided the greatest electrical gradient. Figure 9 is a drawing of the device.

B. DEVICE FABRICATION

The device was fabricated using standard micro fabrication techniques including a "Lift-off" process. A "Lift-off" process is a method designed for making micro and nano metallic patterns on a rigid substrate. The general process is:

- A photoresist pattern is defined using a photolithography process.
- A metallic film is deposited by directional sputter film deposition covering the substrate and the photoresist pattern.
- During the lifting-off process, the photoresist under the metallic film is removed with solvent, taking the metal film with it, and leaving only the film which was deposited directly on the substrate.

The precise process used in the fabrication of the device is outlined below:

1. Photoresist Process:

- a. Only one photo mask was used to fabricate the devices. A standard photolithography procedure was incorporated using a silicon oxide substrate.
- b. The first step in designing a photo mask is using a design program like AutoCAD to design a pattern of the device that you wish to build. The photo mask designed for this project is shown in Figure 10. The mask has three "Cards" and each "Card" contains 10 individual testing regions.
- c. Once the photo mask has been designed, a photolithography recipe has to be developed. The recipe used to develop the devices is outlined in Appendix A.

2. Deposition of Metal: Technics Sputtering System

- a. The second step in the fabrication process is the deposition of metal. I used the Technics Sputtering System to deposit a thickness of approximately 150nm of aluminum over the substrate and the photoresist pattern.

3. Lift-Off Process:

- a. The third step in the fabrication process is the removal of excess aluminum and photoresist. This excess is removed by submersion in acetone and sonication.

4. Dicing:

- a. The last and final step in the device fabrication process is the dicing of devices and the substrate. This operation was performed by the Micro / Nano Technology Center. The final device is shown in Figure 10.

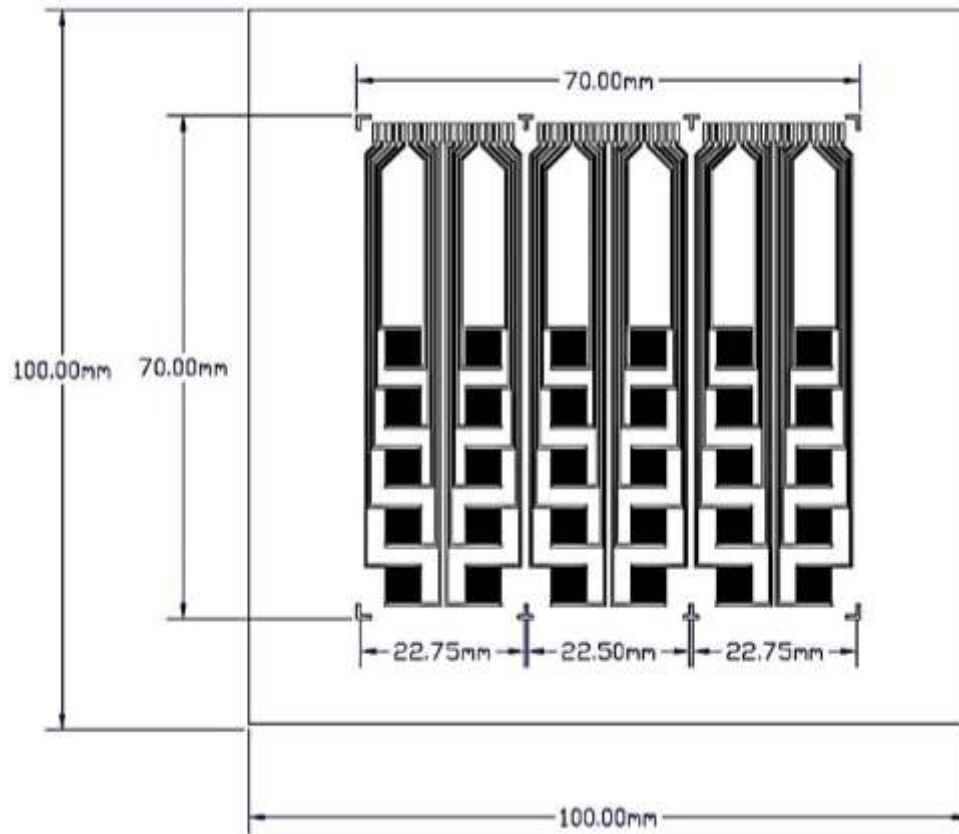


Figure 10 Photo Mask Design

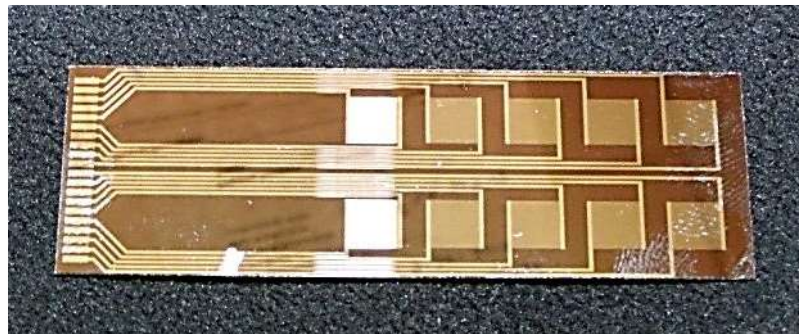


Figure 11 Fabricated Device

C. TEST APPARATUS AND EQUIPMENT

The test apparatus was designed with the intent of using a closed loop system with an 80 mm DC fan to control the velocity of the particle laden air stream. The apparatus is shown in Figure 12. The apparatus was constructed of 1" x 1" acrylic tubing which was purchased from US Plastics. The tubing comes in 10 ft. sections and was cut with a circular saw and assembled together with adhesives. The DC fan was supported by sheet metal and sealed with RTV silicone and tape. The fluid velocity was measured directly above the location where the device performed the experiment. The measurements were taken with a hot wire manometer. Table VIII displays the measured fluid velocity with the fan voltage and the corresponding Reynolds number.

Table VIII Measured Fluid Velocity

Fan Voltage (V)	Air Velocity (m/s)	Reynolds Number
3	1.3	1701.73
4	1.7	2225.34
8	2.8	3665.26
12	3.7	4843.38

During testing the device was connected to an Agilent 34405A Multimeter to measure the voltage, amperage, and the applied voltage frequency. The initial applied voltage was supplied by an Agilent 33220A Waveform Generator. The voltage output from the waveform generator needed to be increased to achieve the desired voltage. To achieve the needed voltage the output voltage from the Waveform Generator was fed through an Agilent 33502A amplifier, and then the output was fed through a Trek 2205 amplifier. The Trek 2205 amplifier was connected to a circuit board through a 20 pin ribbon cable connector. The test equipment setup is show in Figure 13.

ITEM NO.	DESCRIPTION	QTY.
1	1/4 ACRYLIC SHEET (CONNECTION FLANGE)	4
2	12 VDC 80mm CPU FAN	1
4	18 GA SHEET METAL (LOWER TRANSITION)	1
5	18 GA SHEET METAL (UPPER TRANSITION)	1
6	WASHER 1/4	16
7	HFBOLT 1/4-20 x 1 x 0.75-N	8
8	HEX NUT 1/4-20-D-N	8
9	1/8 ACRYLIC SHEET (SUPPORT STAND)	2
10	1/8 ACRYLIC SHEET (SUPPORT STAND)	4
11	2 X 2 ACRYLIC SQUARE TUBING (LONG SIDE)	1
12	2 X 2 ACRYLIC SQUARE TUBING (TOP / BOTTOM)	2
13	2 X 2 ACRYLIC SQUARE TUBING (SIDE)	3
14	DEP DEVICE	1

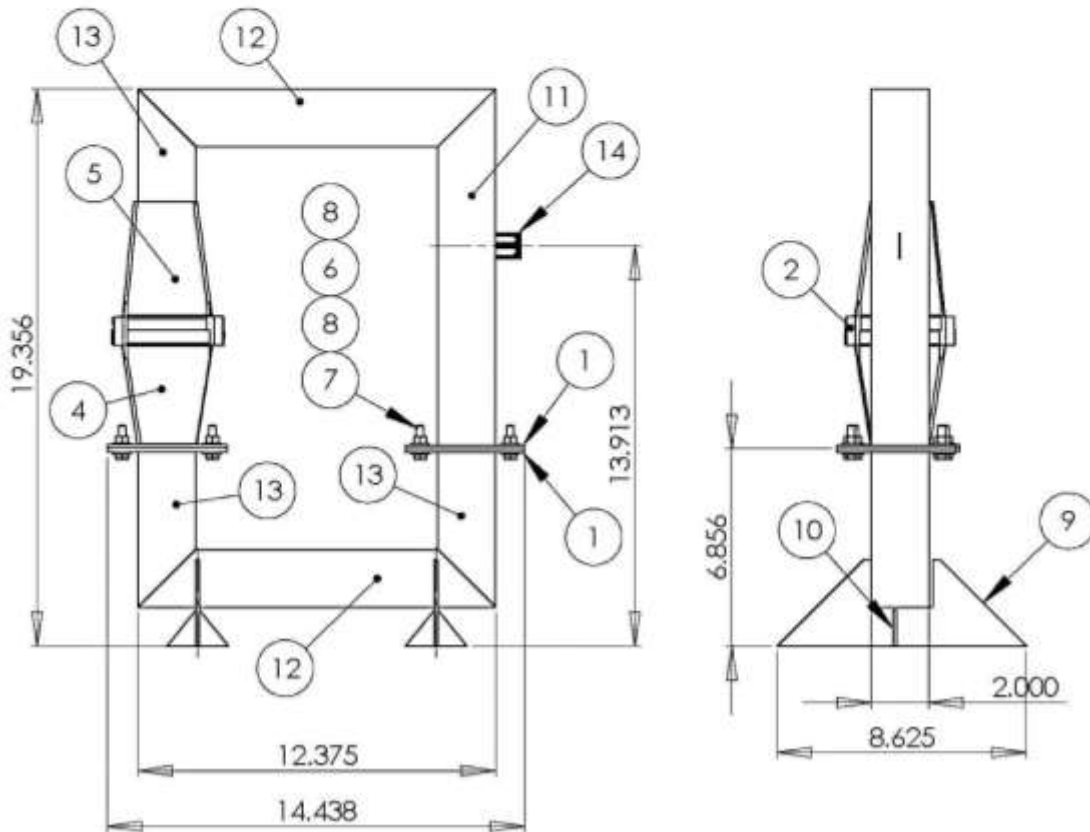


Figure 12 Design of Test Apparatus

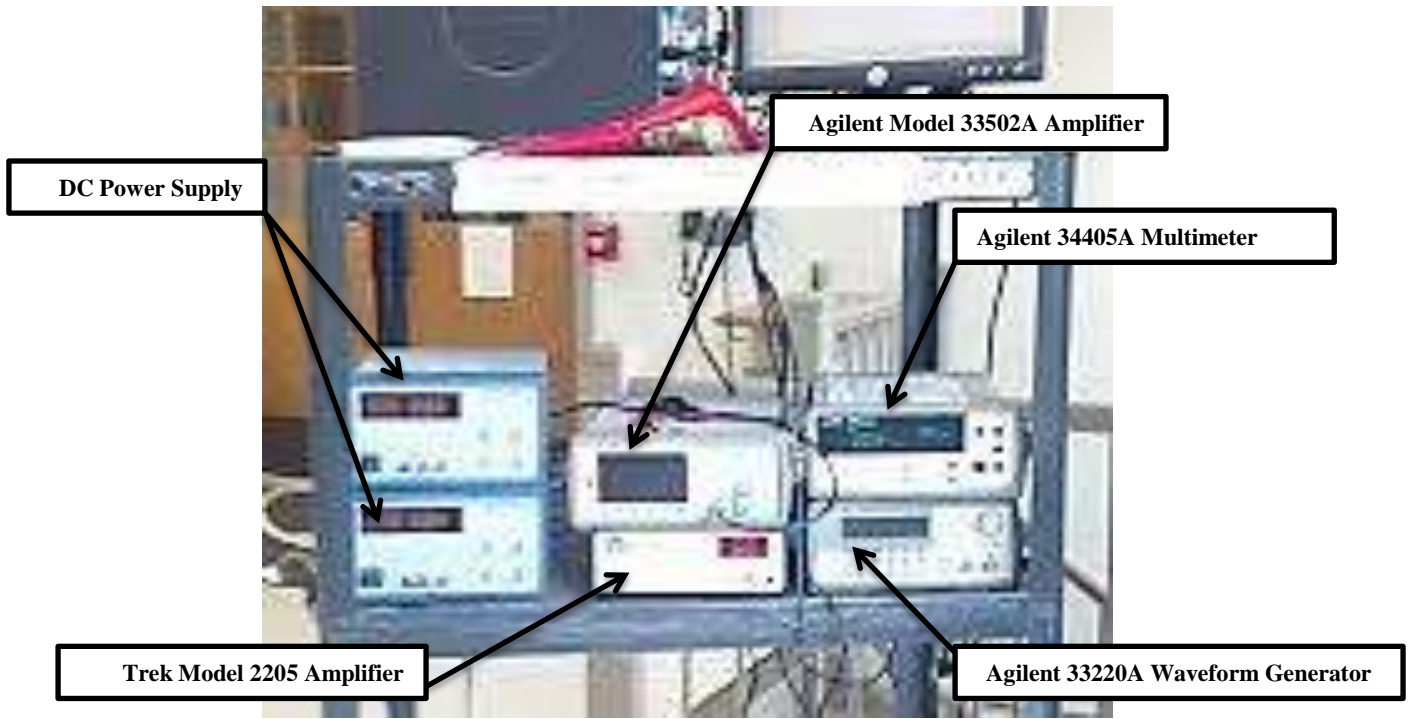


Figure 13 Test Equipment Setup

D. ISO 12103-1 TEST DUST PARTICLE SIZE DISTRIBUTION

During this experiment ISO 12103-1 A1 ultrafine test dust was used for testing. This test dust was purchased from Power Technology Inc. This test dust was selected because it is industry standard dust that has been analyzed for particle size and distribution. The statistical analysis of the test dust is shown in Table IX. This statistical analyzes was performed by Power Technology Inc. using a multisizer accucomp and is shown in Appendix D.

Table IX TEST DUST STATISTICAL DATA

Geometric Mean	Median	Mode	Standard Deviation
4.077	4.476	5.058	3.07

The frequency of occurrence is shown in Figure 13. This figures shows that there is a greater chance of collecting particles in the size range of 3 to 6 microns. The makeup of the dust is comprised of SiO₂, Al₂O₃, CaO, MgO, TiO₂, K₂O, Fe₂O₃ and Na₂O.

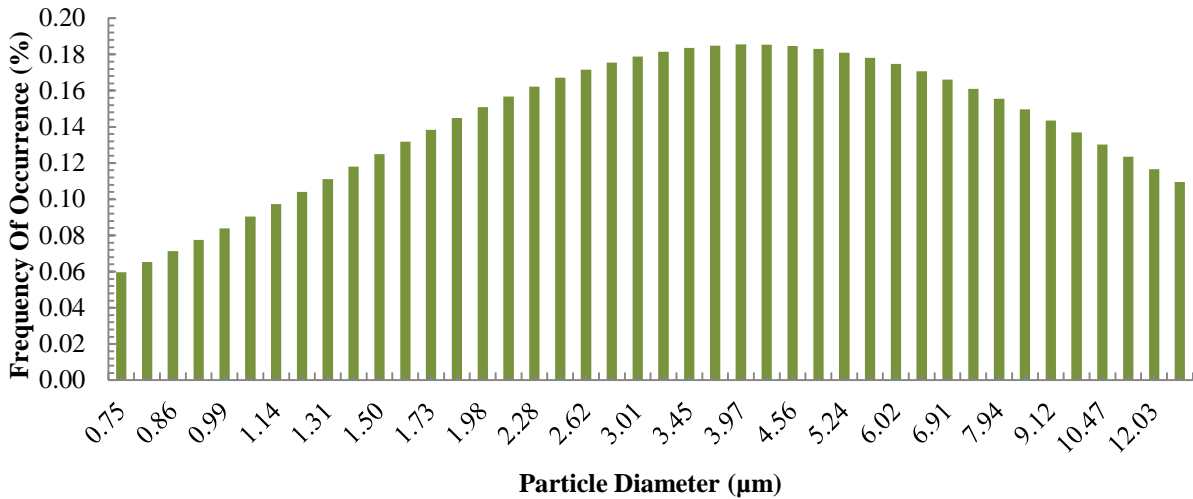


Figure 14 Frequency of Occurrence

E. EXPERIMENTAL PROCEDURE AND METHODS

These experiments were designed with the intent to determine the effectiveness of the dielectrophoretic force. Table X lists the parameter settings for each test that was performed. Each experiment was designed to determine the effect of each of the controllable variables. For example experiments #1 through #4 were designed to determine the role of the applied voltage. Experiment #4 through #6 were designed for the impact of the fluid velocity and experiment #7 through #10 the frequency was varied (60Hz, 15 KHz, DC).

Table X LIST OF TESTS PERFORMED

Experiment	Voltage (V)	Frequencies (Hz)	AC/DC	Air Velocity (m/s)	Reynolds Number
1	100	60	AC	1.5	2000
2	150	60	AC	1.5	2000
3	200	60	AC	1.5	2000
4	300	60	AC	1.5	2000
5	300	60	AC	2.3	3000
6	300	60	AC	3.0	4000
7	250	15K	AC	≈ 0	2000
8	250	15K	AC	2.3	3000
9	250	15K	AC	3.0	4000
10	150	0	DC	1.5	2000

There is no clear and/or direct way to quantify the results of this experiment; this is due to the method of particle collection. To quantify the results for this experiment the amount of particles collected would have to be determined. The design of the device and experiment will not allow for that to occur. However, there is a direct path to determine the effectiveness of the dielectrophoretic force. This path requires a comparison of a clean and powered electro set to a clean and unpowered one. Figure 11 is a picture of a typical device with ten addressable DEP regions. All testing sites were exposed to the same fluid sample.

Each device was cleaned and inspected before each experimental run to insure that there was no pre experiment contamination. After the cleaning process each experimental run was performed using the experimental procedure stated below:

- Clean and inspect device for contamination under 5X magnification using a microscope
- Inspect device for proper fabrication and operation using continuity tester
- Attach device to amplifier, multimeter, waveform generator, and mounting chip
- Place and secure in test rig with tape
- Turn on DC fan and apply the selected voltage that corresponding to the air velocity needed for testing
- Turn on and apply the select test voltage to the device
- Add 1 fluid cup of test dust and/or add test dust as needed for testing. Not all the test dust escapes from the test rig during testing. The amount of dust in the test rig will have to be determined form test to test.
- Test the device for 10 minutes. During the testing time provide burst of compressed air on 2 min intervals. The compressed air forces tests particles that have fallen out of the test air stream back into the air stream.
- Turn off power supplies to the fan and the device. Then remove the device from test rig and place in protective case
- Examine the devices under a microscope, using 5X magnification and capture the effects with a picture

VIII. RESULTS

A. COMPUTER SIMULATION (2D)

1. CLAUDIUS-MOSSOTTI FACTOR

The Clausius-Mossotti factor was calculated using MATLAB script. The script is shown in Appendix B. The electric properties are stated in the Table XI.

TABLE XI ELECTRICAL PROPERTIES OF ISO TEST DUST

Material	Permittivity (F/m)	Conductivity (Siemens/m)
Air	1.00059[16]	0.783×10^{-14} [16]
Silicon Dioxide (SiO_2)	3.8[17]	1×10^{-17} [17]
Aluminium Oxide (Al_2O_3)	9.5[17]	1×10^{-14} [17]
Calcium Oxide (CaO)	3.0[17]	0.000024 [17]
Magnesium Oxide (MgO)	9.6[17]	1×10^8 [17]
Titanium Dioxide (TiO_2)	86[17]	1×10^{-16} [17]

The test dust is comprised of Silicon Dioxide (SiO_2), Aluminium Oxide (Al_2O_3), Calcium Oxide (CaO), Magnesium Oxide (MgO), Titanium Dioxide (TiO_2), Potassium Oxide (K_2O), Iron (III) Oxide (Fe_2O_3), and Sodium Oxide (Na_2O) as shown in Appendix D. The electrical properties of K_2O , Fe_2O_3 , and Na_2O are not available in known literature. However, the combined total percentage of the other known composition is between 81.5% and 99%. It will be assumed that the unknown properties would not be significantly different than the known properties. Therefore, it is assumed that the impact of the unknown properties would not significantly change the outcome of the experiments. Nevertheless, the material in question will be excluded from the simulation. Figures 14 through 19 are graphs of the Clausius-Mossotti factor for the material in Table XI as a function of frequency.

Figure 14 shows all the available material Clausius-Mossotti factors plotted together showing that the real parts of the Clausius-Mossotti factor have a range between 0.48 and 1 for

all given frequencies. The Clausius-Mossotti factor value is not a constant for some particles over the plotted frequency range. Figures 15, 16, 18, and 19 show a plot of the Clausius-Mossotti factor for SiO₂, Al₂O₃, MgO, and TiO₂ respectively. All material in Figures 15-19 have a constant value of 0.48, 0.75, 1.0, and 0.95, respectively.

The plot of the Clausius-Mossotti factor for CaO is shown in Figure 17. Figure 17 shows that the Clausius-Mossotti factor for CaO is frequency dependent and has a range from 1 (below 10⁵Hz) and a value of 0.45 (above 10⁵Hz). The Clausius-Mossotti factor from these plots will be used for the 2D simulation and a summary is providing in Table XII.

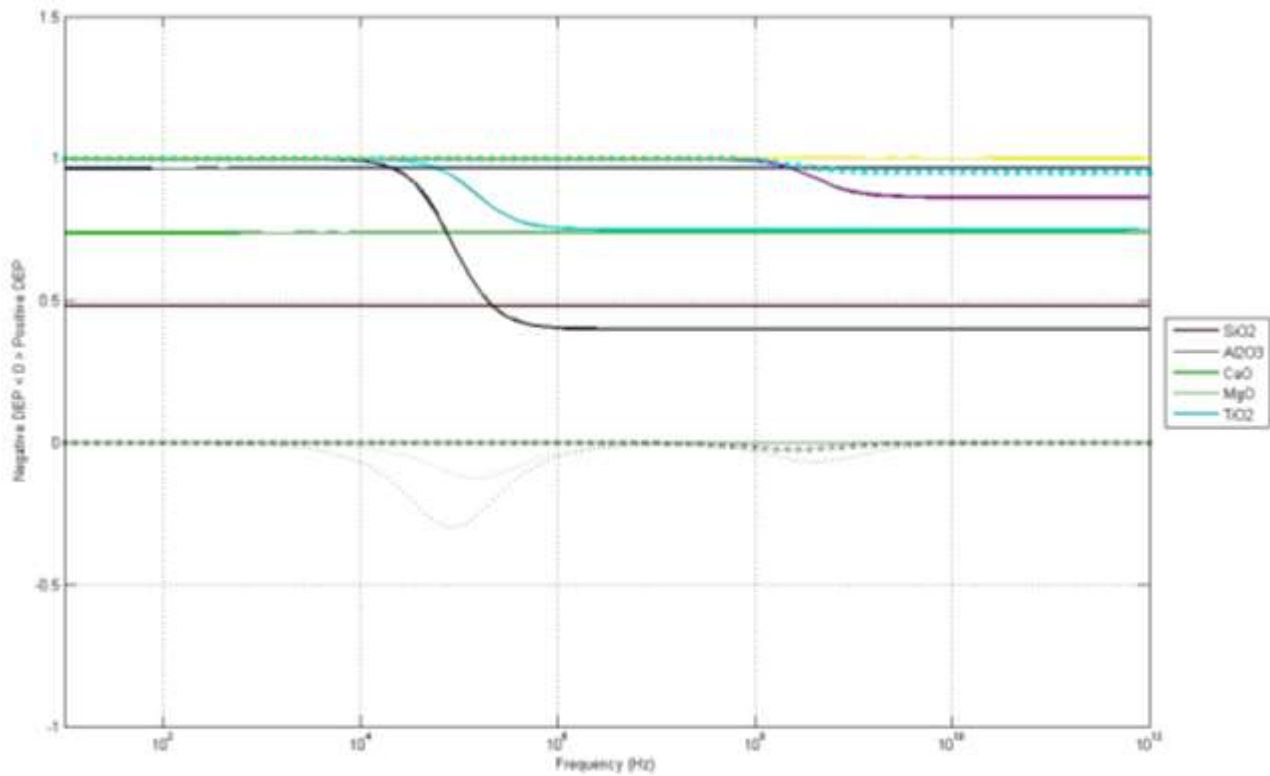


Figure 15 Clausius-Mossotti Factor of each particle vs. frequency

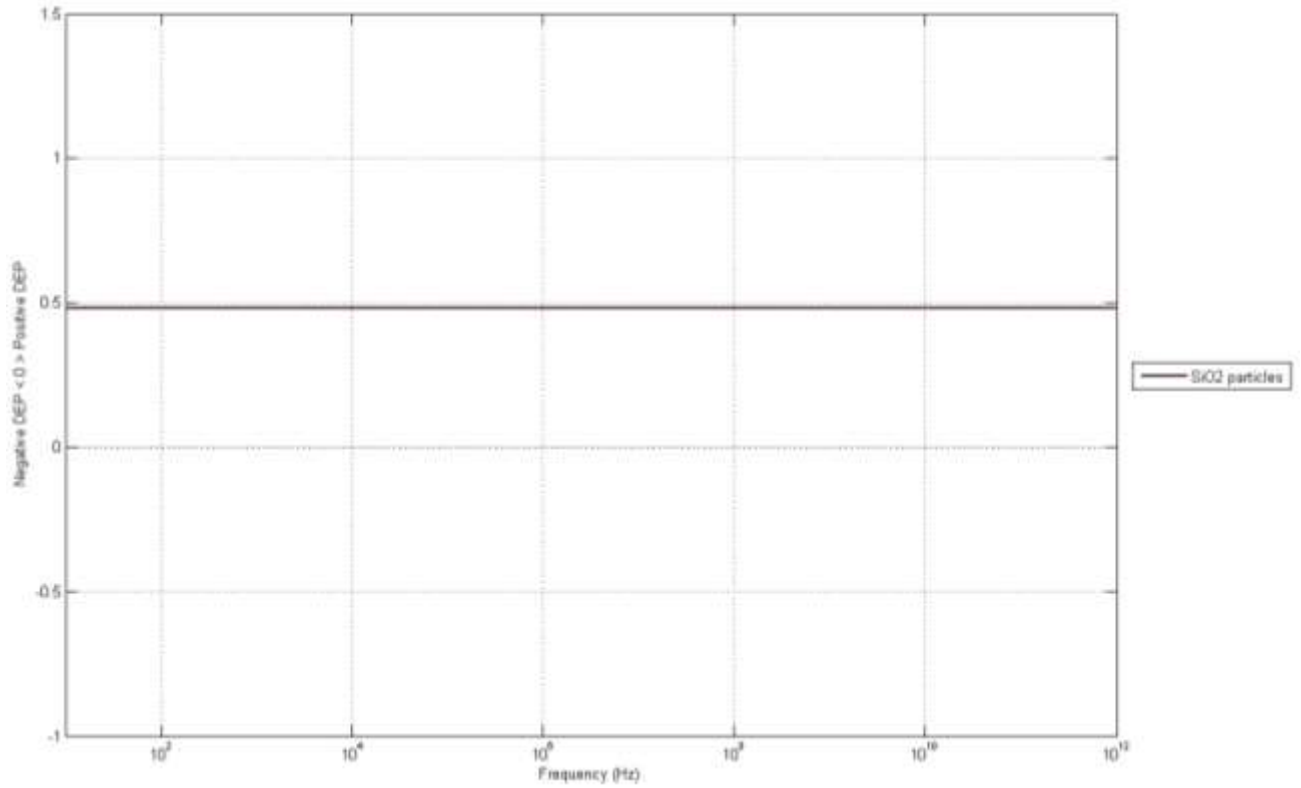


Figure 16 Clausius-Mossotti Factor of SiO₂ particle vs. Frequency

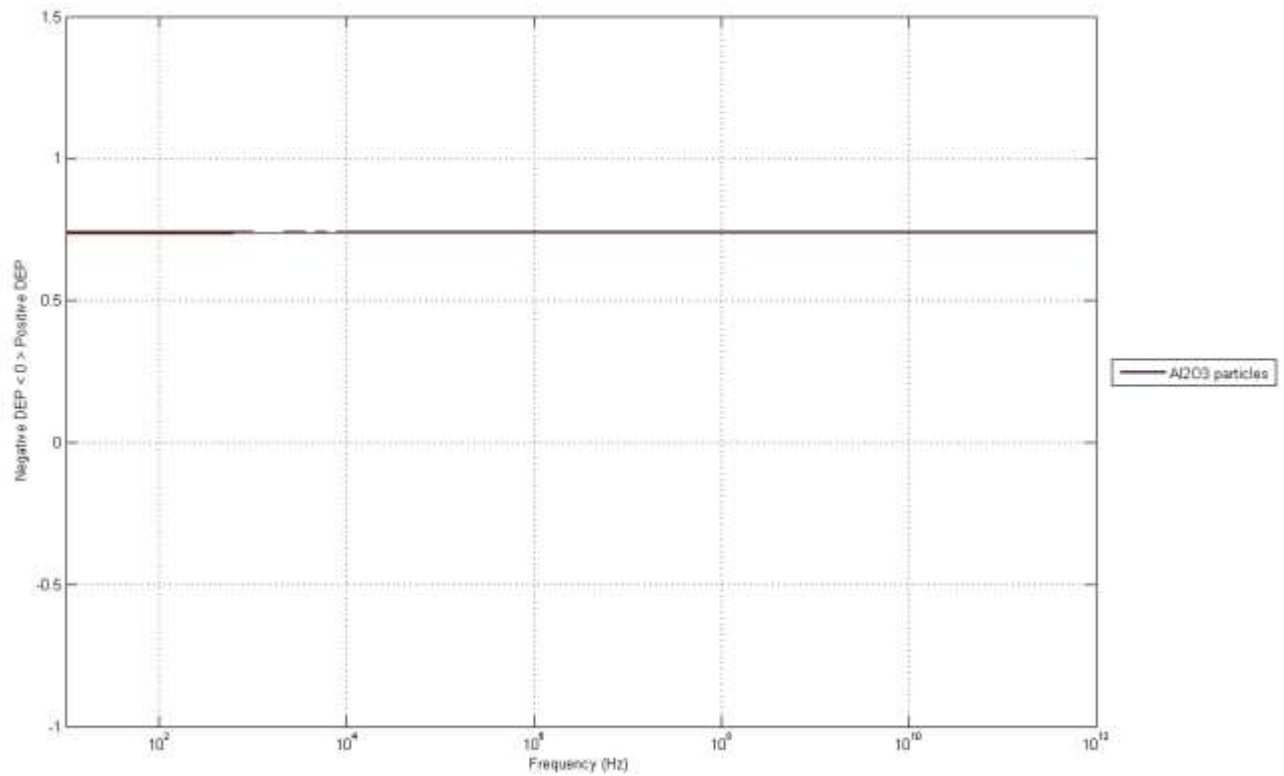


Figure 17 Clausius-Mossotti Factor of Al₂O₃ particle vs. frequency

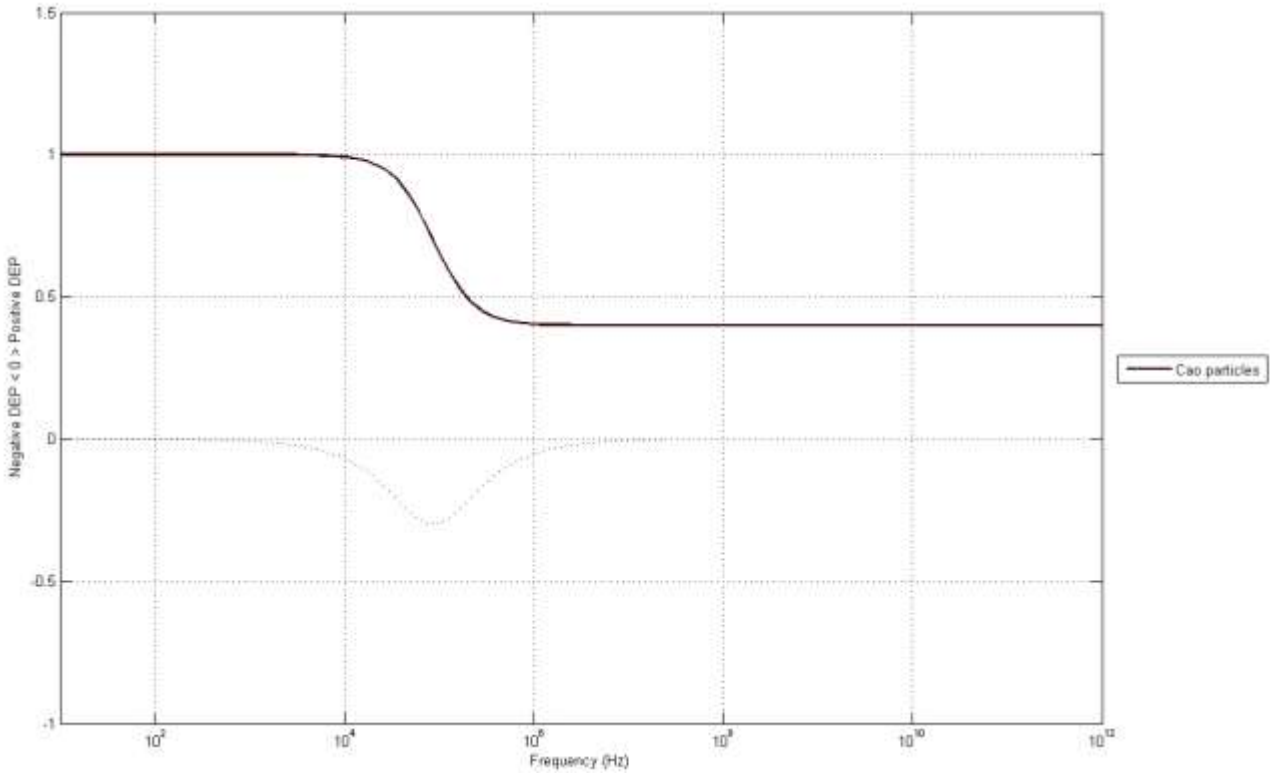


Figure 18 Clausius-Mossotti Factor of CaO particle vs. frequency

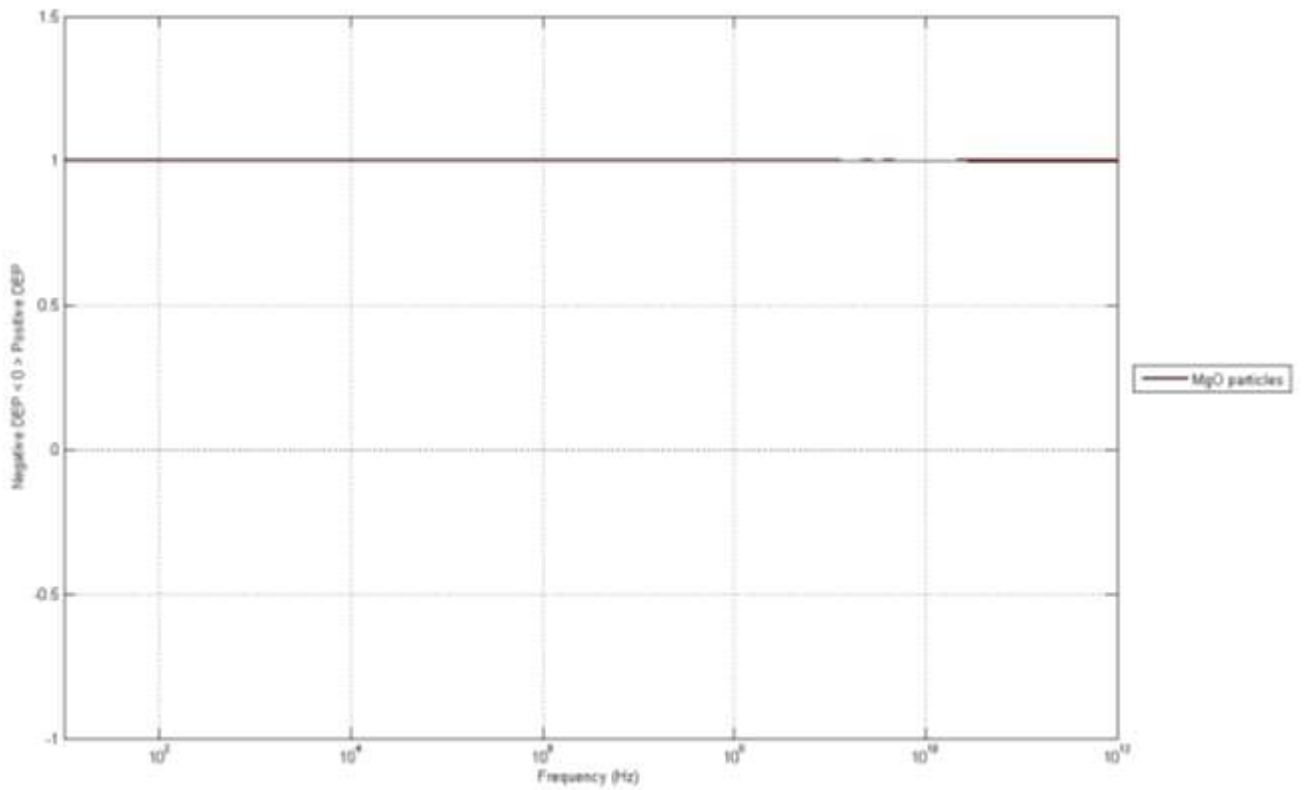


Figure 19 Clausius-Mossotti Factor of MgO particle vs. frequency

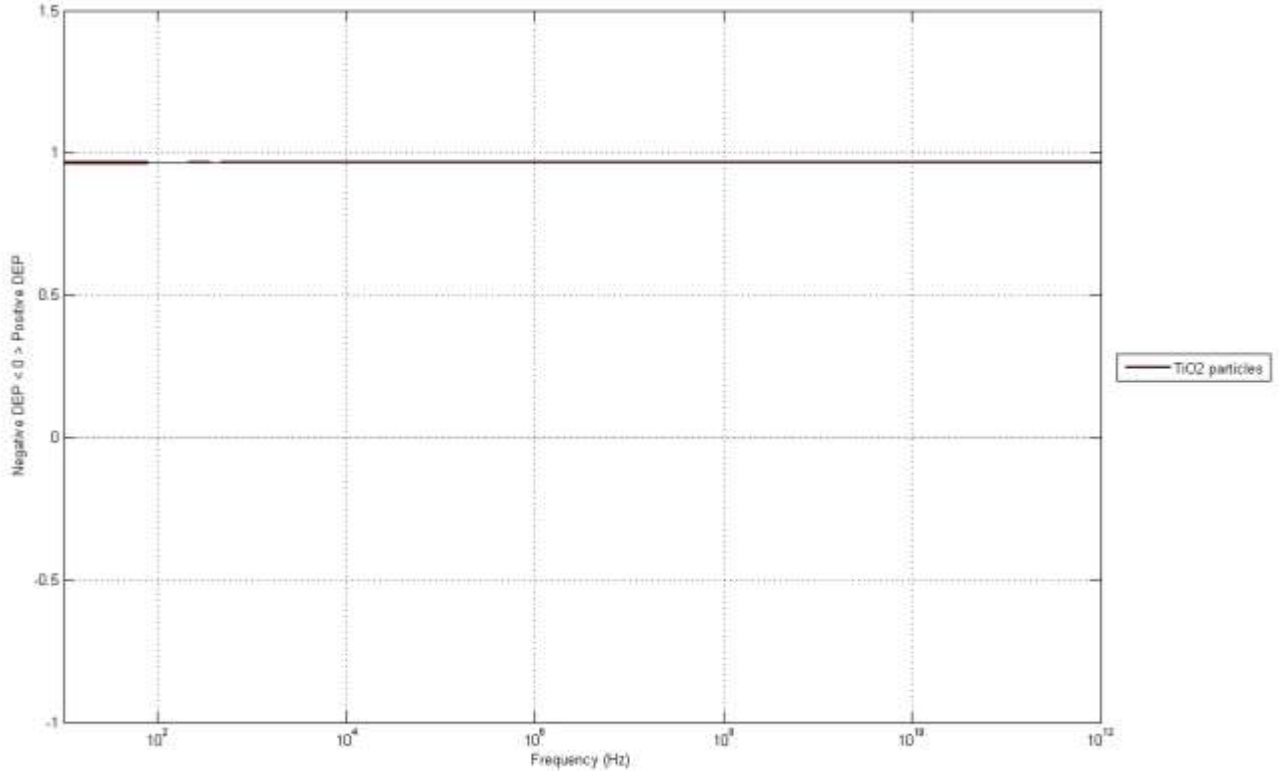


Figure 20 Clausius-Mossotti Factor of TiO₂ particle vs. frequency

Table XII Summary of Clausius Mossotti Factors

Material	Clausius-Mossotti	Figures
SiO ₂	0.48	15
Al ₂ O ₃	0.75	16
CaO	0.45 to 1.0	17
MgO	1.0	18
TiO ₂	0.95	19

Based on the Clausius Mossotti Factors stated above, the particles will experience positive DEP. This is an encouraging indication that dielectrophoresis will collect particles. However, this is just one factor influencing the outcome.

2. COMPUTATIONAL FLUID DYNAMICS SIMULATION (2D)

The computational fluid dynamics analysis was performed using Comsol 3.5a and the boundary condition shown in Figure 21. An incompressible Navier Stokes solver was used for the analysis. The fluid inlet velocity and outlet pressure were uniformly applied on the respective boundaries. The velocity magnitude was changed for each simulation, but the outlet pressure was set at zero for all simulations. The no slip boundary condition was applied to the horizontal boundaries for all simulations.

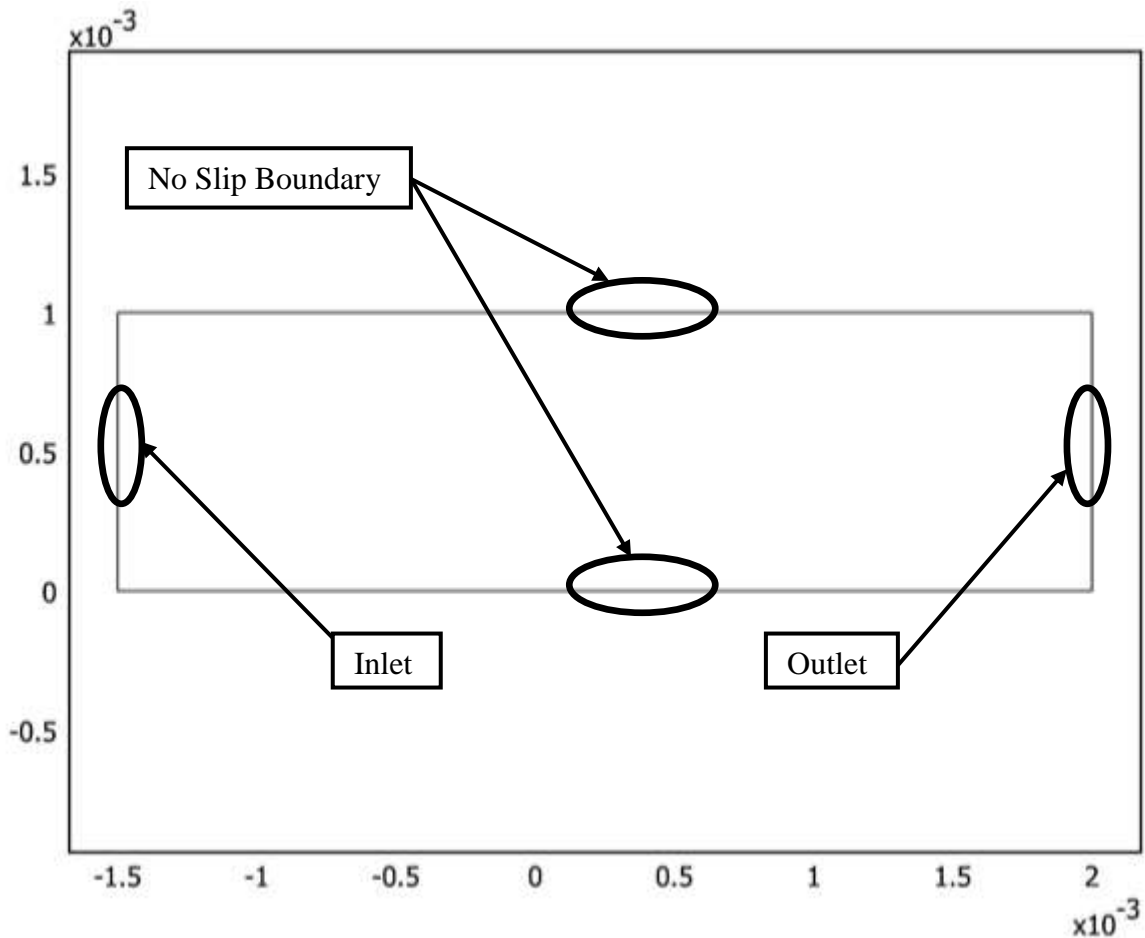


Figure 21: CFD boundary and Geometry Plot

Figure 22 is a computational fluid dynamics results plot with the inlet boundary velocity set to 0.01 m/s. The expected maximal velocity for a 2D channel is $\frac{3}{2}U_{ave} = U_{max}$. The maximal velocity in Figure 22 is 0.0153 m/s.

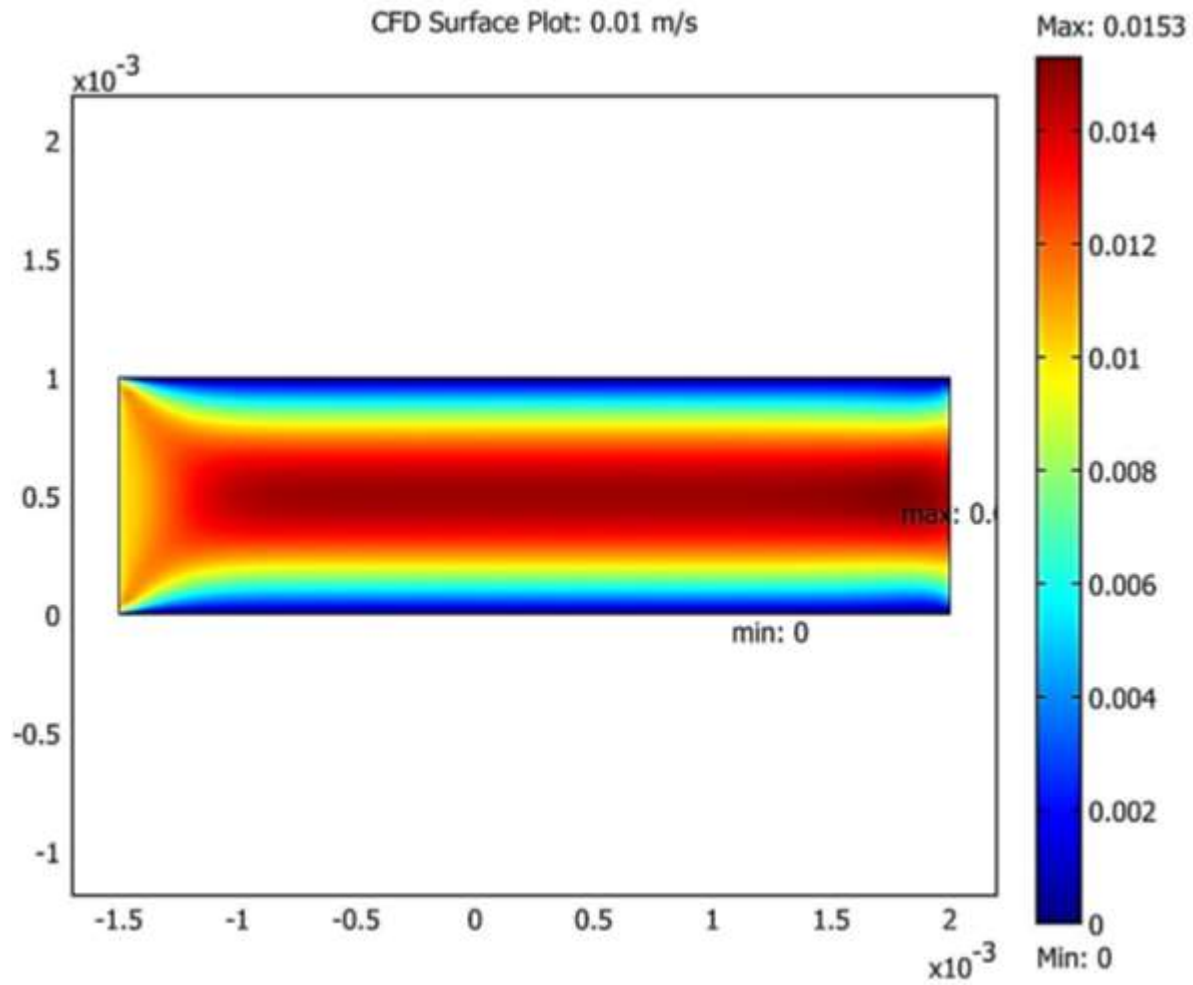


Figure 22: CFD Surface Plot; Velocity = 0.1 m/s

Figure 23 is a computational fluid dynamics results plot with the inlet boundary velocity set to 1.5 m/s. The expected maximal velocity for a 2D channel is $\frac{3}{2}U_{ave} = U_{max}$. The maximal velocity in Figure 23 is 2.25 m/s.

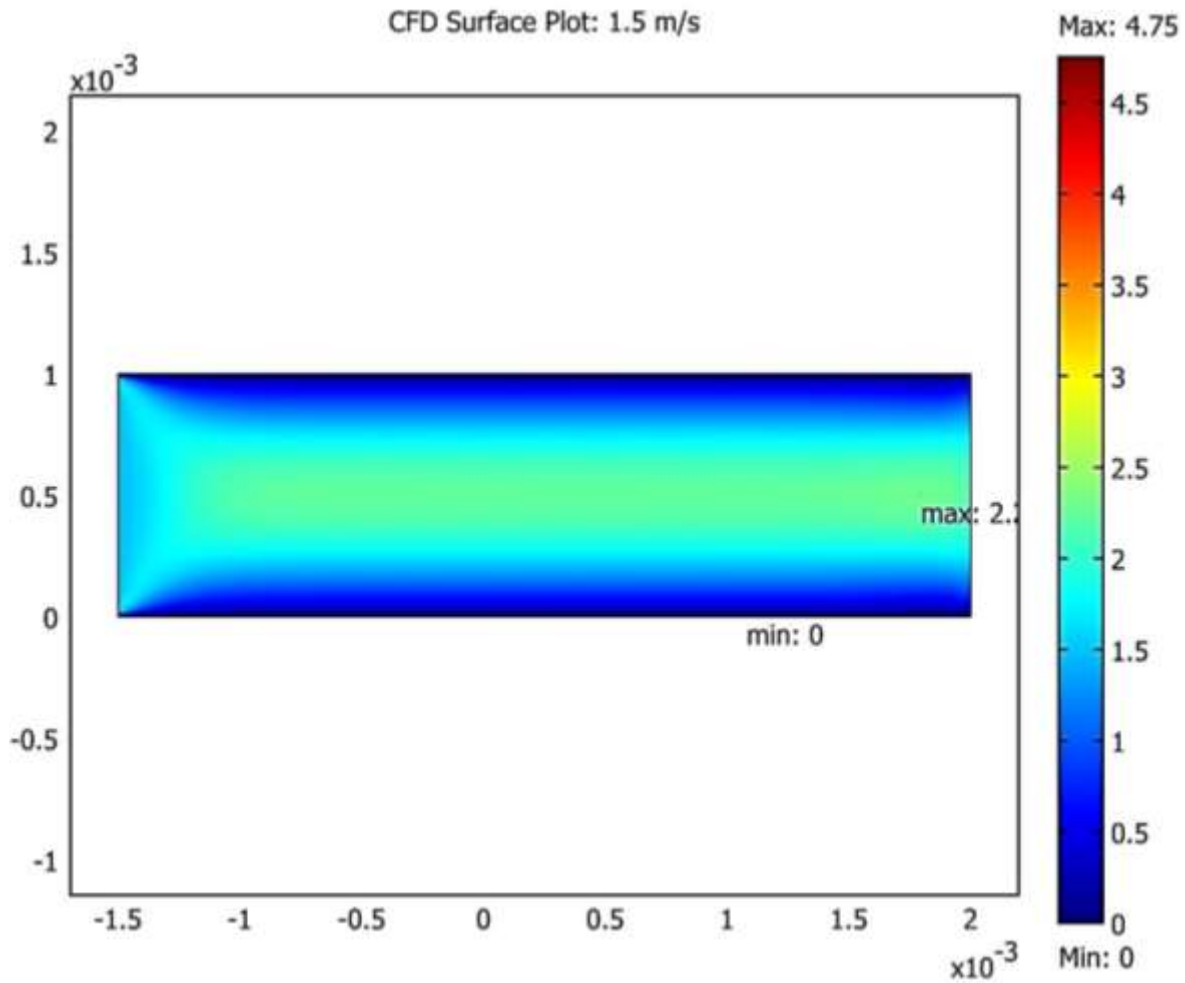


Figure 23 CFD Surface Plot; Velocity = 1.5 m/s

Figure 24 is a computational fluid dynamics results plot with the inlet boundary velocity set to 2.3 m/s. The expected maximal velocity for a 2D channel is $\frac{3}{2}U_{ave} = U_{max}$. The maximal velocity in Figure 24 is 3.5 m/s.

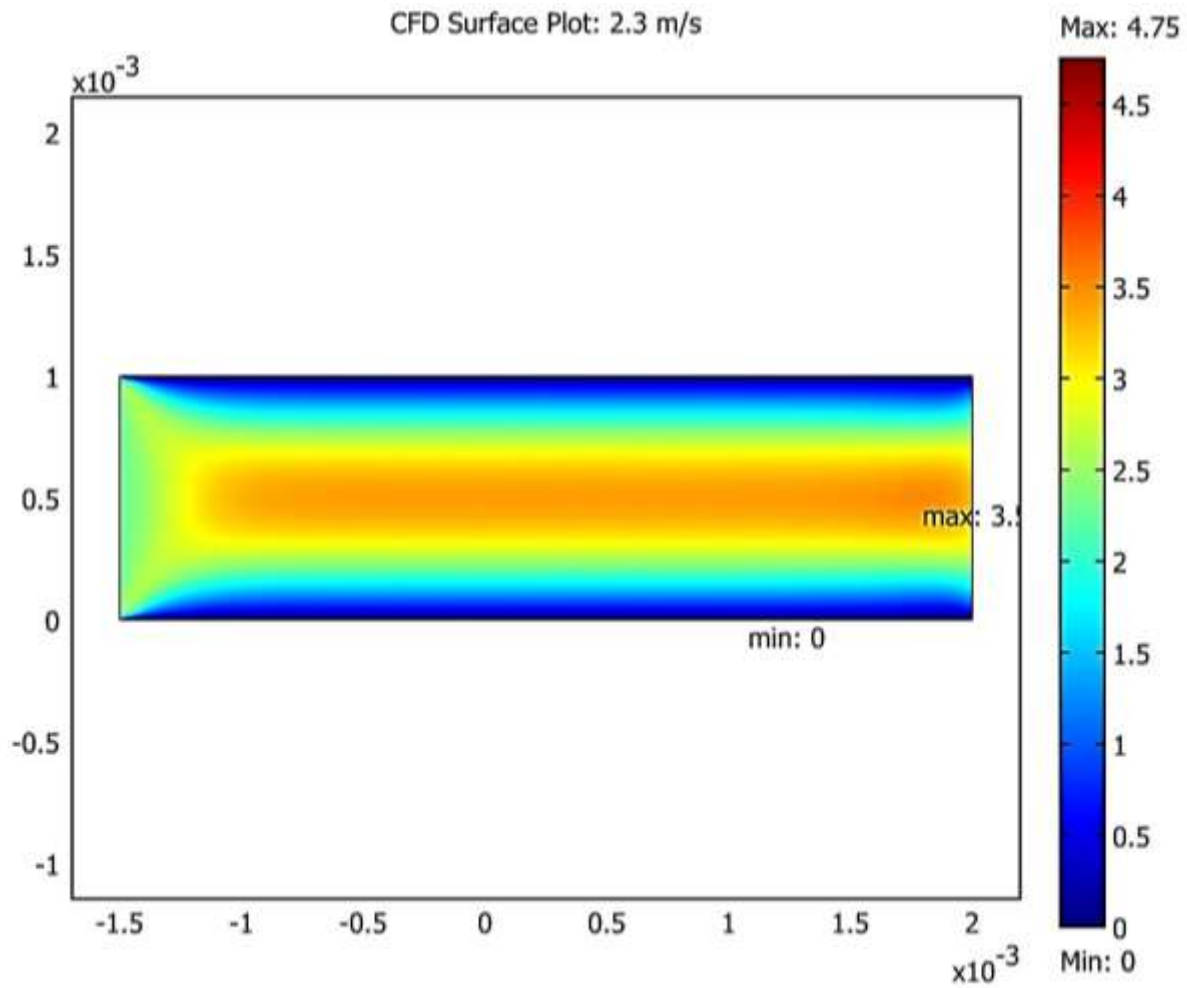


Figure 24 CFD Surface Plot; Velocity = 2.3 m/s

Figure 25 is a computational fluid dynamics results plot with the inlet boundary velocity set to 3.0 m/s. The expected maximal velocity for a 2D channel is $\frac{3}{2}U_{ave} = U_{max}$. The maximal velocity in Figure 25 is 4.5 m/s.

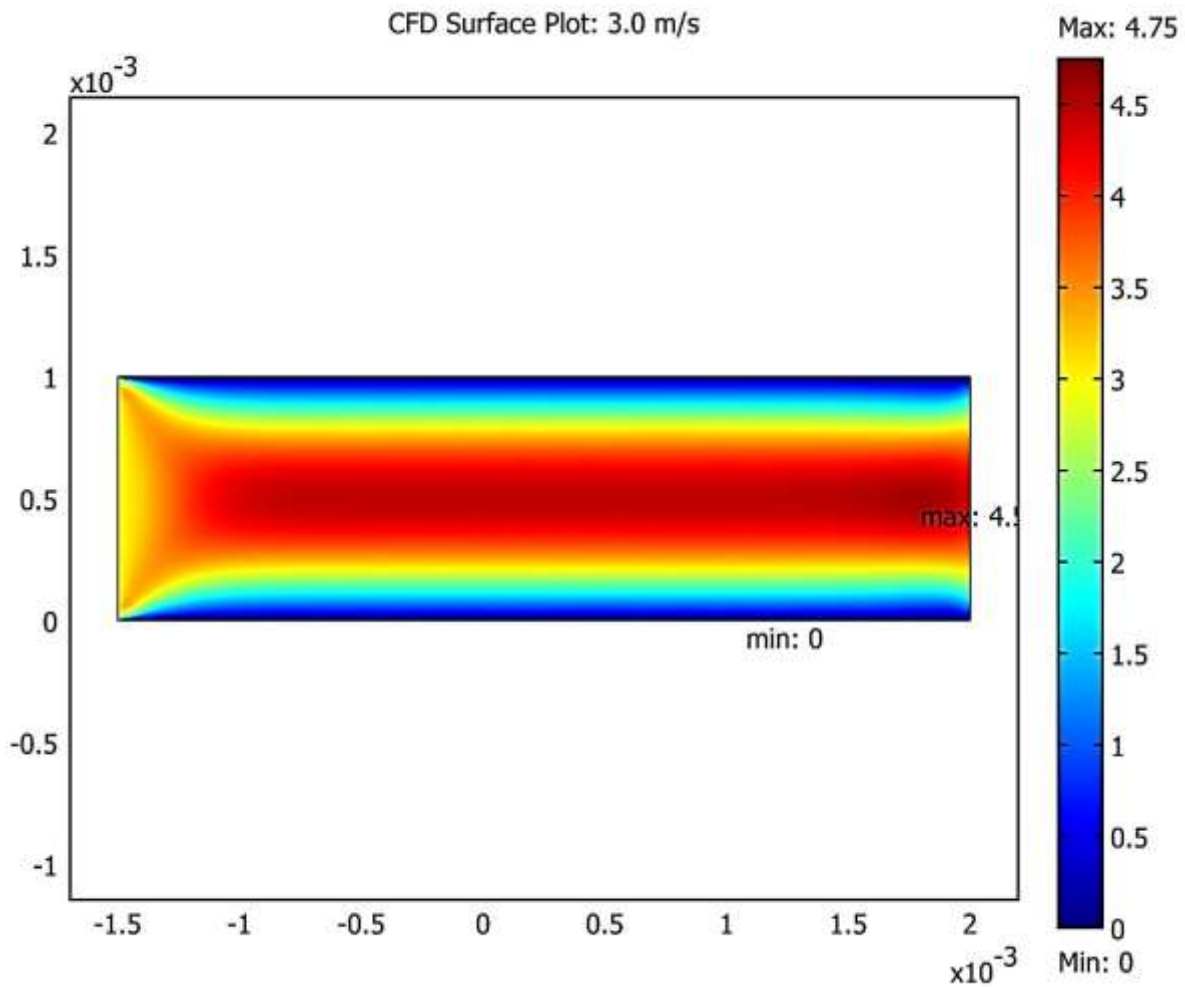


Figure 25 CFD Surface Plot; Velocity = 3.0 m/s

3. DIELECTROPHORESIS SIMULATION

The dielectrophoresis analysis was performed with the boundary conditions shown in Figure 26. This analysis was performing using Poisson Equation and the voltage varied from 100V to 300V. The radius of the particle was set to a constant value of 4 μ m. The radius of the particle was chosen to be 4 μ m to match the geometric mean radius of the test dust used during testing. The relative permittivity of the medium and the free space were set to a value of $1.00059\frac{F}{m}$, and $8.845E-12\frac{F}{m}$ respectively. The Clausius-Mossotti factor was set to a constant value of 1 for all simulations. The height of the channel was 3/8in to correspond to the test rig. The length was specified to insure that the fluid inlet and outlet boundaries were of adequate distance from the electrodes for the particle dynamic simulation.

The remaining geometric boundary conditions are a Neumann boundary condition. The boundaries that are above the electrode array are set to a Neumann boundary condition for the reason that these, geometric boundaries are of adequate distance from the electrodes being at distances much greater than that the electrode dimensions. The boundary conditions between the electrodes are set as a Neumann boundary condition. This assumption is based on the fact that both the potential and normal component of the total current is continuous. This assumption will not hold true for this work. The normal component of the electric field in the electrolyte at the interface is not negligible compared to that of the glass. Consequently, this space cannot be simplified to just the electrolyte. Nevertheless, for this work we will make this assumption.

The results of the analysis were plotted of the $\log_{10}(F_{dep})$ of the dielectrophoretic force. The purpose of plotting the $\log_{10}(F_{dep})$ is to linearize the results for mapping. Otherwise, the results would be confined to the space directly above the electrodes.

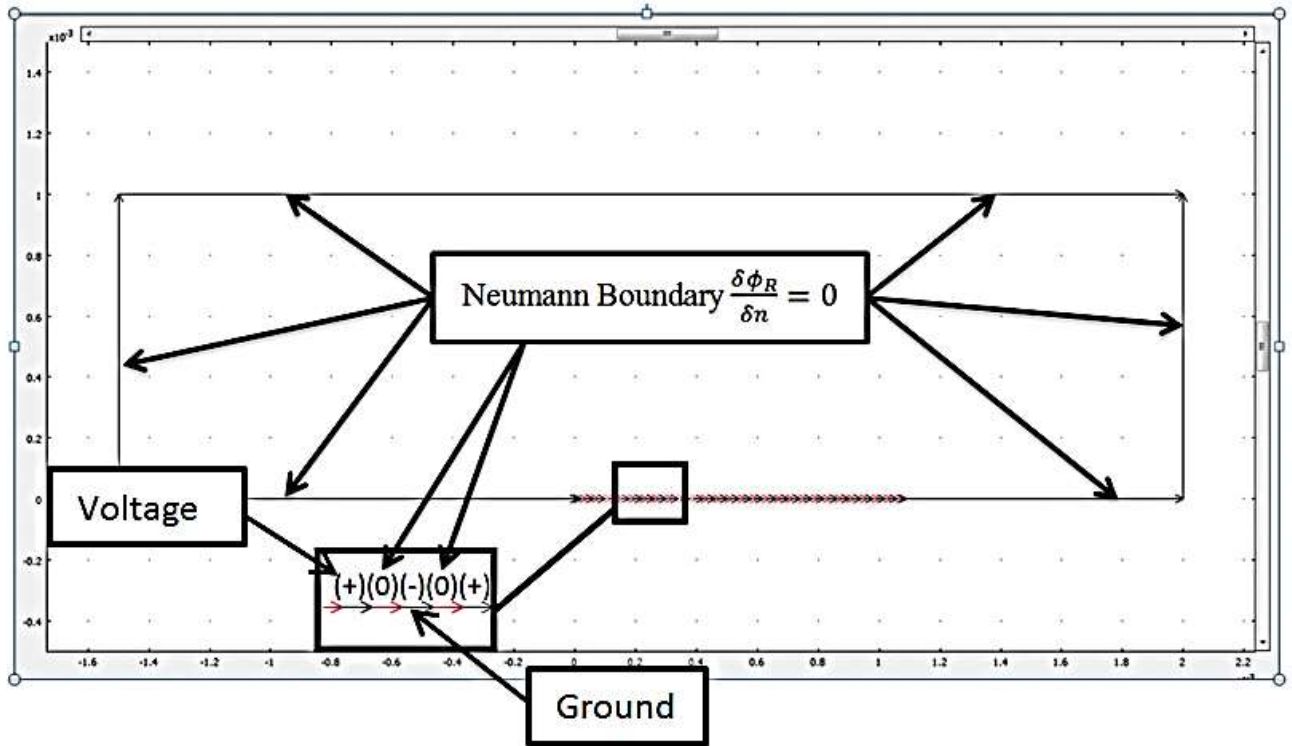


Figure 26: DEP Electrode Array Design and Boundary Conditions

Figure 27 is a $\log_{10}(F_{dep})$ plot of the dielectrophoretic force with the input voltages set to a value of 100V. The $\log_{10}(F_{dep})$ of the dielectrophoretic force in Figure 25 has a maximum value at the ends of the electrode array; reaching $3.80 \log_{10}(F_{dep})$. There is a minimum value located in the upper part of the channel of $-17.28 \log_{10}(F_{dep})$.

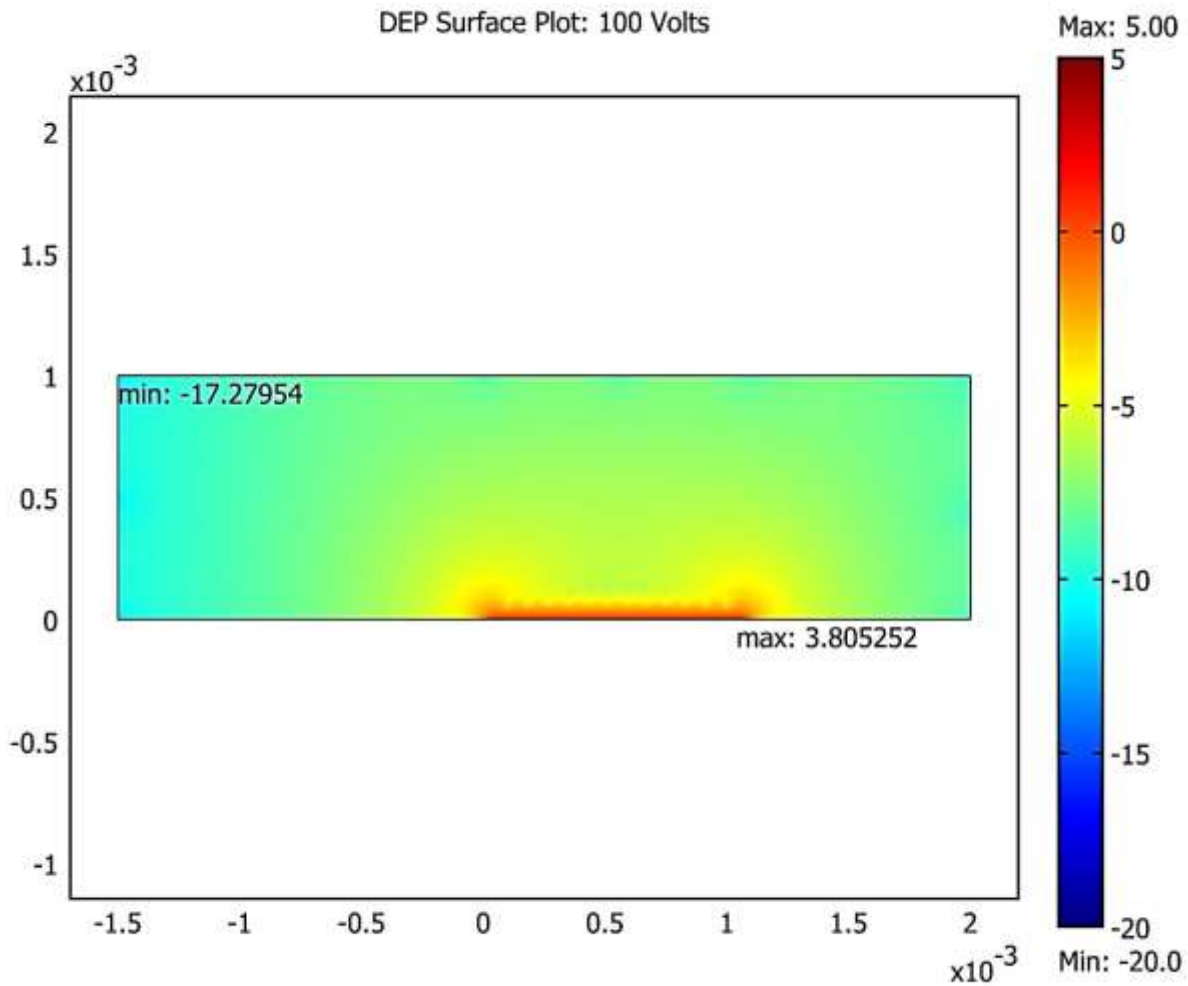


Figure 27: DEP Surface Plot of $\log_{10}(F_{dep})$: 100V

Figure 28 is a $\log_{10}(F_{dep})$ plot of the dielectrophoretic force with the input voltages set to a value of 150V. The $\log_{10}(F_{dep})$ of the dielectrophoretic force in Figure 28 has a maximum value at the ends of the electrode array of $4.16 \log_{10}(F_{dep})$. There is a minimum value located in the upper part of the channel of $-16.93 \log_{10}(F_{dep})$.

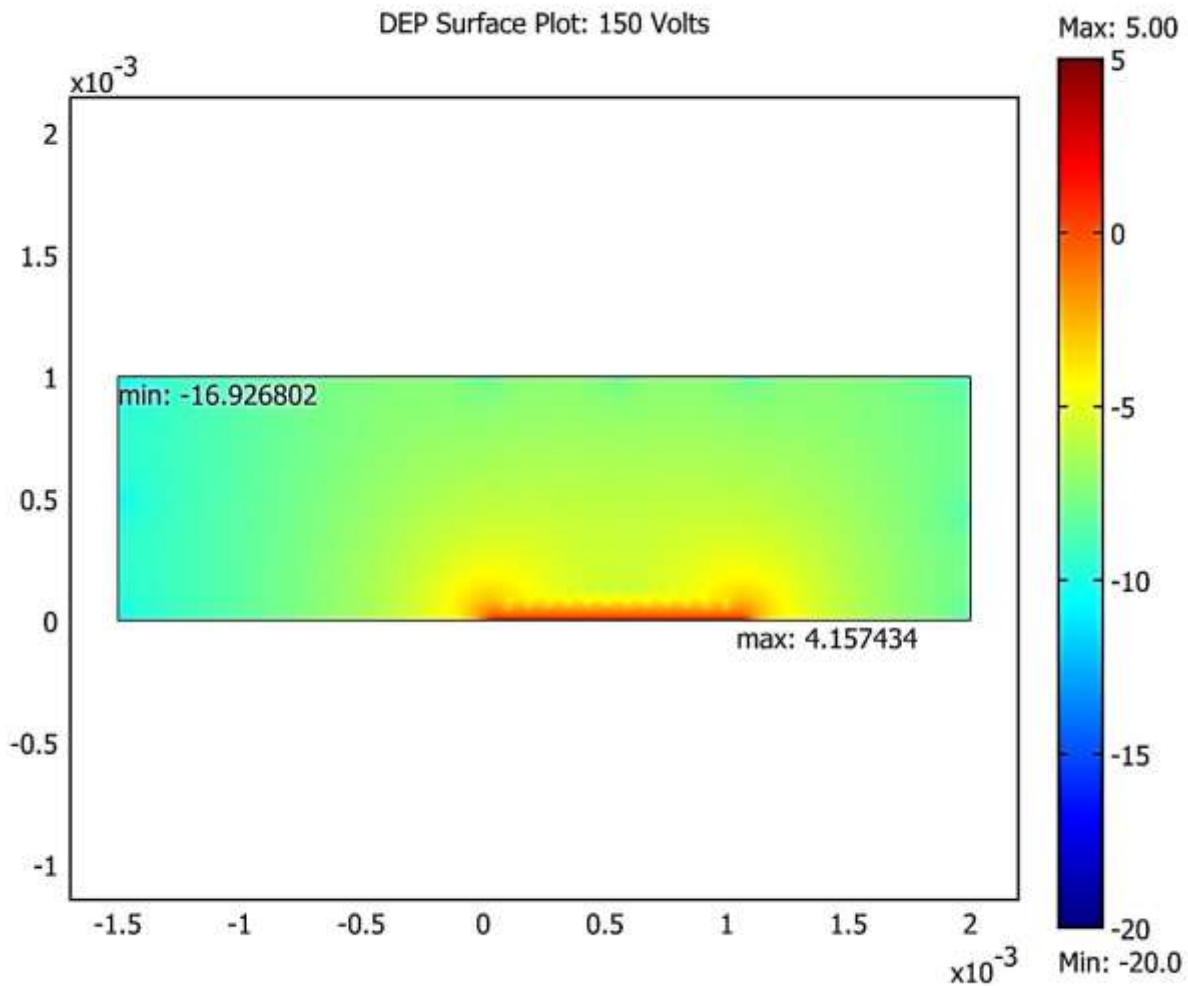


Figure 28 DEP Surface Plot of $\log_{10}(F_{dep})$: 150V

Figure 29 is a $\log_{10}(F_{dep})$ plot of the dielectrophoretic force with the input voltages set to a value of 200V. The $\log_{10}(F_{dep})$ of the dielectrophoretic force in Figure 29 has a maximum value at the ends of the electrode array of $4.41 \log_{10}(F_{dep})$. There is a minimum value located in the upper part of the channel of $-16.68 \log_{10}(F_{dep})$.

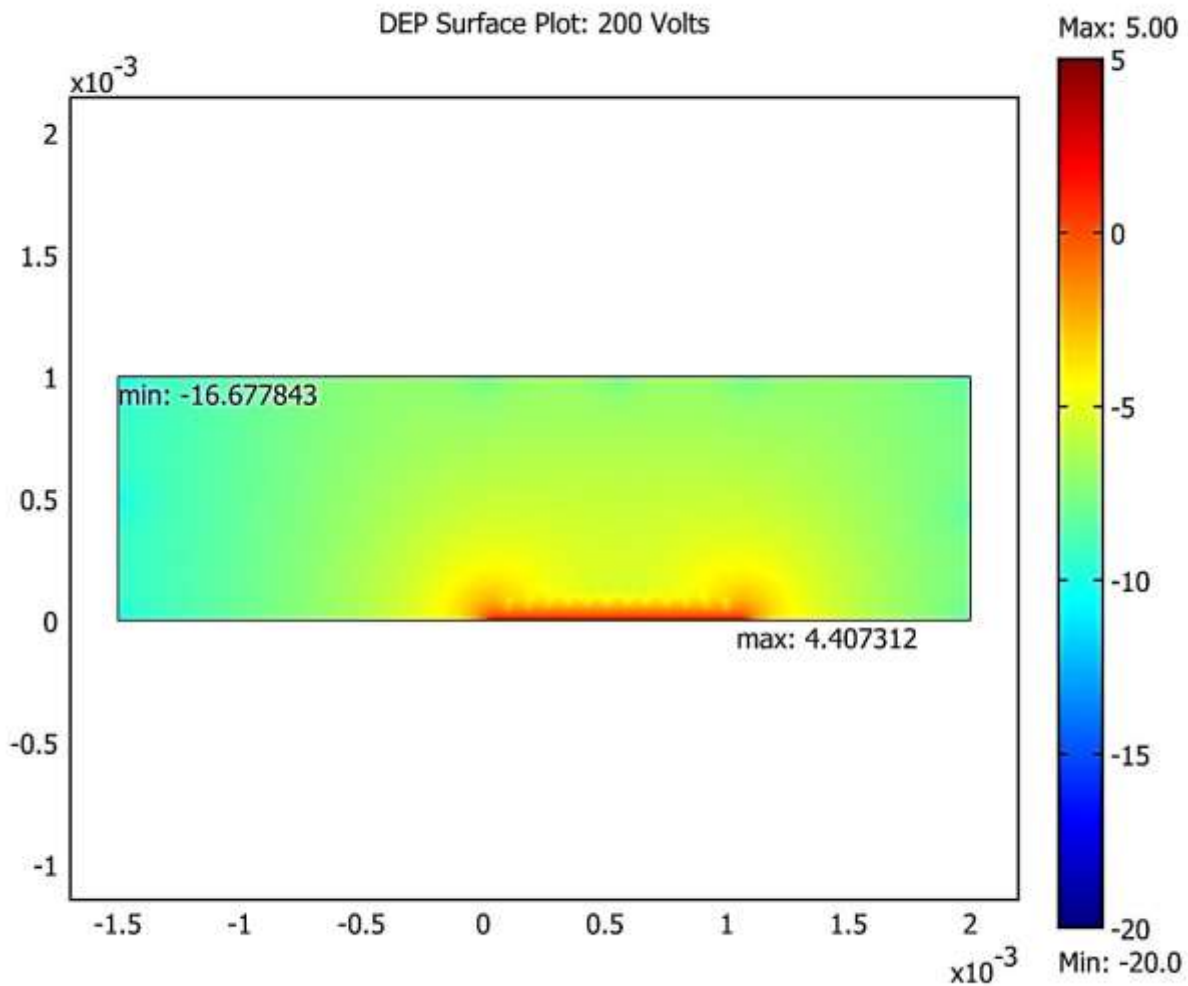


Figure 29 DEP Surface Plot of $\log_{10}(F_{dep})$: 200V

Figure 28 is a dielectrophoretic force results plot with the input voltages set to 150V. The dielectrophoretic force in Figure 28 has a maximum force at the ends of the electrode array channel; reaching $4.60 \log_{10}(F_{dep})$. There is a minimum of $-16.48 \log_{10}(F_{dep})$ in the upper part of the channel.

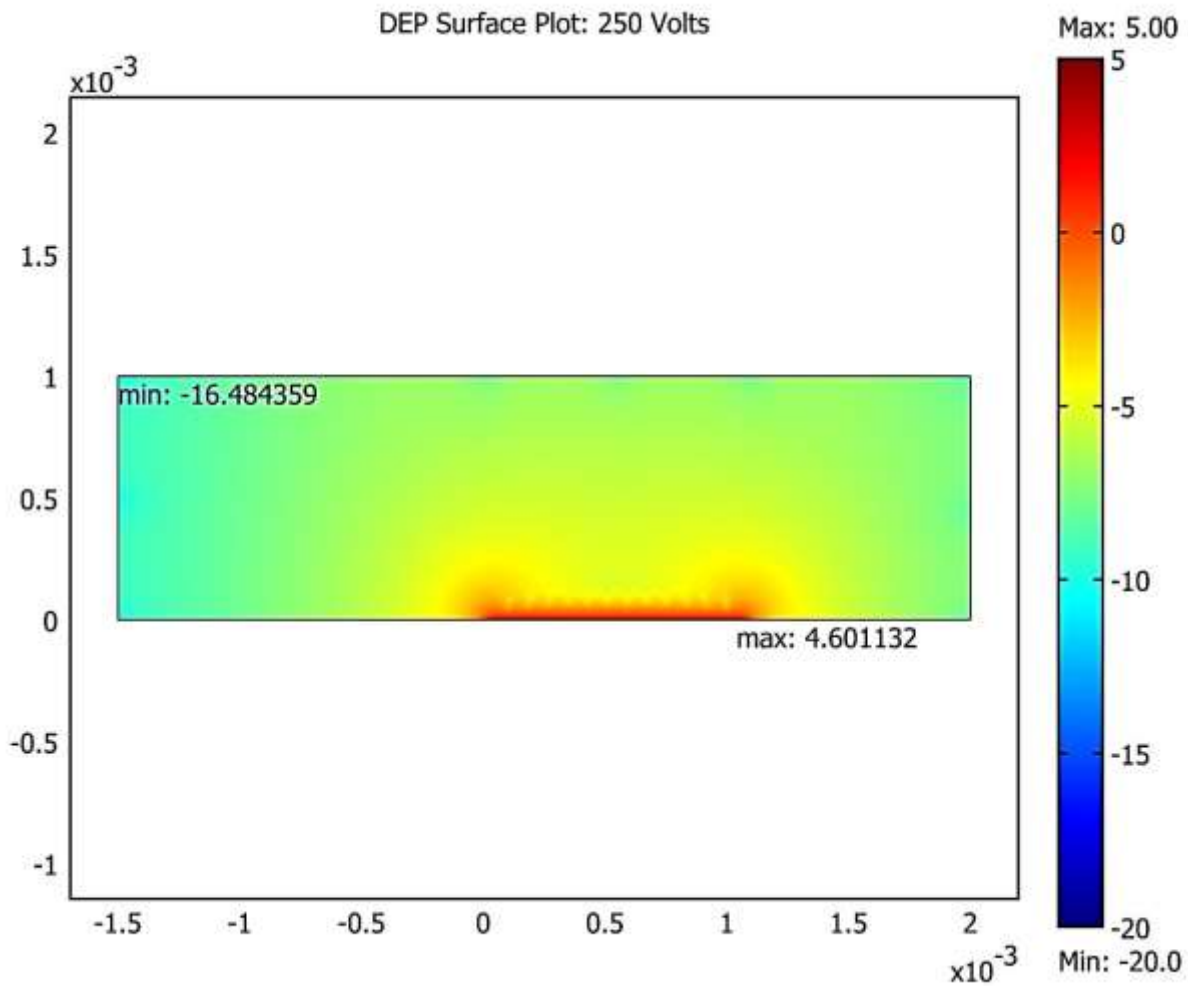


Figure 30 DEP Surface Plot of $\log_{10}(F_{dep})$: 250V

Figure 29 is a dielectrophoretic force results plot with the input voltages set to 300V. The dielectrophoretic force in Figure 25 has a maximum force at the ends of the electrode array channel; reaching $4.76 \log_{10}(F_{dep})$. There is a minimum of $-16.33 \log_{10}(F_{dep})$ in the upper part of the channel.

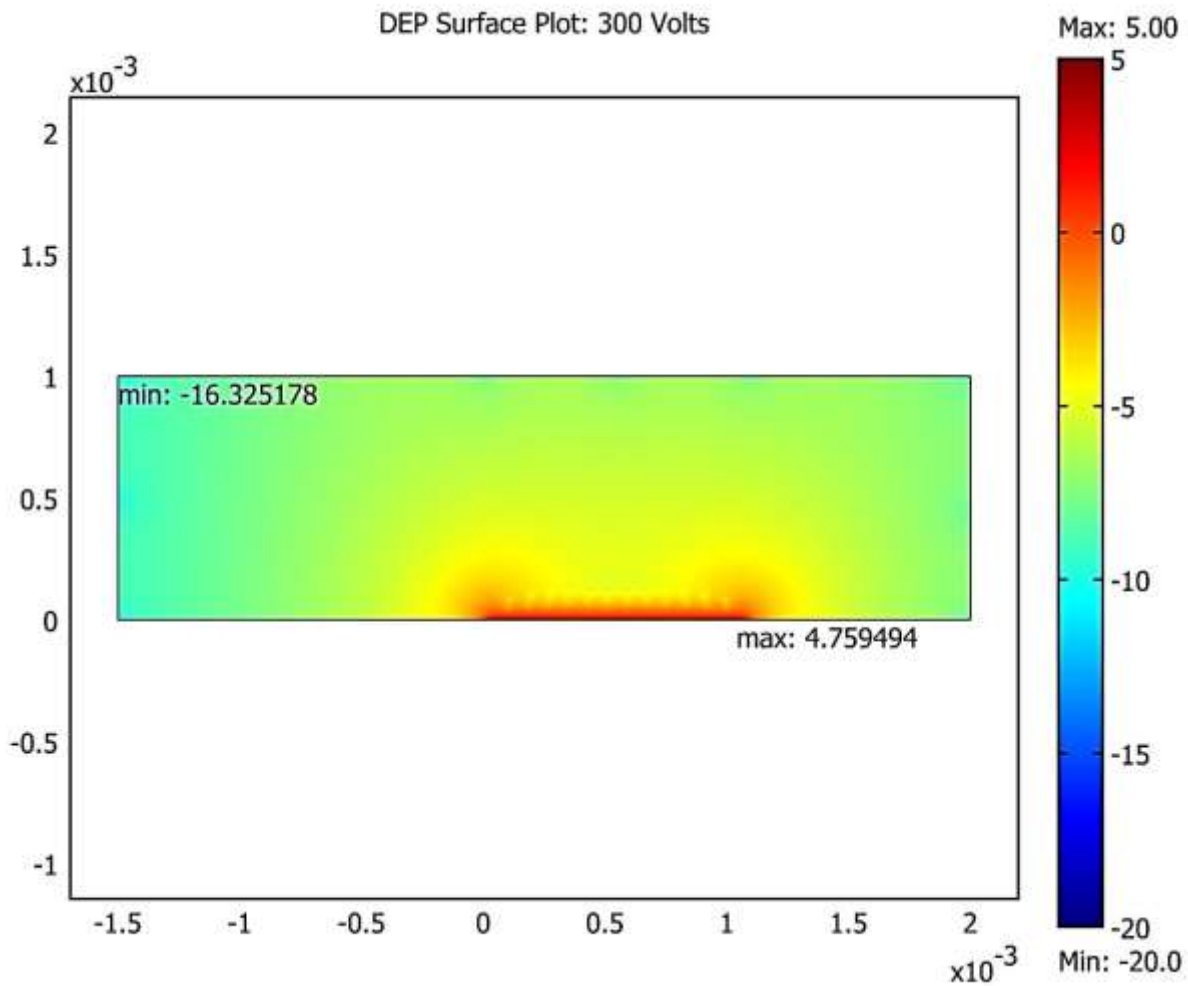


Figure 31 DEP Surface Plot of $\log_{10}(F_{dep})$: 300 V

4. COMBINATION DIELECTROPHORESIS VELOCITY AND FLUID VELOCITY SIMULATION

Dielectrophoretic velocity is the velocity of a particle that is imparted on a particle when it enters a non-uniform electric field. The dielectrophoretic velocity can be determined by dividing the dielectrophoretic force by the friction factor of the particle as shown in equation 37.

$$u_{DEP} = \frac{\pi r^3 \epsilon_m RE[f_{cm}] \nabla E^2}{6\pi\eta r} \quad (37)$$

where, r is the radius of the particle, ϵ_m is the permittivity of the medium, $RE[f_{cm}]$ is the real part of the Clausius-Mossotti factor, E is the electric field, and η is the viscosity of the fluid.

Equation 37 shows that for spherical particles, the velocity is dependent on two areas of interest. First, the geometry and material makeup of the particle are a determining factor in the final value of the velocity. For example, the radius of the particle is cubed. The other area of importance is the properties of the fluid medium. For example, as the value of the fluid viscosity increases the slower the particle velocity. In this simulation the particles reach terminal velocity.

Figure 32 is a dielectrophoretic velocity combined with the fluid velocity resulting in normalized arrow plot showing the directional vector of the combination of these velocities.

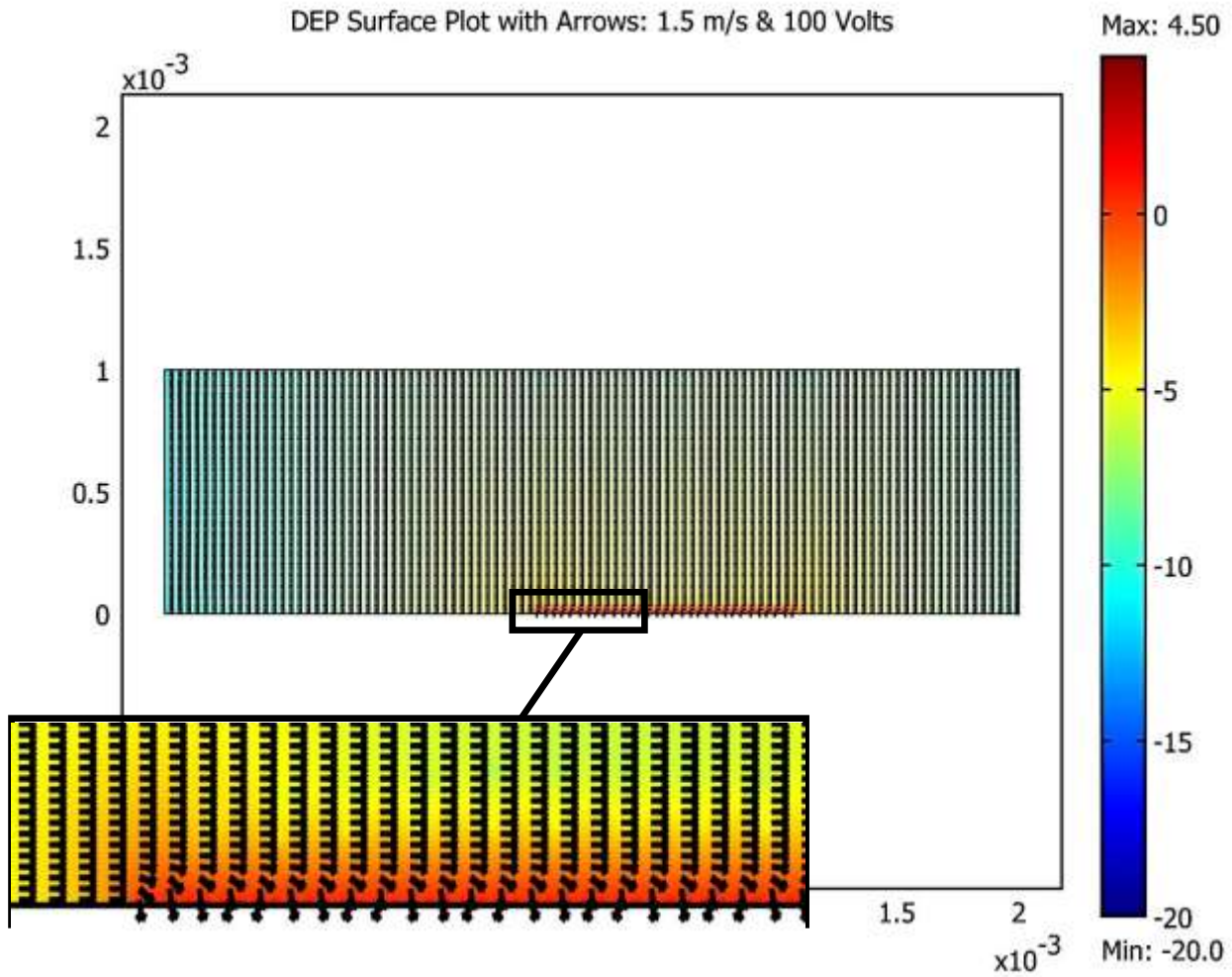


Figure 32: Combination of dielectrophoresis velocity and fluid velocity

5. PARTICLE TRACING SIMULATION

Particle tracing simulation shows the behavior of a particle under the influence of fluid and DEP forces. This analysis all occurs from an origin, in this case they enter from fluid inlet boundary and travel through the electrical field and then the fluid outlet. The particle size diameter used for this analysis is $4\mu\text{m}$. The applied voltage and fluid velocity varied for each analysis.

Figure 33 is a dielectrophoretic surface plot overlaid with the results of the particle tracing analysis. The air velocity in Figure 33 was set to 1.5 m/s and the applied voltage was set to 100 volts.

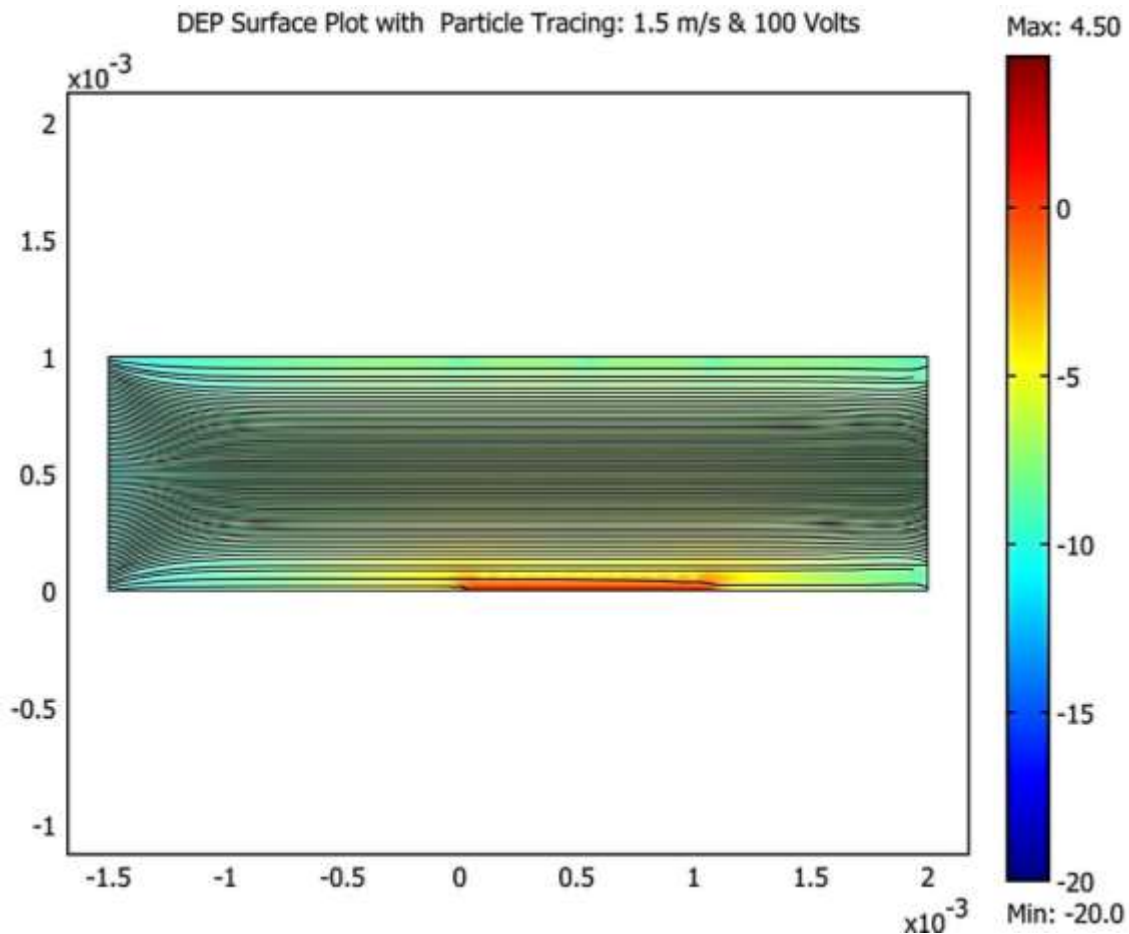


Figure 33 Particle Tracing Plot: air velocity is 1.5 m/s and applied voltage value of 100 V

Figure 34 is a dielectrophoretic surface plot overlaid with the results of the particle tracing analysis. The air velocity in Figure 34 was set to 1.5 m/s and the applied voltage was set to 200 volts.

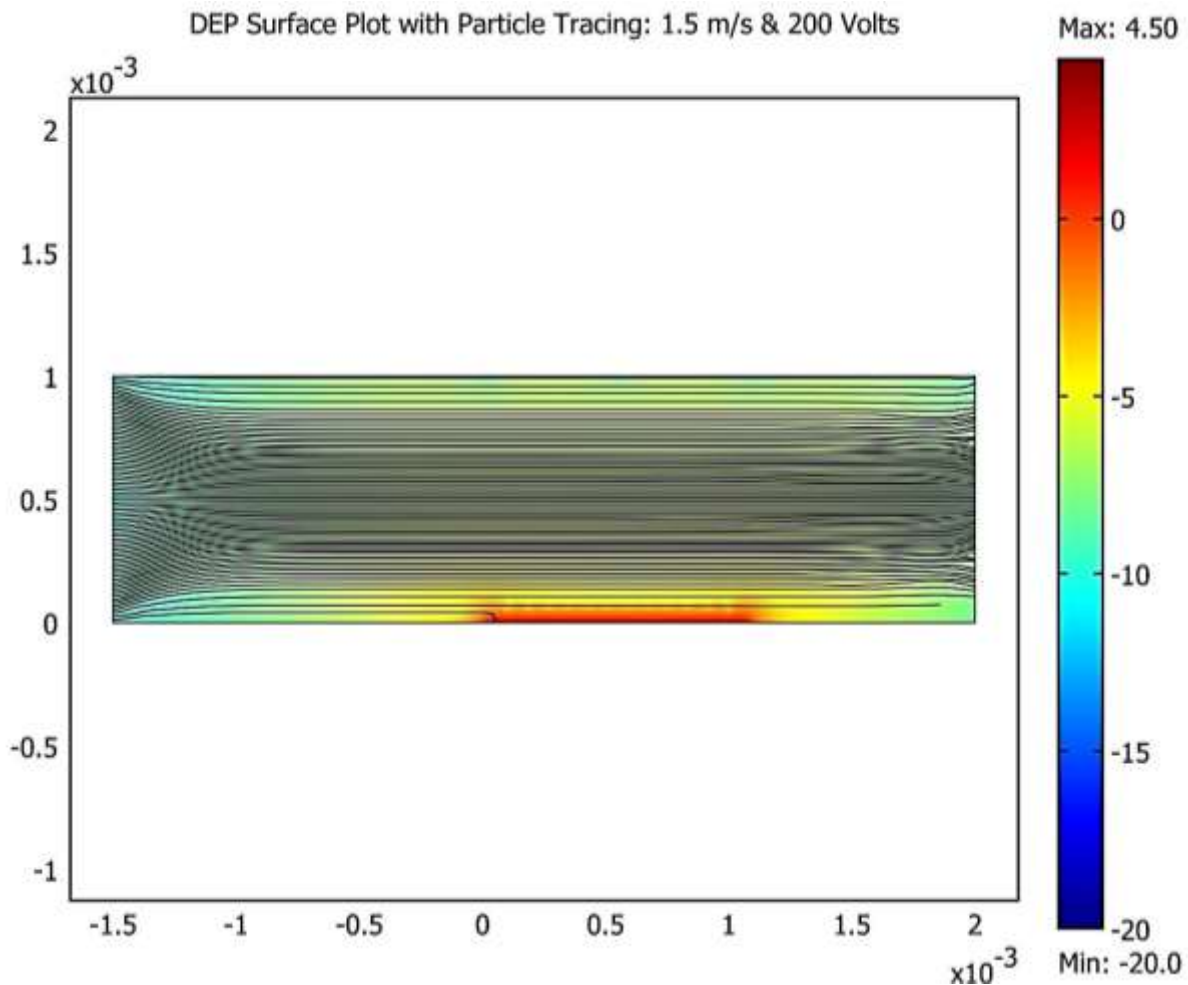


Figure 34 Particle Tracing Plot: air velocity is 1.5 m/s and applied voltage value of 200 V

Figure 35 is a dielectrophoretic surface plot overlaid with the results of the particle tracing analysis. The air velocity in Figure 35 was set to 0.01 m/s and the applied voltage was set to 250 volts.

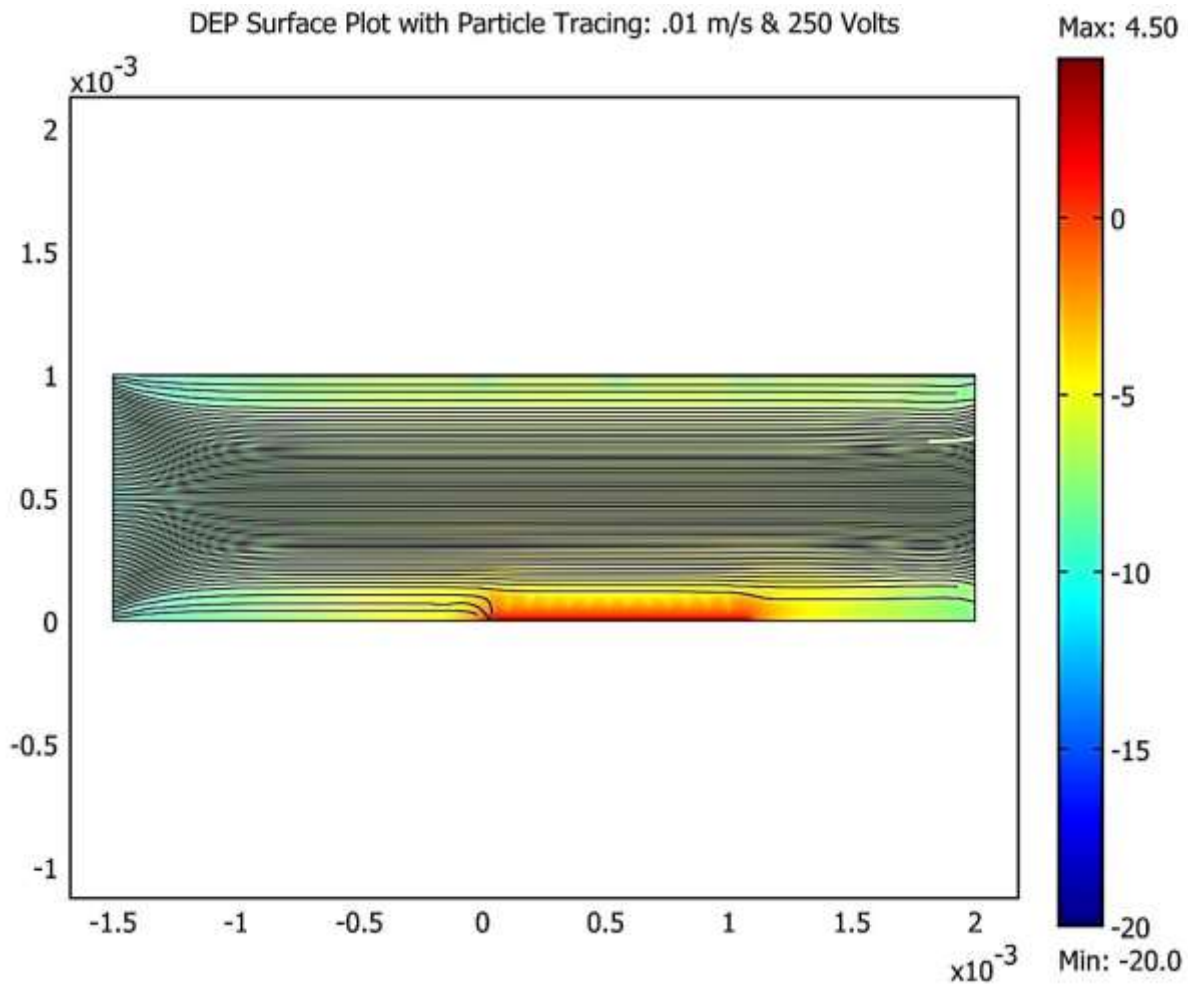


Figure 35 Particle Tracing Plot: air velocity is 0.01 m/s and applied voltage value of 250 V

Figure 36 is a dielectrophoretic surface plot overlaid with the results of the particle tracing analysis. The air velocity in Figure 36 was set to 1.5 m/s and the applied voltage was set to 300 volts.

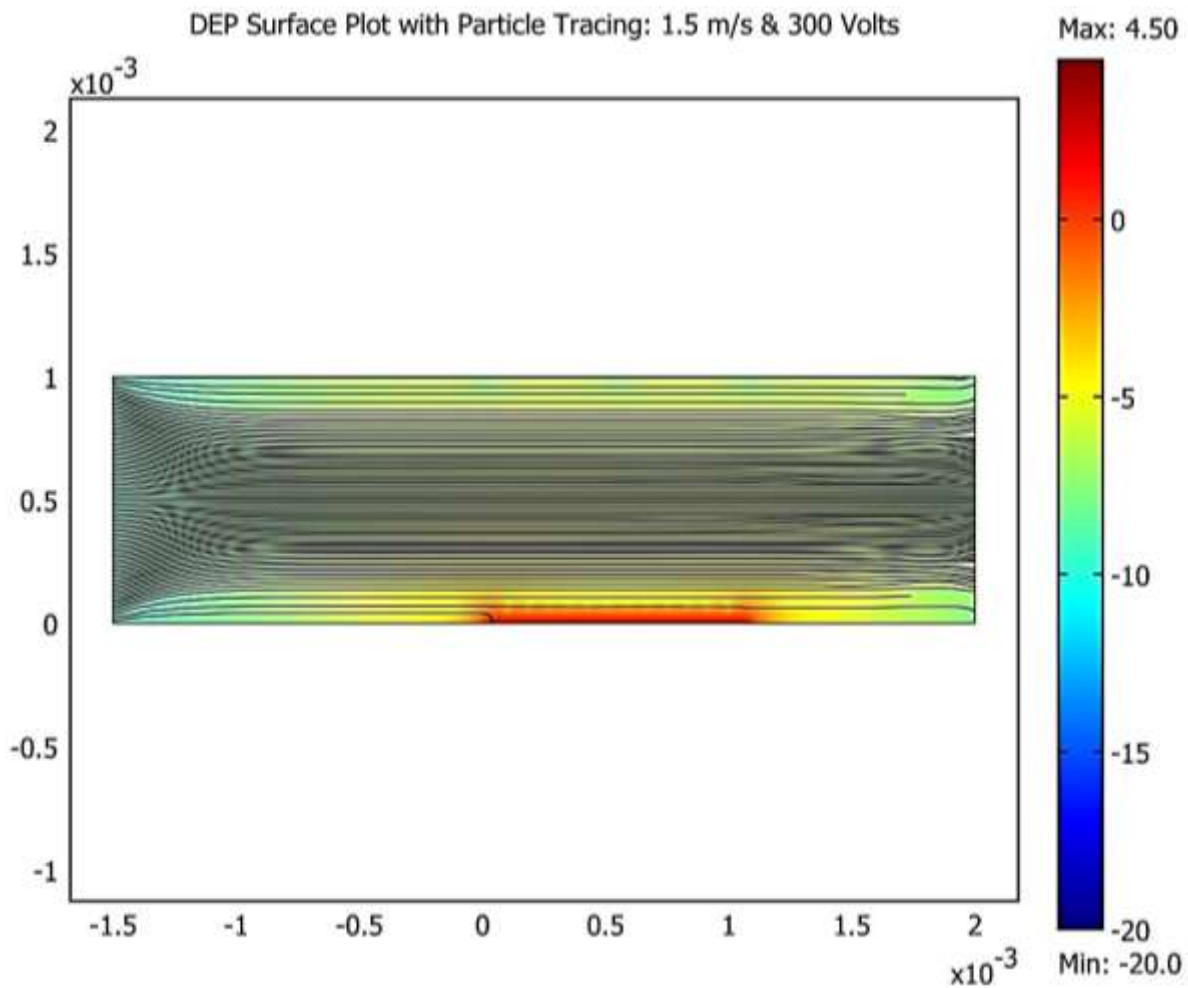


Figure 36 Particle Tracing Plot: air velocity is 1.5 m/s and applied voltage value of 300 V

Figure 37 is a dielectrophoretic surface plot overlaid with the results of the particle tracing analysis. The air velocity in Figure 37 was set to 2.3 m/s and the applied voltage was set to 300 volts.

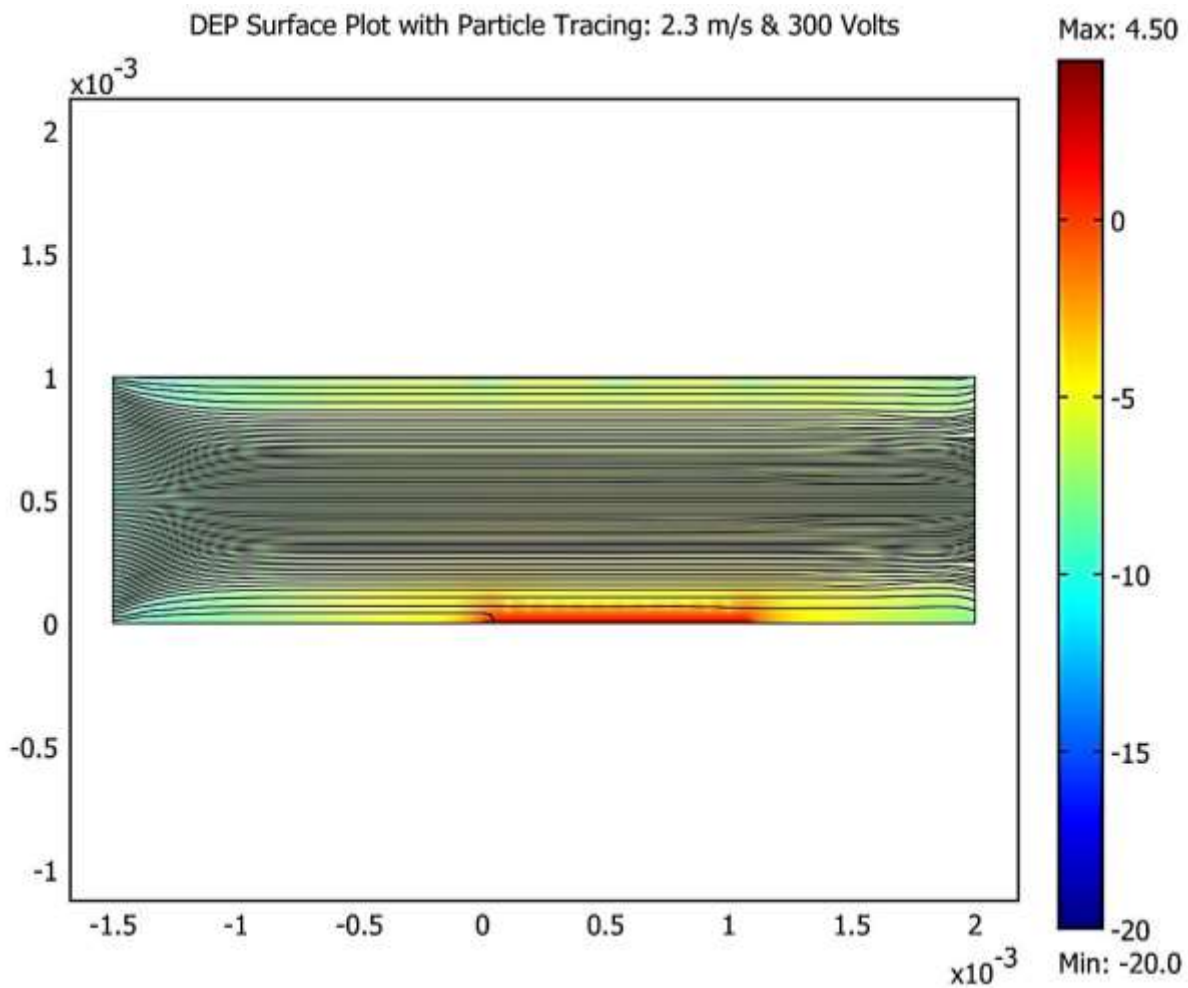


Figure 37 Particle Tracing Plot: air velocity is 2.3m/s and applied voltage value of 300V

Figure 38 is a dielectrophoretic surface plot overlaid with the results of the particle tracing analysis. The air velocity in Figure 38 was set to 3.0m/s and the applied voltage was set to 300 volts.

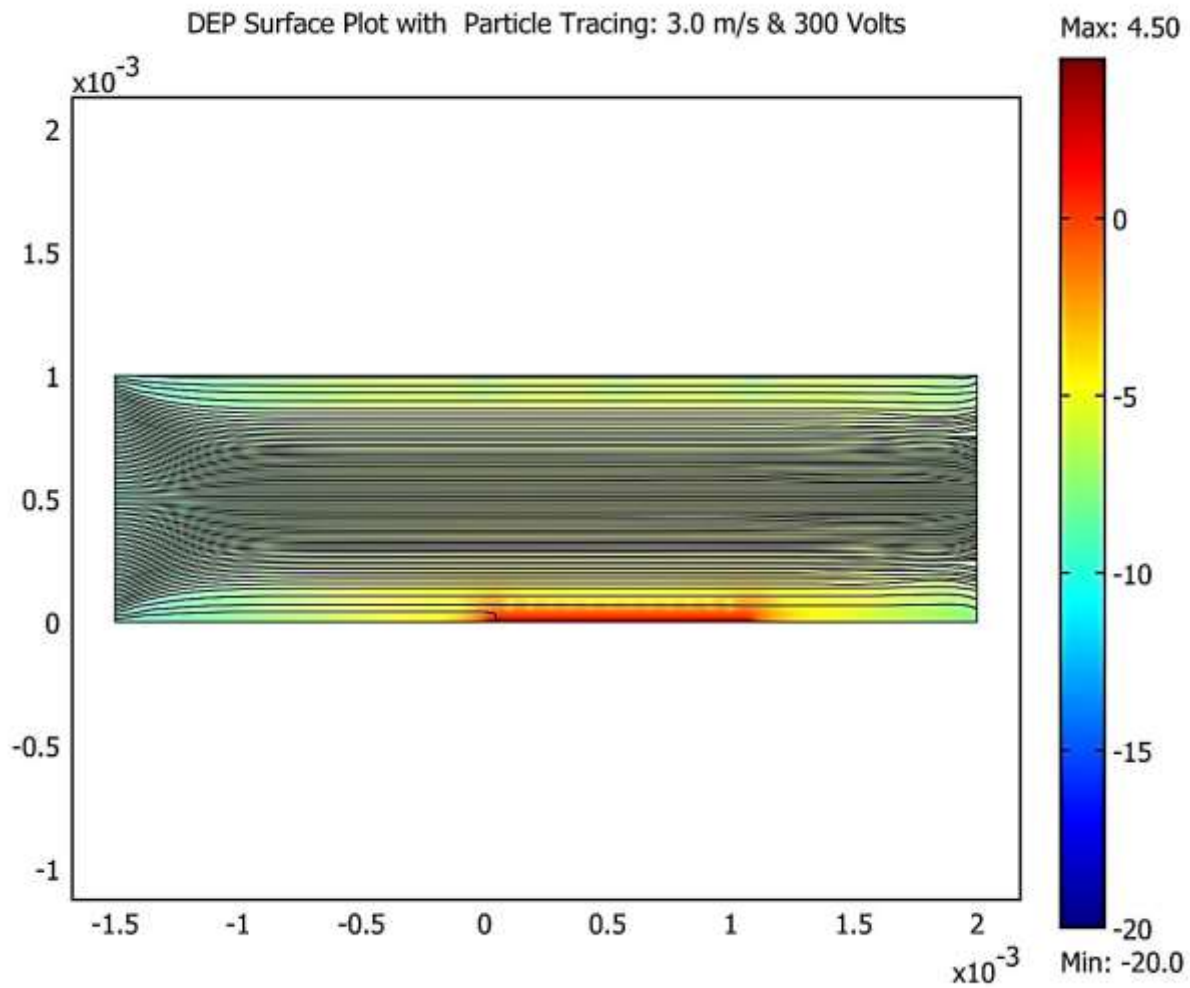


Figure 38 Particle Tracing Plot: air velocity is 3.0m/s and applied voltage value of 300V

C. EXPERIMENTAL

1. EXPERIMENTAL RESULTS

The first set in the experimental sequence is to demonstrate the starting level device cleanliness. Figure 39 is an image of the surface of a clean device before the start of the experiment.

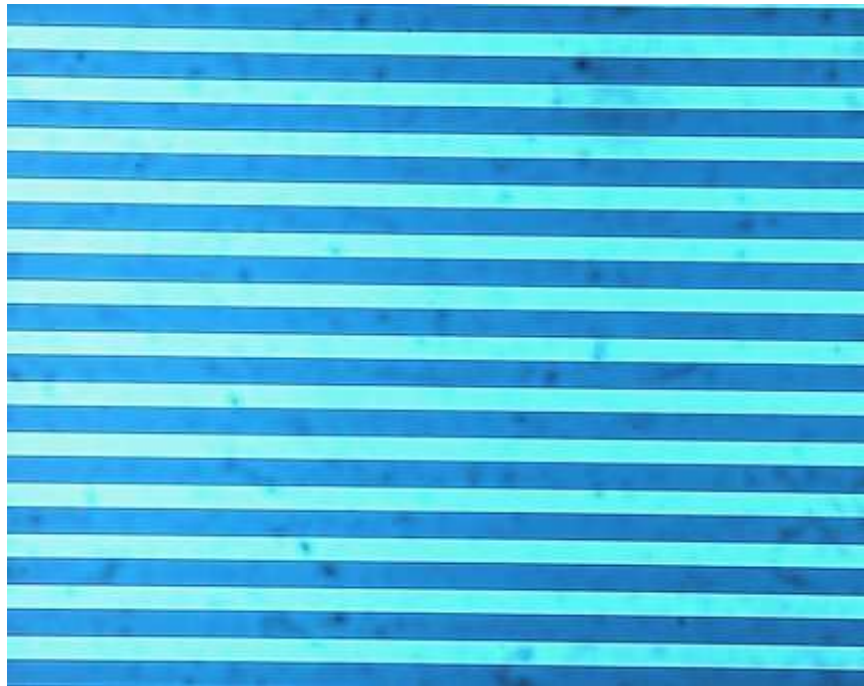
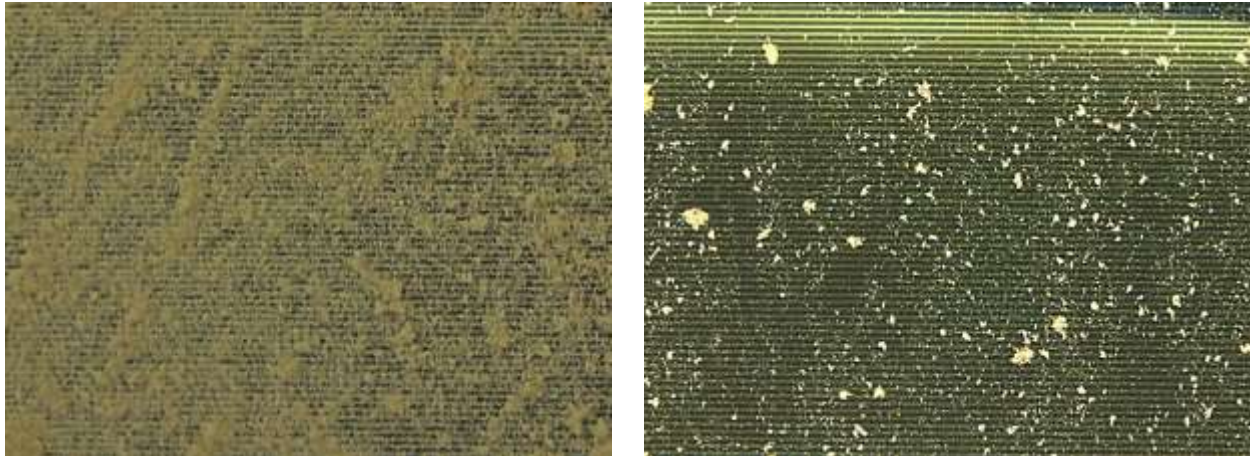


Figure 39: Clean Device before Testing; Taken Under 10X Magnification

Figure 40a shows the results of the powered side and Figure 39b shows the control side of the device used during experiment #1. Figure 40 is shown using 5X magnification. This experiment was conducted with the air velocity measured at 1.5m/s, the voltage was set to 100V at a frequency of 60Hz applied to the powered side of the device. No voltage was supplied to the control side of the device. It is clear from Figure 39a that the device captured significantly more particles compared to Figure 39b. Moreover, the controlled side of the device collected few particles.



A
Powered Test Site
Applied Voltage of 100 V @ 60 Hz

B
Control Test Site

Figure 40 Experiment #1: Under 5X Magnification and 1.5 m/s Air Velocity

Figure 41a shows the results of the powered side and Figure 39b shows the control side of the device used during experiment #2. Figure 41 is shown using 5X magnification. This experiment was conducted with the air velocity measured at 1.5m/s, the voltage was set to 150V at a frequency of 60Hz applied to the powered side of the device. No voltage was supplied to the control side of the device. It is clear from Figure 41a that the device captured significantly more particles compared to Figure 41b. Moreover, the controlled side of the device collected few particles.



A

**Powered Test Site
Applied Voltage of 150 V @ 60 Hz**



B

Control Test Site

Figure 41: Experiment #2: Under 5X Magnification and 1.5 m/s Air Velocity

Figure 42a shows the results of the powered side and Figure 42b shows the control side of the device used during experiment #3. Figure 42 is shown using 5X magnification. This experiment was conducted with the air velocity measured at 1.5m/s, the voltage was set to 200V at a frequency of 60Hz applied to the powered side of the device. No voltage was supplied to the control side of the device. It is clear from Figure 42a that the device captured significantly more particles compared to Figure 42b. Moreover, the controlled side of the device collected few particles.



A

Powered Test Site
Applied Voltage of 200 V @ 60 Hz



B

Control Test Site

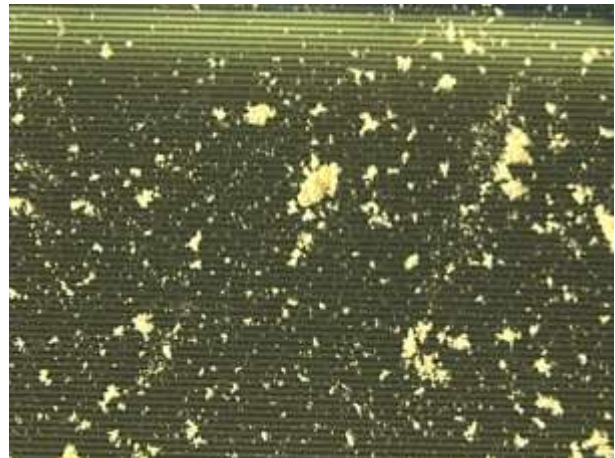
Figure 42:Experiment #3: Under 5X Magnification and 1.5 m/s Air Velocity

Figure 43a shows the results of the powered side and Figure 39b shows the control side of the device used during experiment #4. Figure 43 is shown using 5X magnification. This experiment was conducted with the air velocity measured at 1.5m/s, the voltage was set to 300V at a frequency of 60Hz applied to the powered side of the device. No voltage was supplied to the control side of the device. It is clear from Figure 43a that the device captured significantly more particles compared to Figure 43b. Moreover, the controlled side of the device collected few particles.



A

**Powered Test Site
Applied Voltage of 300 V @ 60 Hz**



B

Control Test Site

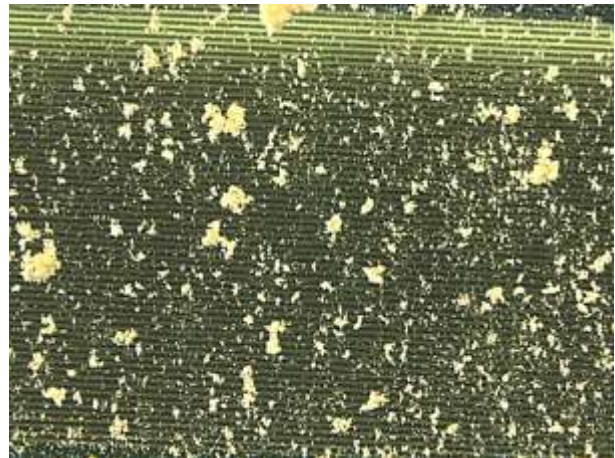
Figure 43: Experiment #4: Under 5X Magnification and 1.5 m/s Air Velocity

Figure 44a shows the results of the powered side and Figure 44b shows the control side of the device used during experiment #5. Figure 40 is shown using 5X magnification. This experiment was conducted with the air velocity measured at 2.3m/s, the voltage was set to 300V at a frequency of 60Hz applied to the powered side of the device. No voltage was supplied to the control side of the device. It is clear from Figure 44a that the device captured significantly more particles compared to Figure 44b. Moreover, the controlled side of the device collected few particles.



A

**Powered Test Site
Applied Voltage of 300 V @ 60 Hz**



B

Control Test Site

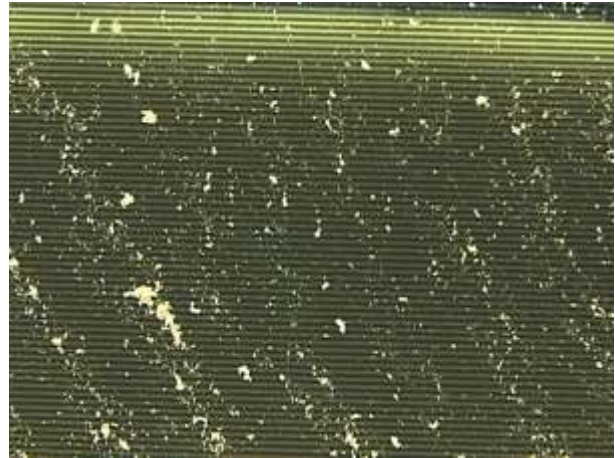
Figure 44: Experiment #5: Under 5X Magnification and 2.3 m/s Air Velocity

Figure 45a shows the results of the powered side and Figure 45b shows the control side of the device used during experiment #6. Figure 45 is shown using 5X magnification. This experiment was conducted with the air velocity measured at 3.0m/s, the voltage was set to 300V at a frequency of 60Hz applied to the powered side of the device. No voltage was supplied to the control side of the device. It is clear from Figure 45a that the device captured significantly more particles compared to Figure 45b. Moreover, the control side of the device collected few particles.



A

**Powered Test Site
Applied Voltage of 300 V @ 60 Hz**



B

Control Test Site

Figure 45: Experiment #6: Under 5X Magnification and 3.0 m/s Air Velocity

Figure 46a shows the results of the powered side and Figure 46b shows the control side of the device used during experiment #7. Figure 46 is shown using 5X magnification. This experiment was conducted with the air velocity measured at $\approx 0\text{m/s}$, the voltage was set to 250V at a frequency of 60Hz applied to the powered side of the device. No voltage was supplied to the control side of the device.

The velocity of the air in this experiment was judged to be approximately $\approx 0\text{m/s}$. This is due to an equipment failure during testing. The test dust was forced into the area using compressed air. The compressed air would allow the dust to “puff” up in a dust cloud around the device. It is clear from Figure 46a that the device captured significantly more particles compared to Figure 46b. Moreover, the control side of the device collected few particles.

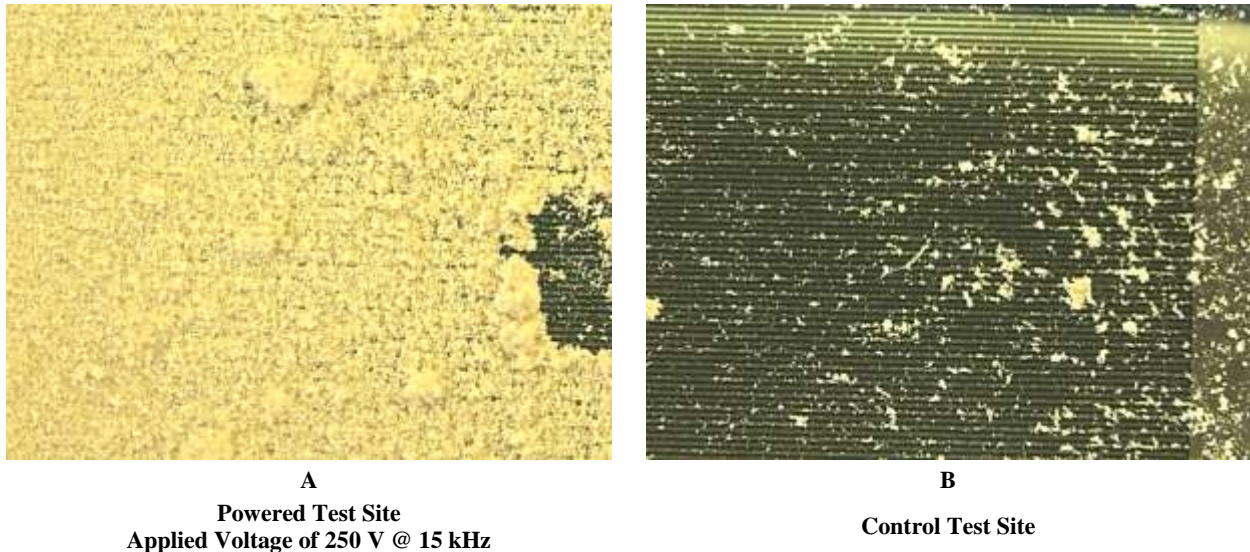
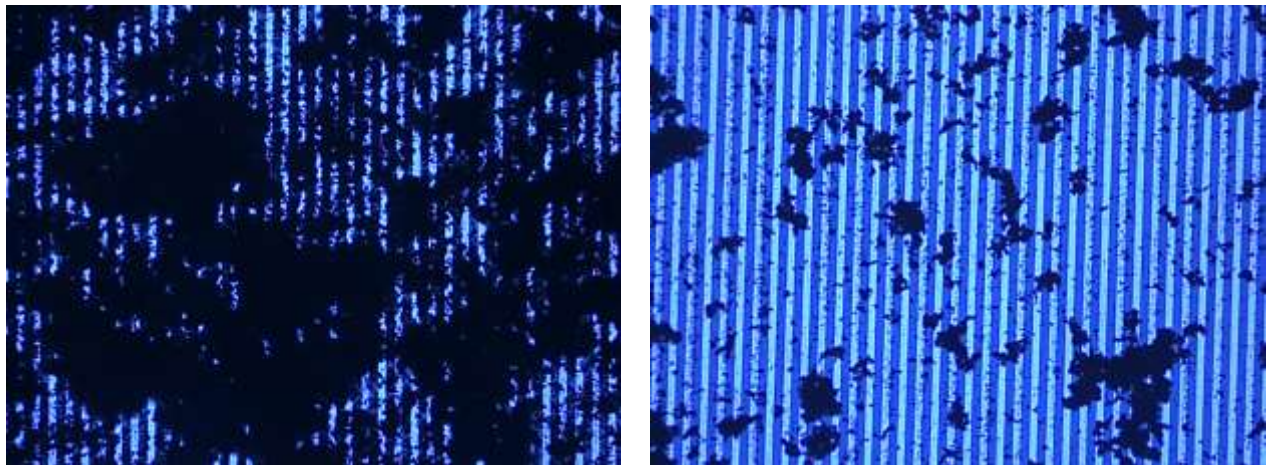


Figure 46: Experiment #7: Under 5X Magnification and $\approx 0\text{ m/s}$ Air Velocity

Figure 47a shows the results of the powered side and Figure 47b shows the control side of the device used during experiment #8. Figure 47 is shown using 5X magnification. This experiment was conducted with the air velocity measured at 2.3m/s, the voltage was set to 250V at a frequency of 15kHz applied to the powered side of the device. No voltage was supplied to the control side of the device. It is clear from Figure 47a that the device captured significantly more particles compared to Figure 47b. Moreover, the control side of the device collected few particles.

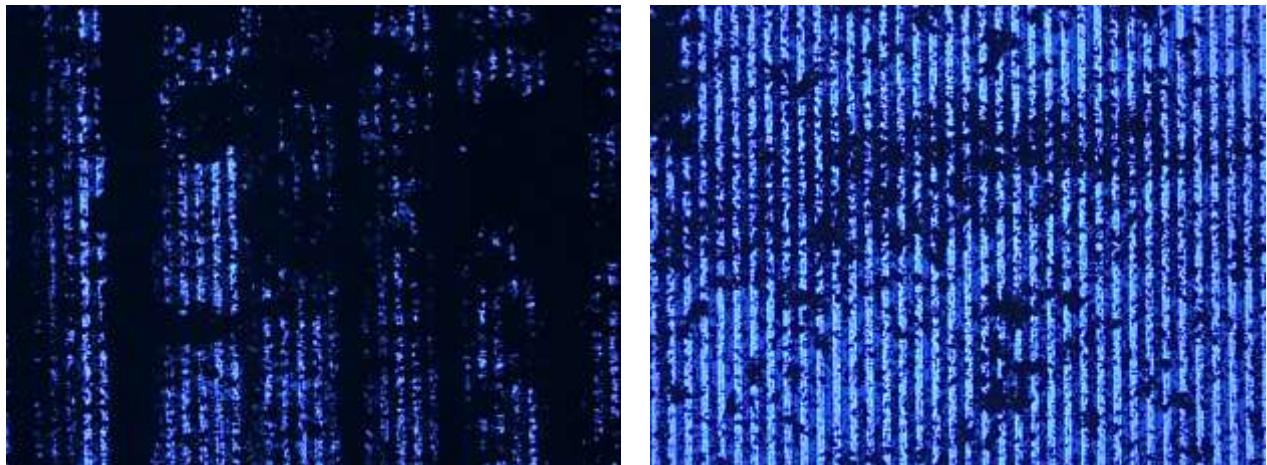


A
Powered Test Site
Applied Voltage of 250V @ 15kHz

B
Control Test Site

Figure 47: Experiment #8: Under 5X Magnification and 2.3m/s Air Velocity

Figure 48a shows the results of the powered side and Figure 48b shows the control side of the device used during experiment #9. Figure 48 is shown using 5X magnification. This experiment was conducted with the air velocity measured at 3.0m/s, the voltage was set to 250V at a frequency of 15kHz applied to the powered side of the device. No voltage was supplied to the control side of the device. It is clear from Figure 48a that the device captured significantly more particles compared to Figure 48b. Moreover, the control side of the device collected few particles.



A
Powered Test Site
Applied Voltage of 250V @ 15kHz

B
Control Test Site

Figure 48: Experiment #9: Under 5X Magnification and 3.0m/s Air Velocity

Figure 49a shows the results of the powered side and Figure 49b shows the control side of the device used during experiment #10. Figure 49 is shown using 5X magnification. This experiment was conducted with the air velocity measured at 1.5m/s, the voltage was set to 250V DC applied to the powered side of the device. No voltage was supplied to the control side of the device. It is clear from Figure 49a that the device captured significantly more particles compared to Figure 49b. Moreover, the control side of the device collected few particles.

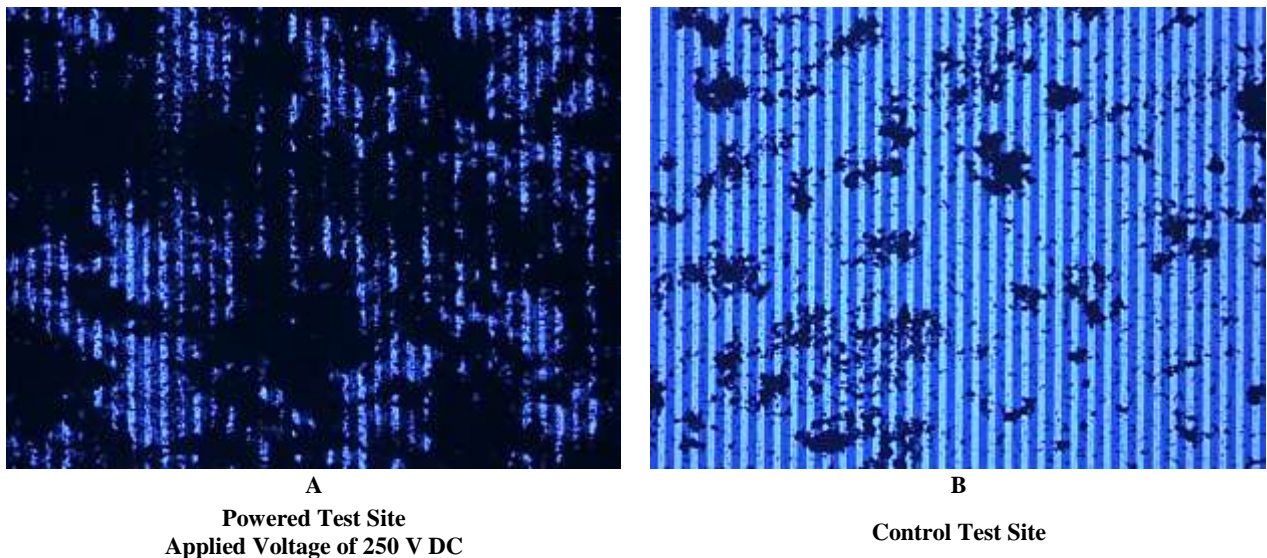


Figure 49: Experiment #10: Under 5X Magnification and 1.5 m/s Air Velocity

2. IMAGE RESULTS

MATLab is a high-level language for matrix manipulation and matrices are the foundation of images making MATLab an perfect tool to compare images. The image averaging programs in MATLab was used to perform using grayscale image processing. A gray-scale image is graph of a function of two variables that takes values between 0 and 256. When the color of the pixel is white the value of the function equals 256. Conversely, when the color is black the value of the function is 0, and for the various shades of gray there will be intermediate

values between 256 and 0. For this processing the average image value for a clean device is 158.

Figure 50 shows the results of the preceding experiment shown in Figure 39-49.

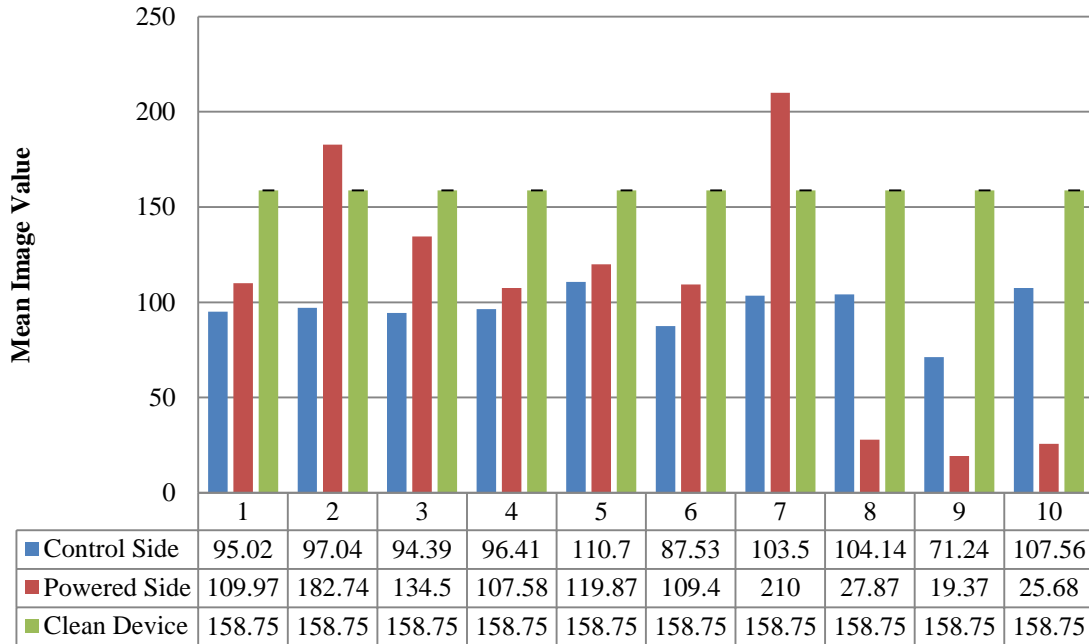


Figure 50 IMAGE RESULTS

3. POWER MEASUREMENTS

Table 13 shows the voltage, amperage, and power that were recorded during the two experiments. The power was calculated using Ohm's law. The electrical measurements were taken with the Agilent 34405A multimeter shown in Figure 13.

Table XIII POWER MEASUREMENTS

Voltage (V)	Amperage (mA)	Power (W)
250 AC	8.64	2.16
250 AC	8.15	2.04

IX. DISCUSSION

The CFD simulations show that a relatively small change in inlet velocity has a great impact on the velocity at the center of the channel. This is an important issue, the velocity profile in the simulations are not true representations of the velocity profile that occurred during the actual experiments. The simulation is limited in scope because of two points; first, the CFD simulation is in 2D. And the last reason, the geometric design of the simulation was simplified to decrease the amount of time need to coverage to a solution.

The greatest of this simplification was the channel geometry. The channel geometry was modeled to be half the actual size of the testing channel used for testing. The second simplifications in the simulations were how the trapping sites were modeled. The simulations do not take in to account the fluidic disturbance that the device would cause. The device is not perfectly smooth or infinitely thin. The actual device during testing will induce fluidic turbulence. This is due to the location of the device in the channel geometry and how it impacts the velocity profile. The leading edges of the device would cause drag and rotation disrupting the fluid flow.

The next area of discussion is the dielectrophoresis simulation. The dielectrophoretic simulation in Figure 27-31 has the same geometric profile as the CFD simulations. The dielectrophoretic plot is a plot of the $\log_{10}(F_{dep})$. The dielectrophoretic simulation shows that the $\log_{10}(F_{dep})$ increases with an increase in input voltage. The area of positive $\log_{10}(F_{dep})$ increase as expected. However, this electrode design is not ideal for the collection of particles. The $\log_{10}(F_{dep})$ force has a limited effective collection area above the electrode array. Moreover, this is not a concern from a proof of concept point of view; there will be a constant

supply of particles in the collection zone of this device to collect. Furthermore, collection efficiency is currently not being tested.

The combination of dielectrophoresis velocity and fluid velocity simulation shown in Figure 32, shows that the combined velocity profile will drive the particles to be collected to the surface of the electrodes. Still, there is a finite area above the electrode where this will occur. Furthermore, any particles that are outside this area will not be collected.

Particle tracing simulations shown in Figures 33-38 demonstrate that under all applied voltages particles are collected. Moreover, when comparing the entire particle tracing simulations together as a group, the collection area above the electrode array increase with an increase in voltage; as expected. A closer inspection of collection, the simulations show that fluid velocity has a significant impact on the collection ability of the device, but this issue can be overcome by increasing the applied voltage, thus increasing the dielectrophoretic force. This voltage effect can be show in comparing the results of Figure 33 and 36. The area of collection in Figure 33 is smaller than Figure 36.

However, the particle tracing simulations use massless particles and are released once during the simulation and the sizes of the particles are 4.0 micron in diameter. The massless particle simulations do not simulate the effects of gravity, particle momentum, and/or particle inertia. Leaving out these important aspects of the simulation undermines the simulations and of the particle movement; there is some value in this type of simulation.

The simulation shows that a massless particle traveling from the inlet of the channel across the electrode array under a dielectrophoretic influence will collect at the stated voltage and fluid velocities.

The experimental section of the results shows that dielectrophoretic precipitation will collect particles from a gas stream as shown in Figures 40 - 49. Each experiment collected particles under varying degrees of environmental conditions, and results. The results of experiment 1 - 6 and 8 - 10 have similar results, each collected particles. Nevertheless, you can see the electrodes under the cake of particles. This is an indication that the cake is thin with few particles collected. Conversely, there are areas in the cake that are thicker, suggesting that the device is capable of developing a thicker cake with longer testing time. Without this force there is no enhanced particle removal from the air stream. These results support the capability of the dielectrophoretic force to remove particles from the air stream.

Experiment 7 occurred because of a fan failure. The source of air movement occurred from a quick burst of compressed air from the air compressor. This burst would push a cloud of dust up in the channel and the cloud would float around the device. This would greatly reduce the effect of the fluid movement and test the effectiveness of the dielectrophoretic force. The outcome of this test is not surprising; the device collected a noticeable amount of particles. This is clearly seen in Figure 46, you are not able to see the electrodes under the cake of particles. Combining the results of simulations and the experiments, the results are suggesting that the collection efficiency of the device is directly affected by the input voltage and the fluid velocity.

One way to measure the effectiveness of each experimental test was to perform an image averaging analysis using MATLAB. The results of this analysis show that there is a relationship between the applied voltage and fluid velocity. Moreover, experiments 2, 3, and 7 have the highest mean values of the powered devices. These experiments also have the highest difference in applied voltage to fluid velocity.

This can also be seen in experiment 9. However, the color contrast and lighting of images is different in experiments 8, 9, and 10. These images are darker than the rest of the experiments causing an inverse relationship compared to the preceding experiments. Still, Experiment 7 with its large voltage to velocity difference shows to have collected the greasiest amount of particles; as expected.

The power to collect those particles is shown in Table 13. Table 13 shows that the devices consumed about 2 watts of power to collect the particle using 250V at 15 kHz. This is a small amount of power. Each testing site has an area of 0.25 mm^2 and the measured current was 8.15 mA . This provides a current density of $0.031 \frac{\text{mA}}{\text{mm}^2}$. Conversely, the typical electrostatic precipitator has a current density of $1.1E^6 \frac{\text{mA}}{\text{mm}^2}$ [18]. There is a significant difference between these devices and these devices are not comparable in designs or function. For a true comparison of power usage a large scale DEP precipitator would have to be designed and constructed to compare the two.

X. CONCLUSIONS

The result of this work show that the application of dielectrophoresis for the removal of micron sized particles from an air stream is appropriate. There is clear evidence that the particles are captured and removed from the air stream under all applied voltages and air velocities with an interdigitated electrode device.

These results demonstrate that designing a full scale dielectrophoretic precipitator has merit. However, the current interdigitated electrode design does not. The current design is not a functional filter nor could it be. Nevertheless, it did prove that a dielectrophoretic precipitator is possible. With that in mind, a properly designed dielectrophoretic precipitator would have to have a high gradient electric field and moderate to high voltages.

There are two design directions that have the most potential. First, an array of plate and wire designed into a dielectrophoretic precipitator would be ideal design for large gas loads with low pressure loss. The wire could be a carbon nanotube fiber. For example Rice University has developed a carbon nanotube fiber that can be hundreds of meters in length, around 80 μ m in diameter, and has comparable electrical conductivity to copper[19].

This carbon nanotube fiber could also be woven into a fabric media to be charged. This design would allow for the higher efficiency with lower pressure loss across the fabric media filter. These discussed designs could then be integrated with current industrial equipment. For example a bag house filter could be replaced with a DEP media filter to decrease the pressure loss and provide higher filtration efficiency, the electrostatic precipitators systems could be retrofitted to remove highly resistive particle. This would change how we clean the air!

XI. RECOMMENDATIONS

This project has shown that dielectrophoresis is capable of collecting air born particles from a moving gas stream. Dielectrophoresis was first discovered in the 1960's and the investigation of how to implement this force is ongoing. However, with the correct application dielectrophoresis can dynamically change the way we filter and separate particles from a moving fluidic process. This technology has the potential to have a high impact on the ability to collect particles with high collection and energy efficiency, leading to a lower total cost of filtration than what is currently available in the market place today.

I recommend that this project be fully capitalized and supported for future development.

The focus of this effort shall be to determine the following:

1. The physics of air born particles under the influence of dielectrophoresis focusing on an analytical and numerical modeling of the particle behavior
2. The collection efficiency of a dielectrophoresis filter using ASHRAE 52.2 testing procedures.
3. The ideal applied voltage/fluid velocity ratio for optimal particle collection
4. The ideal electrode geometry and/or orientation for particle collection
5. Economical electrode and air handling manufacturing process

This development focus is necessary to determine the total economic and environmental impact that a dielectrophoretic filter can have.

REFERENCES

- [1] A. Desai, S.-W. Lee, and Y.-C. Tai, "A MEMS electrostatic particle transportation system," *Sensors and Actuators A: Physical*, vol. 73, pp. 37-44, 1999.
- [2] S. Calvert and H. M. Englund, *Handbook of air pollution technology*. New York: Wiley, 1984.
- [3] L. Theodore and A. J. Buonicore, *Air pollution control equipment*. Boca Raton, Fla.: CRC Press, 1988.
- [4] C. D. Cooper and F. C. Alley, *Air pollution control : a design approach*. Boston: PWS Engineering, 1986.
- [5] N. A. Janssen, G. Hoek, M. Simic-Lawson, P. Fischer, L. van Bree, H. ten Brink, M. Keuken, R. W. Atkinson, H. R. Anderson, B. Brunekreef, and F. R. Cassee, "Black carbon as an additional indicator of the adverse health effects of airborne particles compared with PM10 and PM2.5," *Environmental health perspectives*, vol. 119, pp. 1691-9, 2011.
- [6] H. Morgan and N. G. Green. (2003). *AC electrokinetics colloids and nanoparticles*. Available: <http://search.ebscohost.com/login.aspx?direct=true&scope=site&db=nlebk&db=nlabk&AN=101789>
- [7] (2013, 05/01/2013). *About AAF International*.
- [8] L. Lawrence Livermore, L. Lawrence Livermore National, S. United States. Dept. of Energy. Office of, and I. Technical. (1976). *Air filtration enhancement using electronic techniques*. Available: <http://www.osti.gov/servlets/purl/7269025-ftRfw2/>
- [9] L. Lawrence Livermore, L. Lawrence Livermore National, S. United States. Dept. of Energy. Office of, and I. Technical. (1978). *Enhanced filtration program at LLL. A progress report*. Available: <http://www.osti.gov/servlets/purl/6689914-biA9YV/>
- [10] A. D. Moore, *Electrostatics and its applications*. New York: Wiley, 1973.
- [11] T. B. Jones, "Basic theory of dielectrophoresis and electrorotation," *IEEE engineering in medicine and biology magazine : the quarterly magazine of the Engineering in Medicine & Biology Society*, vol. 22, 2003.
- [12] H. Li and R. Bashir, "Dielectrophoretic separation and manipulation of live and heat-treated cells of *Listeria* on microfabricated devices with interdigitated electrodes," *SENSORS AND ACTUATORS B*, vol. 86, pp. 215-221, 2002.
- [13] M. K. Mazumder, R. Sharma, A. S. Biris, J. Zhang, C. Calle, and M. Zahn, "Self-Cleaning Transparent Dust Shields for Protecting Solar Panels and Other Devices," *Particulate Science and Technology*, vol. 25, pp. 5-20, 2007/01/30 2007.

- [14] N. G. Green, A. Ramos, and H. Morgan, "Numerical solution of the dielectrophoretic and travelling wave forces for interdigitated electrode arrays using the finite element method," *Journal of Electrostatics*, vol. 56, 2002.
- [15] B. R. Munson, D. F. Young, and T. H. Okiishi, *Fundamentals of fluid mechanics*. New York: Wiley, 1998.
- [16] S. D. Pawar, P. Murugavel, and D. M. Lal, "Effect of relative humidity and sea level pressure on electrical conductivity of air over Indian Ocean," *J. Geophys. Res. Journal of Geophysical Research*, vol. 114, 2009.
- [17] G. V. Samsonov, *The Oxide handbook*. New York: IFI/Plenum, 1973.
- [18] T. Neundorfer. (2013). *The Neundorfer* Available: http://www.neundorfer.com/knowledge_base/electrostatic_precipitators.aspx
- [19] N. Behabtu, C. C. Young, D. E. Tsentalovich, O. Kleinerman, X. Wang, A. W. Ma, E. A. Bengio, R. F. ter Waarbeek, J. J. de Jong, R. E. Hoogerwerf, S. B. Fairchild, J. B. Ferguson, B. Maruyama, J. Kono, Y. Talmon, Y. Cohen, M. J. Otto, and M. Pasquali, "Strong, light, multifunctional fibers of carbon nanotubes with ultrahigh conductivity," *Science (New York, N.Y.)*, vol. 339, pp. 182-6, 2013.
- [20] C. P. S. University. (07). *Electrostatic Precipitator*. Available: <http://ceenve3.civeng.calpoly.edu/cota/ENVE411-ESP.html>
- [21] S. Environment. (2010, 7). *Water pollution and its solution*. Available: <http://saferenvironment.wordpress.com/posts/page/2/>
- [22] A. Systems. (2012, 07). *airflow stream around the fiber and through the filter*. Available: <https://airfilterstore.com/blueair/technology.htm>

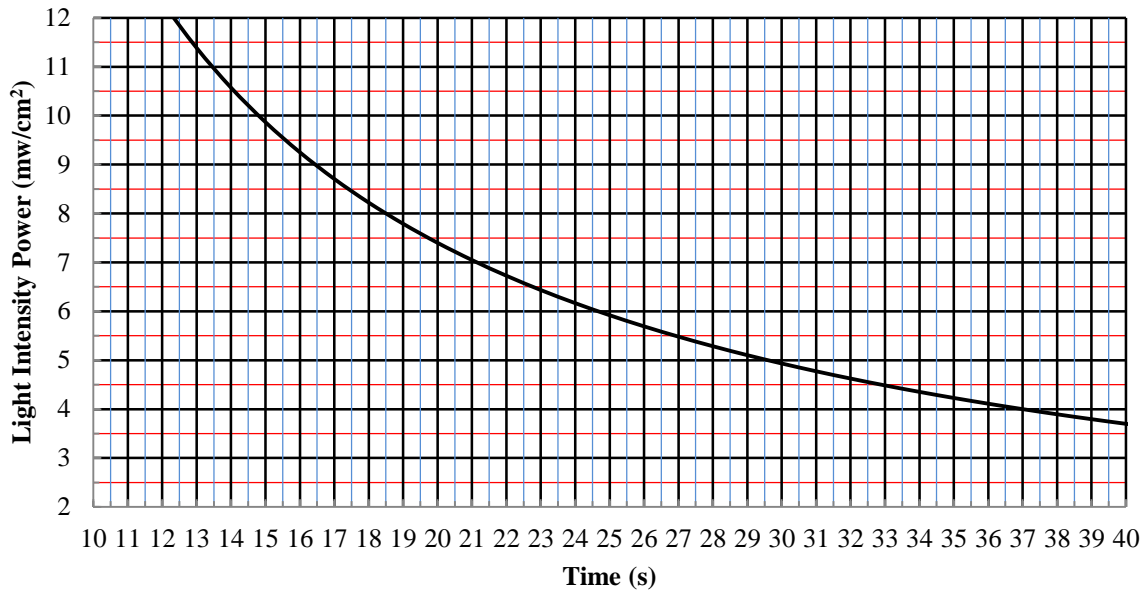
APPENDIX A: LIFTOFF RECIPE

- Tested with a total metal deposition of ~ 200 nm
- Be consistent with your timing (soft bake, toluene soak, & PEB)
- Set one of the lithography hotplates to 90°C
- Program the spinner with the following parameters:

Step	1	2	3
	Spread	Spin	Stop
Spin Speed (rpm)	500	4000	0
Ramp (rpm/s)	1000	1000	1000
Time hold speed (s)	2.0/5.0	10	0

- Spin HMDS on the substrate. HMDS is a primer used for adhesion.
- Puddle HMDS on entire wafer and wait 5-10 seconds before spinning.
- Spin S1827 (photoresist desired thickness ~ 2.7 μm)
- On circular wafers, cover 50% starting at the center working towards the edge. On non-circular or irregularly shaped samples, follow the contour of the sample covering 75% of the area. Spin wafer at the same settings as the HMDS application
- Place your sample on the 90 °C hot plate for 75 s
- Allow sample to rehydrate in air for ~ 1-minute prior to exposure.
- Expose substrate to deliver an energy dosage of ~280 mJ/cm^2
 - Using the graph below to determine the correct time for your current light Intensity of the mask aligner.

- Pour Toluene in a glass dish (enough to submerge your substrate completely)



- Glass dish should be clean, dry and free of any contaminants.
- Submerge exposed substrate in Toluene for 1 min and agitate
- Dry with N₂ gun promptly (no water, no IPA, just N₂!)
- Place the substrate on 90 °C hotplate for 15s
- Develop substrate in MF 319 and agitate the substrate.
- The development of the photoresist with this method takes a little longer. Your developed features will undergo several color changes. You want to look for when the color stops changing. Specifically, for oxidized wafer, you want to look for purple developed features. For glass substrate, you want to make sure you cannot see a rainbow in your developed features.
- I have been using fresh developer and have developed the substrate for 70 seconds with very good results.
- Rinse with water for 30-60 seconds and dry with N₂ gun.
- Optical inspection.
- Check for residual resist in exposed regions. If resist remains in exposed areas or if the pattern is too large or small, strip the resist off the sample and start over. Adjust the exposure times until the measured openings in the photoresist match the patterns on the mask.
- You want to see a dark outline on your features.
- Deposition of metal: KJL PVD 75 Sputtering System

	AL
DC Power	250 W
Pressure	5mTorr
Time (min)	2.5
Measured Thickness	~150nm

- Fill a beaker with acetone and place sample in the beaker (must be completely submerged)
- Set sonicator power at 4 (located on top of bench control)
- Place beaker in sonicator bath and sonicate for 1 hr.
- Prepare a new beaker with clean acetone. Remove your substrate from the old acetone bath and place in the new acetone bath while rinsing it with acetone using the squeeze bottle (avoiding it from drying and removing any metal residue from the surface)
- Place to sonicate for another 1 more hour
- Rinse with acetone, methanol, IPA, water and dry
- Visually inspect if liftoff was successful!

APPENDIX B: MATLAB COMPUTER SIMULATION CODE

```

% This is a script to model and plot the Clausius-Mossotti Factor
% script contains expressions for 0 shell particles with different
% properties defined at the start
eo = 8.854e-12;                                %permittivity (Free)
em = 1.00059*eo;      sm = 0.783e-14;         %medium properties (general)
legendlocation = 'EastOutside';               % Location if the Legend
linereal = 2;                                  % LineWidth of the real Line
lineimag = 1;                                  % LineWith of hte imag Line
xaxis = 10^12;                                 % X Axis
%
%permittivity      conductivity
%
ep1 = 3.8*eo;      sp1 = 1e-17;      %particle (0 shell Sio2 particles )Good
ep2 = 9.5*eo;      sp2 = 1e-13;      %particle (0 shell Al2O3 particles )Good
ep3 = 10*eo;       sp3 = 1e-4;       %particle (0 shell Fe2O3 particles )
ep4 = 20*eo;       sp4 = 0.5;        %particle (0 shell Na2O particles )
ep5 = 3*eo;        sp5 = .000024;    %particle (0 shell CaO particles )Good
ep6 = 9.6*eo;      sp6 = 1e8;        %particle (0 shell MgO particles )Good
ep7 = 86*eo;       sp7 = 1e-16;     %particle (0 shell TiO2 particles )Good
ep8 = 60*eo;       sp8 = 0.9;       %particle (0 shell K2O particles )
%
% The frequency
%
f = logspace(1,12,100);      omega = 2*pi*f;      x = 1;
% The calculation - zero shells
eph1 = ep1 - (1i.*sp1./omega);  emh1 = em - (1i.*sm./omega);
fCM1 = (eph1-emh1)./(eph1+(2*emh1));      %Clausius-Mossotti factor
%
eph2 = ep2 - (1i.*sp2./omega);  emh2 = em - (1i.*sm./omega);
fCM2 = (eph2-emh2)./(eph2+(2*emh2));      %Clausius-Mossotti factor
%
eph3 = ep3 - (1i.*sp3./omega);  emh3 = em - (1i.*sm./omega);
fCM3 = (eph3-emh3)./(eph3+(2*emh3));      %Clausius-Mossotti factor
%
eph4 = ep4 - (1i.*sp4./omega);  emh4 = em - (1i.*sm./omega);
fCM4 = (eph4-emh4)./(eph4+(2*emh4));      %Clausius-Mossotti factor
%
eph5 = ep5 - (1i.*sp5./omega);  emh5 = em - (1i.*sm./omega);
fCM5 = (eph5-emh5)./(eph5+(2*emh5));      %Clausius-Mossotti factor
%
eph6 = ep6 - (1i.*sp6./omega);  emh6 = em - (1i.*sm./omega);
fCM6 = (eph6-emh6)./(eph6+(2*emh6));      %Clausius-Mossotti factor
%
eph7 = ep7 - (1i.*sp7./omega);  emh7 = em - (1i.*sm./omega);
fCM7 = (eph7-emh7)./(eph7+(2*emh7));      %Clausius-Mossotti factor
%
eph8 = ep8 - (1i.*sp8./omega);  emh8 = em - (1i.*sm./omega);
fCM8 = (eph8-emh8)./(eph8+(2*emh8));      %Clausius-Mossotti factor
%
if (x) == 1;
    plotting
    the real parts are plotted as solid lines, the imaginary
    parts as dotted lines
    semilogx(f,real(fCM1),'r','LineWidth',linereal);      hold on
    semilogx(f,imag(fCM1),'r','LineWidth',lineimag);      hold on

```

```

%
semilogx(f,real(fCM2),'g','LineWidth',linereal);      hold on
semilogx(f,imag(fCM2),'g','LineWidth',lineimag);      hold on
%
semilogx(f,real(fCM3),'c','LineWidth',linereal);      hold on
semilogx(f,imag(fCM3),':c','LineWidth',lineimag);    hold on
%
semilogx(f,real(fCM4),'m','LineWidth',linereal);      hold on
semilogx(f,imag(fCM4),':m','LineWidth',lineimag);    hold on
%
semilogx(f,real(fCM5),'k','LineWidth',linereal);      hold on
semilogx(f,imag(fCM5),':k','LineWidth',lineimag);    hold on
%
semilogx(f,real(fCM6),'y','LineWidth',linereal);      hold on
semilogx(f,imag(fCM6),':y','LineWidth',lineimag);    hold on
%
semilogx(f,real(fCM7),'b','LineWidth',linereal);      hold on
semilogx(f,imag(fCM7),':b','LineWidth',lineimag);    hold on
%
semilogx(f,real(fCM8),'cx','LineWidth',linereal);     hold on
semilogx(f,imag(fCM8),':x','LineWidth',lineimag);    hold on
%
figure(1);
xlabel('Frequency (Hz)');
ylabel('Negative DEP < 0 > Positive DEP');
legend('SiO2','Al2O3','CaO','MgO','TiO2','Location','EastOutside');
axis([0 xaxis -1 1.5]);      grid
%
x = x + 1;
end
%
figure(2);
semilogx(f,real(fCM1),'r','LineWidth',linereal);      hold on
semilogx(f,imag(fCM1),':r','LineWidth',lineimag);    hold on
xlabel('Frequency (Hz)');
ylabel('Negative DEP < 0 > Positive DEP');
legend('SiO2 particles','Location',legendlocation);
axis([0 xaxis -1 1.5]);      grid
%
figure(3)
semilogx(f,real(fCM2),'r','LineWidth',linereal);      hold on
semilogx(f,imag(fCM2),':r','LineWidth',lineimag);    hold on
xlabel('Frequency (Hz)');
ylabel('Negative DEP < 0 > Positive DEP');
legend('Al2O3 particles','Location',legendlocation);
axis([0 xaxis -1 1.5]);      grid
%
figure(4)
semilogx(f,real(fCM3),'r','LineWidth',linereal);      hold on
semilogx(f,imag(fCM3),':r','LineWidth',lineimag);    hold on
xlabel('Frequency (Hz)');
ylabel('Negative DEP < 0 > Positive DEP');
legend('FE2O3 particles','Location',legendlocation);
axis([0 xaxis -1 1.5]);      grid
%
figure(5)
semilogx(f,real(fCM4),'r','LineWidth',linereal);      hold on

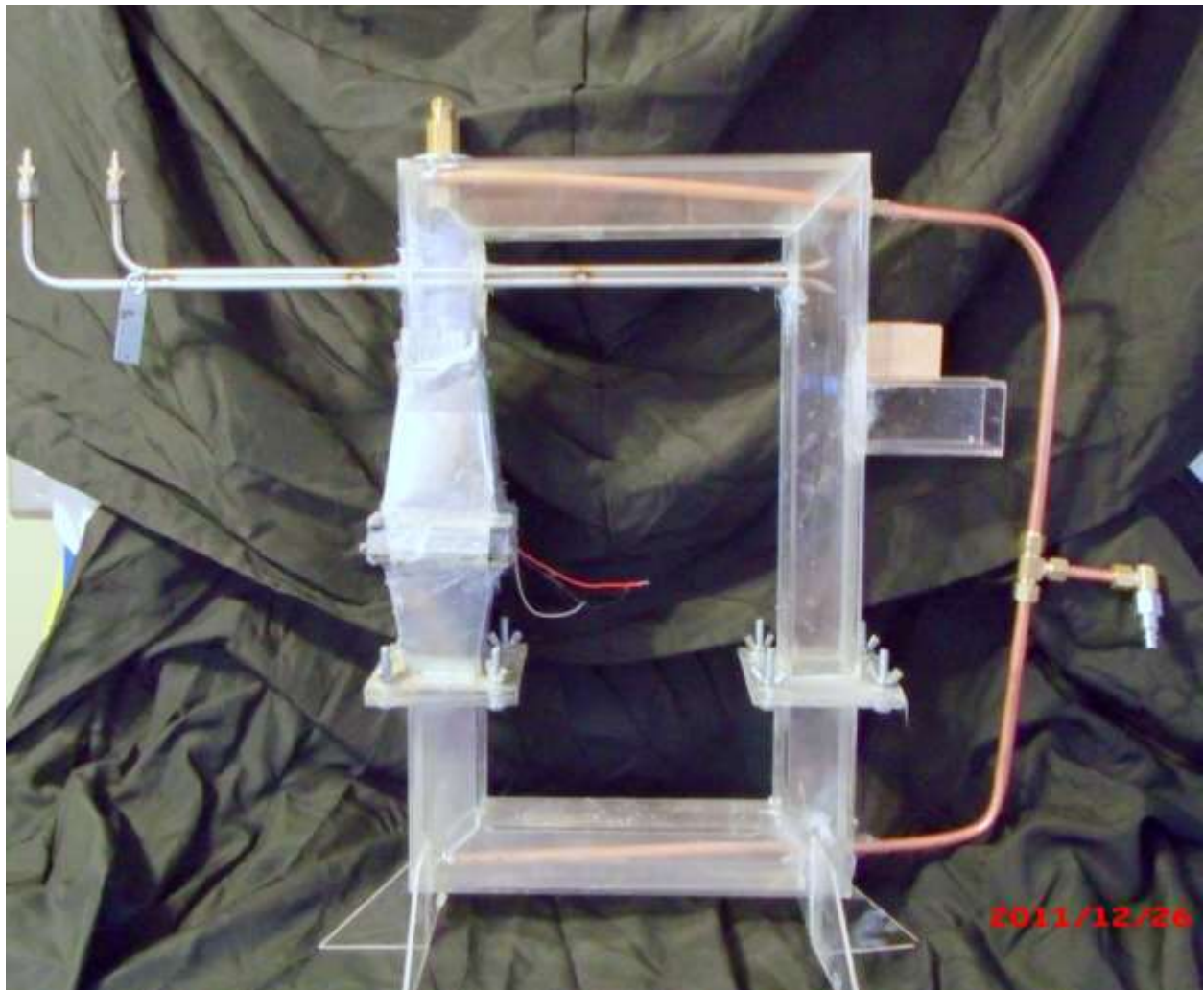
```

```

semilogx(f, imag(fCM4), ':r', 'LineWidth', lineimag); hold on
xlabel('Frequency (Hz)');
ylabel('Negative DEP < 0 > Positive DEP');
legend('Na2O particles', 'Location', legendlocation);
axis([0 xaxis -1 1.5]); grid
%
figure(6)
semilogx(f, real(fCM5), 'r', 'LineWidth', linereal); hold on
semilogx(f, imag(fCM5), ':r', 'LineWidth', lineimag); hold on
xlabel('Frequency (Hz)');
ylabel('Negative DEP < 0 > Positive DEP');
legend('CaO particles', 'Location', legendlocation);
axis([0 xaxis -1 1.5]); grid
%
figure(7)
semilogx(f, real(fCM6), 'r', 'LineWidth', linereal); hold on
semilogx(f, imag(fCM6), ':r', 'LineWidth', lineimag); hold on
xlabel('Frequency (Hz)');
ylabel('Negative DEP < 0 > Positive DEP');
legend('MgO particles', 'Location', legendlocation);
axis([0 xaxis -1 1.5]); grid
%
figure(8)
semilogx(f, real(fCM7), 'r', 'LineWidth', linereal); hold on
semilogx(f, imag(fCM7), ':r', 'LineWidth', lineimag); hold on
xlabel('Frequency (Hz)');
ylabel('Negative DEP < 0 > Positive DEP');
legend('TiO2 particles', 'Location', legendlocation);
axis([0 xaxis -1 1.5]); grid
%
figure(9)
semilogx(f, real(fCM8), 'r', 'LineWidth', linereal); hold on
semilogx(f, imag(fCM8), ':r', 'LineWidth', lineimag); hold on
xlabel('Frequency (Hz)');
ylabel('Negative DEP < 0 > Positive DEP');
legend('K2O particles', 'Location', legendlocation);
axis([0 xaxis -1 1.5]); grid

```

APPENDIX C: TEST APPARATUS DESIGN AND CONSTRUCTION



APPENDIX D: MANUFACTURER DATA SHEETS



PRODUCT LIST PP7C4
ISO 12103-1 ARIZONA TEST DUST CONTAMINANTS
A1 ULTRAFINE & A3 MEDIUM GRADES

TYPICAL CHEMICAL ANALYSIS

Chemical	% Of Weight	Chemical	% Of Weight
SiO ₂	68 - 76	CaO	2.0 - 5.0
Al ₂ O ₃	10 - 15	MgO	1.0 - 2.0
Fe ₂ O ₃	2 - 5	TiO ₂	0.5 - 1.0
Na ₂ O	2 - 4	K ₂ O	2.0 - 5.0

*Loss on Ignition 2 - 5%

ISO TEST DUST PARTICLE SIZE DISTRIBUTIONS (Volume % Less Than)

SIZE (µm)	ISO 12103-1, A1 Ultrafine	ISO 12103-1, A3 Medium
1	1.0 - 3.0	1.0 - 3.0
2	9.0 - 13.0	4.0 - 5.5
3	21.0 - 27.0	7.5 - 9.5
4	36.0 - 44.0	10.5 - 13.0
5	56.0 - 64.0	15.0 - 19.0
7	83.0 - 88.0	28.0 - 33.0
10	97.0 - 100	40.0 - 45.0
20	100	65.0 - 69.0
40		84.0 - 88.0
80		99.0 - 100
120		100

ISO Ultrafine	ISO Medium
Cost (per 500 grams): \$42.00	Cost (per jar): \$60.00
Packaging: Customized to quantity ordered	Packaging: 4-Liter jar, 3.5 kg per jar

Notes:

1. Orders less than \$200.00 are subject to a \$20.00 handling fee
2. Prices are in U.S. Dollars
3. Each batch is shipped with particle size distribution, analyzed with a Coulter Multisizer IIe
4. F.O.B. - Shipping Point
5. Prices are subject to change without notice.
6. PTI has a no return policy on all products.

ISO 9001:2008 Registered

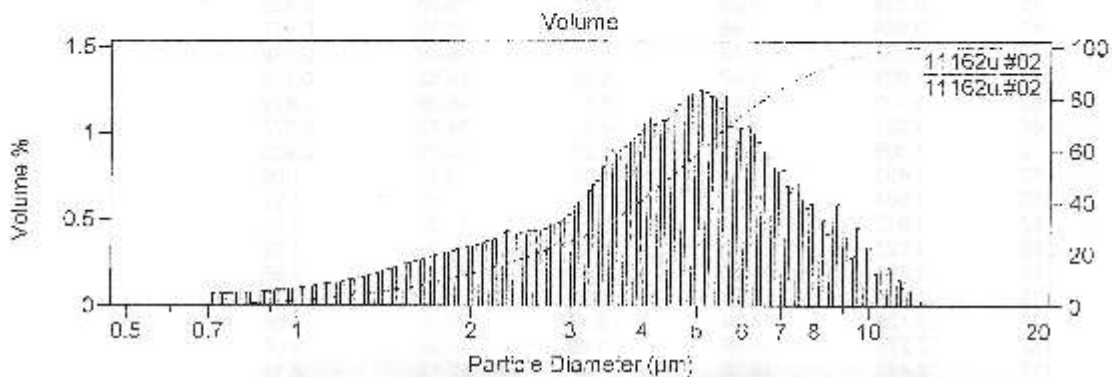


14331 Ewing Ave S • Burnsville, Minnesota 55306 • Phone: 952-894-8737 • Fax: 952-894-0734
 Web: www.powdertechologyinc.com

October 2008



Filename: 11162u.#02 Sample Number: 267
 Group ID: 11162u.
 Sample ID: ISO 12103-1: A1 ULTRAFINE TEST DUST, NIST TRACEABLE
 Comment: DRUM 1
 Operator: MJP
 Acquired: 10:38 10 Nov 2011
 Edited size data



Volume Statistics (Geometric) 11162u.#02

Calculations from 0.489 µm to 17.01 µm

Volume: $303.8e3 \mu\text{m}^3$
 Mean: 4.677 µm S.D.: 3.07 µm
 Median: 4.478 µm
 Mode: 6.358 µm

11162u.#02

Particle Diameter µm	Volume % <
1	1.98
2	12.47
3	24.87
4	41.36
5	59.48
7	84.64
10	97.82

11182u.#02

Channel Number	Particle Diameter µm	Cum < Volume %	Diff Number %	Cum < Number %	Diff Volume %
22	0.654	0	0	0	0
27	0.701	0	8.36	0	0.278
32	0.752	0.278	9.26	8.36	0.372
37	0.808	0.650	7.69	17.62	0.381
42	0.864	1.03	7.03	25.32	0.427
47	0.925	1.48	6.27	32.32	0.477
52	0.992	1.93	5.83	38.69	0.538
57	1.053	2.47	6.37	44.52	0.610
62	1.120	3.08	4.85	49.89	0.679
67	1.221	3.76	4.51	54.74	0.777
72	1.309	4.54	4.26	59.25	0.803
77	1.403	5.44	4.07	63.51	1.03
82	1.504	6.50	3.80	67.57	1.22
87	1.612	7.73	3.47	71.37	1.37
82	1.727	9.10	3.12	74.91	1.52
97	1.851	10.62	2.74	77.96	1.65
102	1.984	12.27	2.40	80.71	1.77
107	2.128	14.04	2.14	83.10	1.95
112	2.279	15.98	1.88	85.24	2.09
117	2.443	18.08	1.65	87.12	2.18
122	2.618	20.23	1.32	88.68	2.26
127	2.806	22.48	1.13	90.01	2.48
132	3.007	24.86	1.15	91.20	2.97
137	3.223	27.93	1.15	92.35	3.65
142	3.451	31.58	1.14	93.80	4.43
147	3.702	36.01	0.893	94.54	4.77
152	3.968	40.78	0.890	95.83	5.25
157	4.253	46.03	0.750	96.52	5.46
162	4.558	51.48	0.861	97.27	5.92
167	4.885	57.41	0.558	97.91	6.14
172	5.236	63.55	0.439	98.49	5.95
177	5.612	69.80	0.314	98.93	5.22
182	6.015	74.72	0.242	99.25	4.97
187	6.446	79.89	0.168	99.49	4.73
192	6.908	83.82	0.115	99.66	3.58
197	7.405	87.50	0.091	99.77	3.06
202	7.936	90.59	0.053	99.85	2.47
207	8.508	93.06	0.042	99.91	2.46
212	9.116	95.52	0.024	99.95	1.74
217	9.771	97.26	0.014	99.97	1.23
222	10.47	98.49	0.008	99.99	0.914
227	11.22	99.40	0.004	100.00	0.502
232	12.03	99.90	0.001	100.00	0.097
237	12.89	100.00	0	100.00	0
242	13.82	100.00	0	100.00	0

APPENDIX E: IMAGE AVERAGING PROGRAM

```
clear all % clear all variables

%% 1. Acquire image file

[filename1, pathname1] = uigetfile('.tif','Choose file 1');

%% 2. Convert to grayscale

a=imread(filename1);

a=rgb2gray(a);

a=double(a);

[max(a(:)),min(a(:)),mean(a(:)),std(a(:))]
```


CURRICULUM VITAE:

Joseph D. Duff

1210 Lincoln Ave. • Louisville Kentucky 40208 • Phone 502 4325110

E-mail joseph.duff@gmail.com

EDUCATION

05/2010 – Current University of Louisville Louisville, Kentucky
Master of Engineering in Mechanical Engineering

01/2008 – 05/2010 University of Louisville Louisville, Kentucky
Bachelor of Science in Mechanical Engineering

Memberships American Society of Mechanical Engineers (ASME)
The American Society of Heating, Refrigerating and Air-Conditioning
Engineers (ASHRAE)

MILITARY SERVICE

09/1995 – 10/1997 United States Marine Corps Camp Pendleton, California
Automotive Intermediate Mechanic

Honorable discharge in October 1997.

EMPLOYMENT

08/2009 – 5/2010 University of Louisville Louisville, Kentucky
Research Assistant

Performed experimental research in the area of fabrication and design of nano-mechanical equipment.

07/2006 – 01/2008 AAF International Louisville, Kentucky
Mechanical Designer

Designed mechanical equipment, and systems to meet customer's needs using AutoCAD 2007 and Autodesk Inventor software taking into account cost, availability of materials, strength, maintenance requirements, appearance and impact on the user, and the environment.
Revised and upgraded existing CAD and hand drawings to meet ASME Y14.5 Standard and for use with Autodesk Inventor.
Performed field inspection for the fabrication and installation of air filtration equipment that included field measurements, and installation planning.
Provided 3-D rendering of equipment to the marking team for use in sales promotional material.

05/2005 – 07/2006 The Estopinal Group Jeffersonville, Indiana
Mechanical Designer

Designed the first variable refrigerant flow (VRF) system in the Louisville metropolitan area "City of New Albany Scribner Place YMCA and Aquatics Center"; 82,000 square foot facility.
Designed mechanical systems for commercial building and healthcare facilities using Trane Trace 700 and AutoCAD software.
Developed CAD drafting tool using Auto lisp, and AutoCAD to decrease the production time of construction drawings (CD's).
Performed HVAC load analysis using Trane Trace 700, and selected the HVAC system from the analysis.
Performed Construction Administration task that included overseeing construction to ensure conformity to construction drawings, specifications, and local building codes.

09/2002 – 05/2003 Eminence Speaker Eminence, Kentucky

CAD Technician

Developed drafting procedure, and CAD standards to improve the product line of existing and future speakers using Pro Engineer and AutoCAD software.

Revised and upgraded the drafting and design process for use with Pro Engineer software.

09/2000 – 09/2002 Jordan Technology/ Hicks Equipment Inc Louisville, Kentucky

Mechanical Designer

Designed vapory recovery equipment that included pressure vessels, piping and structural steel assemblies.

Developed drafting standards using ASME Y14.5

Developed equipment design standards using AutoCAD, Autodesk Inventor, Mechanical Desktop and CadWorx Pipe 2002.

Supervise construction to ensure conformity to construction drawings, specifications, and ASME code section 8 and 31.3 standards.

02/2000 – 09/2000 Griffin and Company Louisville, Kentucky

Drafter

Worked with Mechanical Designer, and Engineer's on the design of custom conveyor and automation equipment for various manufacturing capabilities Utilized AutoCAD 2000.